
Louisiana Transportation Research Center

Final Report 535

Monitoring Bridge Scour Using Fiber Optic Sensors

by

C.S.Cai, Ph.D., P.E.
Xuan Kong, Ph.D.
Wen Xiong, Ph.D.
Shuang Hou, Ph.D.

LSU



4101 Gourrier Avenue | Baton Rouge, Louisiana 70808
(225) 767-9131 | (225) 767-9108 fax | www.ltrc.lsu.edu

TECHNICAL REPORT STANDARD PAGE

1. Report No. FHWA/LA.10/535		2. Government Accession No.	3. Recipient's Catalog No.
4. Title and Subtitle Monitoring Bridge Scour Using Fiber Optic Sensors		5. Report Date April 2015	
		6. Performing Organization Code	
7. Author(s) C.S. Cai, Ph.D., P.E., Xuan Kong, Ph.D., Wen Xiong, Ph.D., Shuang, Hou, Ph.D.		8. Performing Organization Report No.	
9. Performing Organization Name and Address Department of Civil and Environmental Engineering Louisiana State University Baton Rouge, LA 70803		10. Work Unit No.	
		11. Contract or Grant No. LTRC Project Number: 08-2ST State Project Number: 736-99-1573	
12. Sponsoring Agency Name and Address Louisiana Department of Transportation and Development P.O. Box 94245 Baton Rouge, LA 70804-9245		13. Type of Report and Period Covered Final Report July 2009-June 2014	
		14. Sponsoring Agency Code	
15. Supplementary Notes Conducted in Cooperation with the U.S. Department of Transportation, Federal Highway Administration			
16. Abstract The scouring process excavates and carries away materials from the bed and banks of streams, and from around the piers and abutments of bridges. Scour undermines bridges and may cause bridge failures due to structural instability. In the last 30 years, more than 1,000 bridges collapsed in the US and about 60% of the failures are related to the scour of bridge foundations. Due to the difficulty in inspecting bridge scour, scour-induced failures tend to occur suddenly without prior warning or signs of distress to the structures. Owing to the threat of hurricane-induced flooding and the fact that there are a significant number of coastal and river/bayou bridges in Louisiana, a more reliable inspection and monitoring procedure for bridge scour is needed. This proposed study is to develop bridge scour monitoring techniques using fiber optic sensors. Based on theoretical and numerical studies, a few mechanisms were proposed for foundation scour monitoring and verified in laboratory tests. In order to apply those mechanisms to field bridges, three instrumentations were designed and tested, and one design was selected for field applications. According to the selected design, two 18-ft long piles with Fiber Bragg Grating (FBG) sensors were then fabricated, transported, and installed besides the foundation of the field bridge. Finally, the long-term monitoring was conducted to evaluate the foundation scour condition.			
17. Key Words scour, pile, bridge, monitoring, optic sensor, instrumentation, data, acquisition		18. Distribution Statement Unrestricted. This document is available through the National Technical Information Service, Springfield, VA 21161.	
19. Security Classif. (of this report) N/A	20. Security Classif. (of this page) N/A	21. No. of Pages 160	22. Price N/A

Project Review Committee

Each research project will have an advisory committee appointed by the LTRC Director. The Project Review Committee is responsible for assisting the LTRC Administrator or Manager in the development of acceptable research problem statements, requests for proposals, review of research proposals, oversight of approved research projects, and implementation of findings.

LTRC appreciates the dedication of the following Project Review Committee Members in guiding this research study to fruition.

LTRC Manager

Walid Alaywan, Ph.D., PE
Structures Research Manager

Members

Ray Mumphrey, P.E
Stephanie Cavalier, P.E
Steve Lee, P.E
Steve Menuier, P.E
Michael Boudreaux, P.E
Art Aguirre, P.E

Directorate Implementation Sponsor

Janice Williams, P.E.
DOTD Chief Engineer

Monitoring Bridge Scour Using Fiber Optic Sensors

by

C.S.Cai, Ph.D., P.E.

Xuan Kong, Ph.D.

Wen Xiong, Ph.D.

Shuang Hou, Ph.D.

Department of Civil Engineering
Louisiana State University
Baton Rouge, Louisiana 70803

LTRC Project No. 08-2ST
State Project No. 736-99-1573

conducted for

Louisiana Department of Transportation and Development
Louisiana Transportation Research Center

The contents of this report reflect the views of the author/principal investigator who is responsible for the facts and the accuracy of the data presented herein. The contents do not necessarily reflect the views or policies of the Louisiana Department of Transportation and Development, Federal Highway Administration or the Louisiana Transportation Research Center. This report does not constitute a standard, specification, or regulation.

April 2015

ABSTRACT

The scouring process excavates and carries away materials from the bed and banks of streams, and from around the piers and abutments of bridges. Scour undermines bridges and may cause bridge failures due to structural instability. In the last 30 years more than 1,000 bridges collapsed in the US and about 60% of the failures are related to the scour of bridge's foundations. Due to the difficulty in inspecting bridge scour, scour-induced failures tend to occur suddenly without prior warning or signs of distress to the structures. Owing to the threat of hurricane-induced flooding and the fact that there are a significant number of coastal and river/bayou bridges in Louisiana, a more reliable inspection and monitoring procedure for bridge scour is needed.

The present study is to develop bridge scour monitoring techniques using fiber optic sensors. Based on theoretical and numerical studies, a few mechanisms were proposed for foundation scour monitoring and verified in laboratory tests. In order to apply those mechanisms to field bridges, three instrumentations were designed and tested, and one design was selected for field applications. According to the selected design, two 18-ft long piles with FBG sensors were then fabricated, transported, and installed besides the foundation of the field bridge. Finally, the long-term monitoring was conducted to evaluate the foundation scour condition.

ACKNOWLEDGMENTS

The investigators are grateful to the Federal Highway Administration and the Louisiana Transportation Research Center (LTRC), Louisiana Department of Transportation and Development (DOTD) for funding this project. The contents of this report reflect only the views of the authors who are responsible for the facts and the accuracy of the data presented herein. The authors would like to thank those who provided help during the development of the initial tasks of this research program. Special thanks go to the project manager Walid Alaywan, the crew of DOTD at District 61 for the fabrication at the workshop and installation at the bridge in the field, and graduate students at Louisiana State University (LSU) for their hard work during the fabrication and bridge testing process.

IMPLEMENTATION STATEMENT

As a type of fiber optical sensor, Fiber Bragg Grating (FBG) sensors have been gaining popularity and acceptance in structural health monitoring. However, the monitoring instrumentation designed in this project is only validated in the laboratory and is the first application on field bridges. Although many tests have been conducted in the laboratory, a successful application depends on many factors. The most important ones are:

- (1) Understanding the principal and performance of FBG sensors;
- (2) Carefully fabricate the monitoring pile and attach the sensors; and
- (3) Regularly check the water level and take measurements from the sensors to monitor the scour condition to ensure the long-term structural performance.

The success of this research project will help Louisiana develop an effective technique to monitor the bridge foundation scour, give the bridge department an early warning to inspect and retrofit bridges, and ultimately prevent possible bridge failures due to bridge scour. However, currently, measurements are carried out by field trips and it is very difficult to know in advance if a high water and scour event occurs. For practical applications, on-line monitoring technology using FBG sensors should be developed, which can continuously monitor the scour process.

TABLE OF CONTENTS

ABSTRACT.....	iii
ACKNOWLEDGMENTS	v
IMPLEMENTATION STATEMENT	vii
TABLE OF CONTENTS.....	ix
LIST OF TABLES	xi
LIST OF FIGURES	xiii
INTRODUCTION	1
Literature Review	
Bridge Scour Definition.....	2
Bridge Scour Prediction.....	4
Bridge Scour Modeling.....	9
Field Scour Measurement and Monitoring Instrumentation.....	12
Scour Countermeasures	17
A Few DOTs’ Practice.....	21
OBJECTIVE	25
SCOPE	27
METHODOLOGY	29
Theoretical and Numerical Studies on Scour Effect.....	29
Analytical Study on Static Solution.....	29
Analytical Study on Dynamic Solution	31
Numerical Examples and Parametric Analyses	33
Proposed Methods for Scour Detection and Monitoring	37
Laboratory Test on Scour Mechanisms	39
Test Design	40
Test Configuration	40
Test Loads.....	43
FRP Bar Response.....	47
Scour Monitoring Instrumentation Design for Field Application.....	47
Fiber Bragg Grating Sensor	48
Monitoring System and Instrumentation Design	51
Experimental Setup.....	58
Field Installation and Test.....	61
Bridge Description	61
Data Acquisition Systems - FBG Interrogator.....	63
Instrument Fabrication and Sensor Preparation.....	64

In-situ Installation	65
DISCUSSION OF RESULTS	68
Laboratory Test Results	68
Specimen Test	68
Test of FRP Bar on Steel Tube (stand)	75
Test of FRP bar on GFRP pipe	89
Results of Instrumental Design	95
Experimental Results for Case 1	95
Experimental Results for Case 2	96
Experimental Results for Case 3	97
Field Monitoring Results	98
Data Collection	98
Field Results of Pile I	100
Field Results of Pile II	105
CONCLUSIONS.....	107
RECOMMENDATIONS	109
REFERENCES	111
ACRONYMS, ABBREVIATIONS, & SYMBOLS.....	119
APPENDIX A.....	121
Installation Procedure for Fiber Optic FBG.....	121
Fundamentals of FOS (Fiber Optic Sensing).....	121
Monitoring with FBG Optic Fibers.....	122
Monitoring with OTDR Based Optic Fibers.....	124
APPENDIX B	129
Field Long-Term Monitoring Guidelines	129
System Concepts.....	129
Monitoring Procedure	130

LIST OF TABLES

Table 1	Comparison of existing instruments for measuring bridge scour	17
Table 2	Comparison between armoring and flow-altering scour countermeasures.....	18
Table 3	Dynamic and kinematic viscosity of water in SI units	45
Table 4	Rebar frequencies	46
Table 5	Incipient motion formulas.....	47
Table 6	Comparison results	58
Table 7	Soil condition.....	62
Table 8	Test detailed information	68
Table 9	Typical correct network settings.....	136
Table 10	Sample data format	140

LIST OF FIGURES

Figure 1 Illustration of bridge scour	3
Figure 2 Illustration of flow during bridge scour.....	3
Figure 3 Comparison of scour equations with field measurement	7
Figure 4 Configuration of a typical feed forward neural network	8
Figure 5 Local scour depth measuring instruments	12
Figure 6 Transmission and deflection of signal in detecting scour using radar.....	13
Figure 7 Working principle of sonar.....	14
Figure 8 Experimental setup for TDR system	15
Figure 9 FBG scour monitoring system.....	16
Figure 10 Scour Protection by riprap.....	19
Figure 11 Scour Protection by using collar.....	20
Figure 12 Scour countermeasure using a downstream bed-sill	21
Figure 13 Schematic of pile under scour	29
Figure 14 Pile deflections at varied scour ratios.....	33
Figure 15 Pile moments at varied scour ratios.....	33
Figure 16 Pile displacements at different positions	34
Figure 17 Pile moments at different positions	34
Figure 18 Pile head deflections with different beta	35
Figure 19 Pile head deflections with different k.....	35
Figure 20 1st frequency changing with scour ratio.....	36
Figure 21 4th frequency changing with scour ratio	36
Figure 22 First frequency with various k.....	36
Figure 23 Change ratio of 1st frequency.....	38
Figure 24 Change ratio of 1st frequency with scour ratio=5% (4 ft).....	38
Figure 25 Bending moment profile.....	39
Figure 26 First modal strain profile	39
Figure 27 Concept of scour monitoring using FBG sensors.....	40
Figure 28 Design of FRP bar on steel tube	41
Figure 29 Schematic drawing of test design	42
Figure 30 Test specimen and layout on shaking table	42
Figure 31 Monitoring mechanisms to be tested.....	43
Figure 32 Pseudo static loading	43
Figure 33 Noise loading.....	44
Figure 34 Drag coefficient for a smooth circular cylinder in steady flow	45
Figure 35 Turbulent flow around an obstacle.....	45

Figure 36	Work principle of FBG sensors	48
Figure 37	Detailed sketch of Design 1	52
Figure 38	Monitoring principle of Design 1	53
Figure 39	Detailed sketch of Design 2 segment	54
Figure 40	Monitoring principle of Design 2	55
Figure 41	Schematic description for the response of each FBG sensor	56
Figure 42	Detailed sketch of Design 3.....	57
Figure 43	Design of sensor protection system.....	57
Figure 44	Monitoring principle of Design 3	58
Figure 45	Instrumentation assembling.....	59
Figure 46	Installation of FBG sensors and their protection system.....	60
Figure 47	Water flume and experimental setup.....	61
Figure 48	Bridge layout	62
Figure 49	Pattern of ground line change.....	63
Figure 50	Si425 optical sensing interrogator	63
Figure 51	Fabrication and sensor testing	64
Figure 52	In-situ installation of the middle pile.....	65
Figure 53	In-situ installation of the side pile	66
Figure 54	The original status of instrument.....	67
Figure 55	Sensor layout after installation	67
Figure 56	Clicking test of FRP specimen	69
Figure 57	Strain response of gentle clicking.....	69
Figure 58	Strain response of moderate clicking	69
Figure 59	Strain response of heavy clicking.....	69
Figure 60	Strain response of test 1 at 11.5s~12.5s	70
Figure 61	FFT of strain response of test 1 at 11.5s~12.5s.....	70
Figure 62	Strain response of test 1 at 21.3s~21.7s	70
Figure 63	FFT of strain response of test 1 at 21.3s~21.7s.....	70
Figure 64	Strain response of test 2 at 9.2s~9.8s	70
Figure 65	FFT of strain response of test 2 at 9.2s~9.8s.....	70
Figure 66	Strain response of test 3 at 10.8s~11.8s	71
Figure 67	FFT of strain response of test 3 at 10.8s~11.8s.....	71
Figure 68	Clicking test of FRP specimen	71
Figure 69	Comparison of the strain response clicked by the hammer.....	72
Figure 70	Water flow test of FRP specimen.....	73
Figure 71	Strain response of water flow test	73
Figure 72	Strain response during 71s~74s.....	73

Figure 73	FFT of strain response during 71s~74s	73
Figure 74	Strain response during 170s~174s.....	74
Figure 75	FFT of strain response during 170s~174s	74
Figure 76	Strain response during 222s~226s.....	74
Figure 77	FFT of strain response during 222s~226s	74
Figure 78	Strain response during 518s~522s.....	74
Figure 79	FFT of strain response during 518s~522s	74
Figure 80	Schematic drawing of test	75
Figure 81	Strain response of test 1.....	75
Figure 82	Strain response of test 2.....	76
Figure 83	Strain response of test 3.....	76
Figure 84	Bending on the top.....	76
Figure 85	Strain response of bending test.....	76
Figure 86	Bending on the top of steel tube	77
Figure 87	Strain response of test 1.....	77
Figure 88	Strain response of test 2.....	77
Figure 89	Strain response of test 3.....	77
Figure 90	FRP bar clicked at 2.95 ft position	78
Figure 91	Zoomed strain response under clicking, 1st run.....	78
Figure 92	Strain response under clicking, 2nd run	79
Figure 93	Strain response under clicking, 3rd run	79
Figure 94	Layout of the specimen	80
Figure 95	Loading procedure of 0.82 ft/s and 1.64 ft/s	80
Figure 96	Strain response, water 0.66 ft., 0.82 ft/s	81
Figure 97	Zoomed strain response, water 0.66 ft., 0.82 ft/s	81
Figure 98	Strain response, water 0.66 ft., 1.64 ft/s	82
Figure 99	Zoomed strain response, water 0.66 ft., 1.64 ft/s	82
Figure 100	Strain response, water 1.31 ft., 0.82 ft/s	83
Figure 101	Zoomed strain response, water 1.31 ft., 0.82 ft/s	84
Figure 102	Strain response, water 1.31 ft., 1.64 ft/s	84
Figure 103	Zoomed strain response, water 1.31 ft., 1.64 ft/s	85
Figure 104	Strain response, water 1.97 ft., 0.82 ft/s	85
Figure 105	Zoomed strain response, water 1.97 ft., 0.82 ft/s	86
Figure 106	Strain response, water 1.97 ft., 1.64 ft/s	86
Figure 107	Zoomed strain response, water 1.97 ft., 1.64 ft/s	87
Figure 108	Strain response, water 2.62 ft., 0.82 ft/s	87
Figure 109	Zoomed strain response, water 2.62 ft., 0.82 ft/s	88

Figure 110	Strain response, water 2.62 ft., 1.64 ft/s	88
Figure 111	Zoomed strain response, water 2.62 ft., 1.64 ft/s	89
Figure 112	FFT of strain response	90
Figure 113	Strain response of the pipe without sand	91
Figure 114	Strain distribution of first run	91
Figure 115	Normalized strain distribution of first run	92
Figure 116	Normalized strain distribution of 6 runs	92
Figure 117	Normalized strain distribution of pipe with 0.66 ft. sand	92
Figure 118	Normalized strain distribution of pipe with 1.31 ft. sand	92
Figure 119	Strain of FRP bar with 1.31 ft. sand	93
Figure 120	Strain of GFRP pipe with 1.31 ft. sand	93
Figure 121	Strain of FRP bar with 0.66 ft. sand	94
Figure 122	Strain of GFRP pipe with 0.66 ft. sand	94
Figure 123	Strain distribution with 1.31 ft. sand, $v=0.82$ ft/s	95
Figure 124	Experimental results of case 1	96
Figure 125	Experimental results of case 2	97
Figure 126	Experimental results of case 3	98
Figure 127	Field data collection	99
Figure 128	Water conditions of different dates	100
Figure 129	Original signal of Sensor I-1	101
Figure 130	Strain response of Sensor I-1	102
Figure 131	Pile-I data on 2013-05-28	103
Figure 132	Pile-I data on 2013-09-21	104
Figure 133	Pile-I data on 2014-02-22	105
Figure 134	Data of Sensor II-1	106
Figure 135	Basic structure of optical fiber	121
Figure 136	Principle of FBG	122
Figure 137	FBG sensors for strain measurement in rebar	123
Figure 138	Principle of OTDR based optic fiber	124
Figure 139	OTDR based optic fiber crack sensor	125
Figure 140	The fiber cleaver unit - Fujikura CT-30	126
Figure 141	Fiber splicing unit - Fujikura FSM-50S splicer	127
Figure 142	Front and rear panel view of si425	131
Figure 143	SM040-016 (16-ch. coupler extension)	132
Figure 144	Sensor wavelength view screenshot	132
Figure 145	Table view screenshot	133
Figure 146	Channel power view screenshot	133

Figure 147	FFT view screenshot.....	134
Figure 148	Sensor FFT view with basic menu options.....	134
Figure 149	Sensor wavelength view with system menu options	135
Figure 150	System IP address query screen shot.....	136
Figure 151	Local area connection property window	137
Figure 152	Screen shot when remote client identified.....	138
Figure 153	Typical host PC software interface.....	138
Figure 154	Screen shot of channel power level view in LABVIEW utility	139
Figure 155	Save data mode screen shot.....	140

INTRODUCTION

The interstate highway network is an important national asset. Bridges constituting critical nodes within transportation networks are the backbones of the transportation infrastructure. It is well-known that scour is one of the major causes of bridge failures. In the last 30 years, more than 1,000 bridges collapsed in the US and about 60% of the failures are related to the scour of bridge's foundations [1], [2]. The collapse of the I-90 Bridge over Schoharie Creek in April 5, 1987, in New York renewed national attention to scour-induced problems. Without warning, five vehicles plunged into the creek and 10 people were killed as two spans of the bridge fell into the floodwaters. Therefore, bridge scour has been identified as the most common cause of highway bridge failures in the United States [3]. The extent of this potential problem is magnified by the fact that according to a study by the Transportation Research Board in 1997, there were 488,750 bridges over streams and rivers in the U.S., and the annual cost for scour-related bridge failures was estimated at \$30 million [4]. Owing to the threat of hurricane-induced flooding and the fact that there are a significant number of coastal and river/bayou bridges in Louisiana, a more reliable inspection and monitoring procedure for bridge scour is needed.

In cooperation with Department of Transportations (DOTs) and the Transportation Research Board, the Federal Highway Administration (FHWA) has developed some scour monitoring and inspection instruments. However, there is a need to develop more reliable, economical instrumentation and equipment to measure bridge scour for the purpose of research and to indicate when a bridge is in danger of scour failure. Therefore, additional research is necessary. Some pilot studies using fiber optic sensors to monitor bridge scour have been carried out in the last decade. The authors propose here to deploy this technology in Louisiana.

Fiber Optic Sensors (FOSs) have become increasingly popular in long-term monitoring of structures, especially in harsh environments. The FOSs' major unique benefits related to this project are: corrosion-resistant and long-term stability that make it possible to be embedded in soil/foundations and submerged in water; distributed sensing and multiplexing capabilities that make it possible to install a series of sensors along a single cable to collect information along the depth of the foundation; small size and light weight with little disturbance to the structure and soil; immunity to electromagnetic/radio frequency interference, etc. The FOS system, particularly fiber Bragg Grating (FBG) sensors, will thus be explored for this application by using it to measure strain, pressure, or other related information so that the scour situation of bridges can be either directly monitored or derived.

As discussed earlier, fiber optic sensors will be embedded in the foundation during the construction process or installed after the construction. As scour occurs and the soil is washed away, some sensors originally embedded in the soil will be exposed to the water. The emerging sensors will pick up the strain due to the bending of the rod or plate where the optic fiber is installed and direct water pressure can also be measured from the sensors directly exposed to the water. From the information of a series of fiber optic sensors, the water level, scour depth, and the water flow information can be monitored. During flood events, the cavity caused by scour may be refilled by debris or mud, which may give false information that scour had never happened if a traditional underwater inspection is conducted. The proposed procedure will monitor the scour and/or refill process, which will ensure the safety of the bridge. Since the fiber optic sensors measure the absolute values of wavelength shift, only one initial reading is needed and the monitoring can be either continuous or intermittent. For regular strain gages, for example, the harsh environment will make them useless in a short period of time and initial reading is needed for each measurement, which make the intermittent measurement much more difficult.

This project will help Louisiana develop the required expertise for the field applications of fiber optic sensors. The success of this research project will reap great economic benefits and may largely impact the practice of bridge maintenance in Louisiana. There is also potential for this project to develop and test equipment that can be used for future scour monitoring. The ultimate objective will be to develop more efficient strategies to mitigate the deficiencies of bridges.

Literature Review

Bridge Scour Definition

Scour is the result of the erosive action of flowing water, which excavates and carries away materials from the bed and banks of streams, and from around the piers and abutments of bridges (Figure 1). Bridge scour is a dynamic phenomenon that varies with many factors such as water depth, flow angle and strength, pier and abutment shape and width, material properties of the sediment, and so on. There are generally three types of scour that affect the performance and safety of bridges: local scour, contraction scour, and degradational scour [5]. Local scour is the removal of sediment from around bridge piers or abutments. Water flowing past a pier or abutment may scoop out holes in the sediment, which are known as scour holes (see Figure 1). Contraction scour is the removal of sediment from the bottom and sides of the river. It is caused by an increase in the speed of the water as the water moves through a bridge opening that is narrower than the natural river channel. Degradational scour is the general removal of sediment from the river bottom by the flow of the river. This

sediment removal and resulted lowering of the river bottom are a natural process, but may remove large amounts of sediment over time.

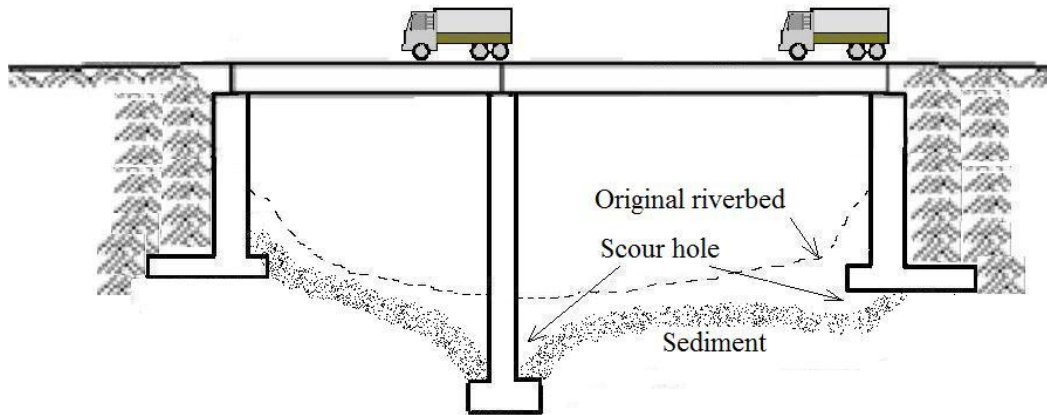


Figure 1
Illustration of bridge scour

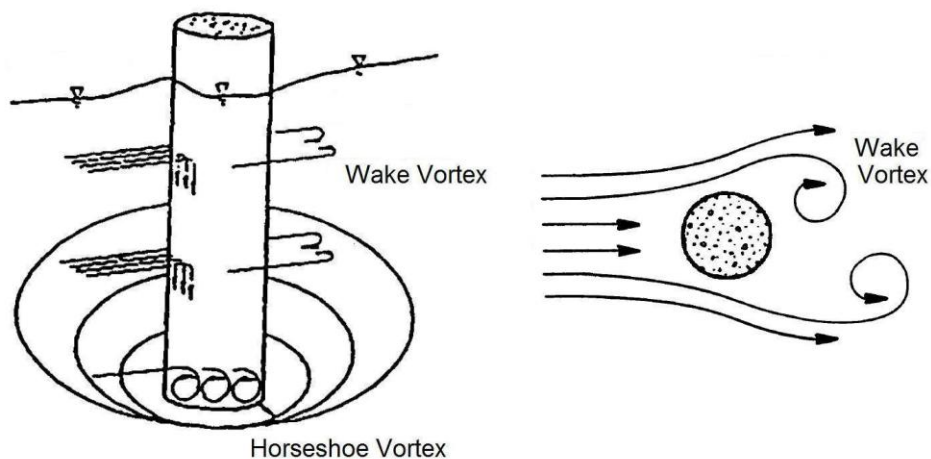


Figure 2
Illustration of flow during bridge scour

Figure 2, adapted from Richardson and Davis, shows the schematic of the flow development in the vicinity of a circular pier situated in a scour hole [6]. As can be seen from Figure 2, wake vortices are formed as the flow, which is separated by the pier, converges at the downstream of the pier. Also, as the mean flow approaches the pier at the middle, a portion of the approach flow is forced to move down the front surface of the pier. When this portion of flow reaches the channel bed, a horseshoe vortex is formed at the base of the pier, which causes local scour at the pier. The mechanism of scour development can be described as the following: The action of horseshoe vortices removes bed materials from around the base of

the obstruction [6]. If the transport rate of sediment away from the base region is greater than the transport rate into the region, a scour hole develops. The strength of horseshoe vortices will be reduced as the depth of scour increases, thereby reducing the transport rate from the base region. Eventually, for live-bed local scour, equilibrium is reestablished between bed material inflow and outflow and the scouring process ceases. For clear-water scour, the scouring process ceases when the shear stress caused by horseshoe vortices is equal to the critical shear stress of the sediment particles at the bottom of the scour hole.

Although scour may occur at any time, scour action is especially strong during floods. Scour undermines bridges and causes bridge failures as a result of structural instability. Scour failure tends to occur suddenly without prior warning to structures. Factors affecting bridge scour include channel and bridge geometry, floodplain characteristics, flow hydraulics, bed materials, channel protection measures, channel stability, riprap placement, ice formations, debris, etc. This paper presents a comprehensive review of the up-to-date work on scour at bridge piers and abutments, including scour prediction, modeling, monitoring, and countermeasures.

Bridge Scour Prediction

Over the past few decades, bridge engineers and researchers have found that bridge scour is related to many factors such as the geometry of the channel, dynamic hydraulic properties of the flow, geometry of the bridge piers and abutments, etc. Predicting bridge scour using the available information of these factors prior to or during flood events is very important in preventing catastrophic failures of bridges and possible loss of life. Scour prediction practice can be generally divided into two categories: (1) predict bridge scour using empirical equations; and (2) predict bridge scour using other methods, such as Neural Networks. It should be noted that both the final scour depth and real time scour depth can be predicted.

Predicting Bridge Scour Using Empirical Equations. Numerous studies have been conducted with the purpose of predicting scour, and various equations have been developed [7-18]. Most of these empirical equations were based on laboratory results and field data, and they differ from each other with respect to the factors considered in constructing the scour model, parameters used in the equation, laboratory or site conditions, etc. Among these equations, one of the most commonly used pier scour equation in the United States is the Colorado State University equation recommended in the U.S. Department of Transportation's Hydraulic Engineering Circular No. 18 (HEC-18) [19], which is expressed as follows:

$$d_s = 2.0yK_1K_2K_3(b/y)^{0.65}F^{0.43} \quad (1)$$

where, d_s = scour depth; y = flow depth at the upstream of the pier; K_1 , K_2 , and K_3 = correction factors for the pier nose shape, angle of attack flow, and bed condition, respectively; b = pier width; and F = Froude number. It is recommended in the HEC-18 that the limiting value of d_s / y is 2.4 for $F \leq 0.8$ and 3.0 for $F > 0.8$. Equation (1) was developed from laboratory data and was recommended for both live-bed and clear-water conditions. A few other commonly used equations are also listed in the following. For the purpose of simplification, repeated terms in the following equations will not be explained again.

Equation presented by Neil [20], which was developed from the design curves by [7]:

$$d_s = 1.35b^{0.7}y^{0.3} \quad (2)$$

Shen equation [9]:

$$d_s = 0.00022\left(\frac{Vb}{v}\right)^{0.3} \quad (3)$$

where, V = average velocity of approach flow; and $v = 1 \times 10^{-6} m^2 / s$.

Jain and Fischer equation [11]:

$$\begin{cases} d_s = 2.0b(F - F_c)^{0.25}\left(\frac{y}{b}\right)^{0.5} & (F - F_c) > 0.2 \\ d_s = 1.85b(F_c)^{0.25}\left(\frac{y}{b}\right)^{0.5} & 0 < (F - F_c) \end{cases} \quad (4)$$

where, F_c = critical Froude number. For $0 < (F - F_c) < 0.2$, the larger of the two scour depths computed using the two equations is used.

Froehlich equation [13]:

$$d_s = 0.32b\phi F^{0.2}\left(\frac{b_e}{b}\right)^{0.62}\left(\frac{y}{b}\right)^{0.46}\left(\frac{b}{D_{50}}\right)^{0.082} \quad (5)$$

where ϕ = coefficient based on the shape of the pier nose; b_e = width of the bridge pier projected normal to the approach flow; and D_{50} = median grain size of bed material.

Melville and Sutherland equation [12]:

$$d_s = K_l K_a K_y K_a K_s b \quad (6)$$

where, K_f = flow intensity factor; K_d = sediment size factor; K_y = flow depth factor; K_a = pier alignment factor; and K_s = pier shape factor.

Though all these proposed equations have been demonstrated to be applicable and accurate for a certain set of data, there has been considerable uncertainty when selecting these equations to predict scour in field practice. To test the accuracy of the developed bridge-scour equations, comparative studies have been conducted by many researchers. J. S. Jones compared the available bridge scour equations using laboratory data and limited field data [21]. In his study, he classified all equations into three categories: those of the University of Iowa, those of the Colorado State University, and those based on foreign literature. He found that the Colorado State University equation enveloped the data, but that the scour depths were less than other equations. P. A. Johnson compared seven of the most commonly used and cited scour equations and models using a large set of field data from both live-bed and clear-water scour [22]. The differences between these equations and their limitations were explained in his study. M. N. Landers and D. S. Mueller evaluated selected pier scour equations using 139 measurements of local scour in live-bed and clear-water conditions [23]. Comparisons of computed and observed scour depths in their study indicate that none of the selected equations accurately estimate the depth of scour for all of the measured conditions.

D. S. Mueller compared 22 scour equations using a large amount of field data collected by the USGS [24], [25]. In his study, he concluded that the HEC-18 equation was good for design because it rarely underpredicted the measured scour depth. However, it frequently overpredicted the observed scour. Figure 3 (adopted from D. S. Mueller) shows the data containing 384 field measurements of scour at 56 bridges from his study [24].

Though conclusions from comparative studies by different researchers more or less differ from each other, it is generally believed, based on the conducted laboratory experiments and field tests, that most existing equations may overestimate the scour depth and are generally conservative [26-30].

Most work on scour prediction discussed previously is focused on the equilibrium scour depth. Time development of scouring has also attracted the attention of many researchers [31-37].

A. M. Yanmaz and H. D. Altinbilek studied the time-dependent local scour around bridge piers under clear water conditions with single cylindrical and square piers [32]. In their study, the time variation of the scour depth around bridge piers can be determined by solving a differential equation. They concluded that the shape of the scour hole around bridge piers

remains almost unchanged with respect to time. However, the rate of scour development decelerates with time.

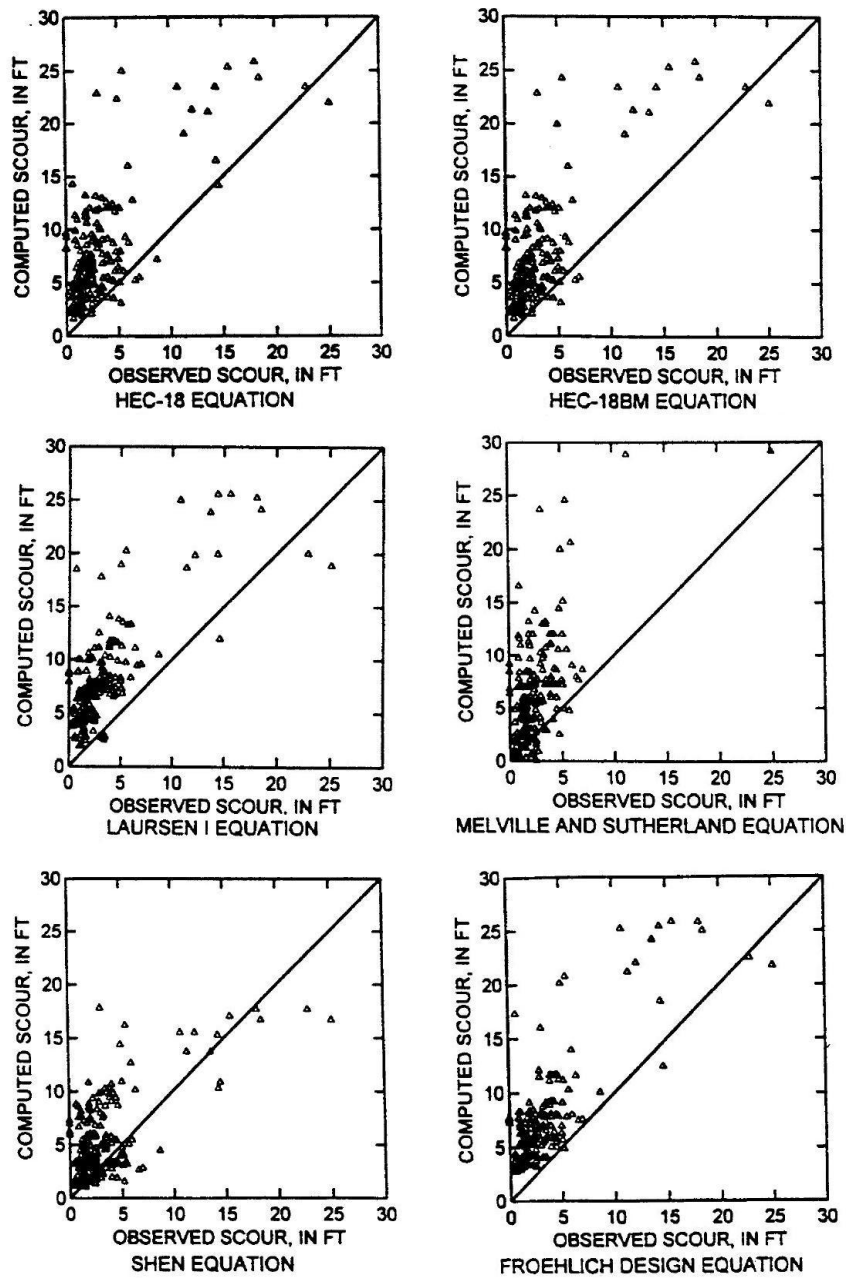


Figure 3
Comparison of scour equations with field measurement

B. W. Melville and Y. M. Chiew studied the temporal development of clear-water local scour depth at cylindrical bridge piers in uniform sand beds [35]. The temporal development of the scour depth as a function of t was described using the equation below:

$$\frac{d_s}{d_{se}} = \exp \left\{ -0.03 \left| \frac{V_c}{V} \ln \left(\frac{t}{t_e} \right) \right|^{1.6} \right\} \quad (7)$$

where, d_{se} = equilibrium scour depth; V_c = critical mean approach flow velocity for entrainment of bed sediment; and t_e = time for equilibrium depth of scour to develop.

Predicting Bridge Scour Using Neural Networks

The mechanism of flow around a pier structure is so complicated that it is difficult to establish a general empirical model to provide accurate estimation for scour, as has been demonstrated in the previous section where comparative studies of different equations were reviewed. Besides the complexity of the scour process, there are also two other reasons why existing methods do not always produce reasonable results for scour predictions. First, site conditions are usually much more complicated than laboratory conditions. Second, the traditional analytical tools of statistical regression have limitations regarding selecting the parameters used in the formulas and determining the exact types of relationships between the responses and the parameters.

Recently, Artificial Neural Networks (ANNs) have been successfully used in predicting bridge scour [38-41]. A significant advantage of using ANNs in predicting the bridge scour is that there is no need to have well-defined physical relationships between the bridge scour (the output) and various factors that affect bridge scour (the inputs). Because the ANNs have more freedom in defining the relationships between the bridge scour and the factors, they have the potential to predict more accurate scour information than the traditional regression based methods [41].

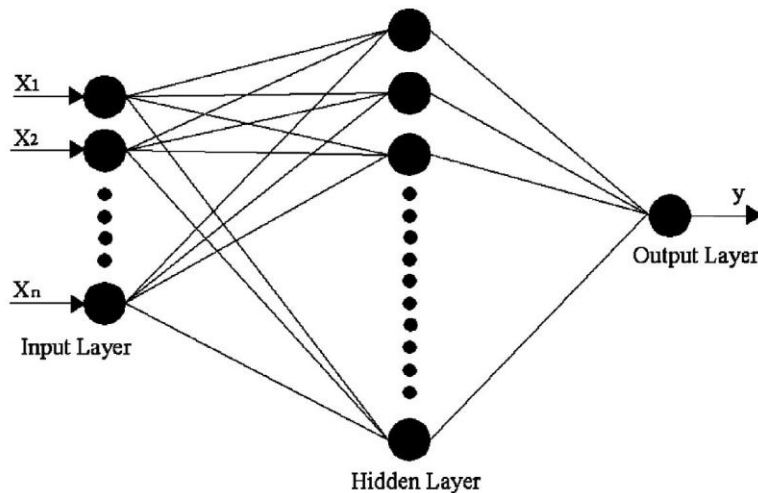


Figure 4
Configuration of a typical feed forward neural network

Figure 4 shows the configuration of a typical three-layer neural network, which consists of an input layer, a hidden layer, and an output layer. The basic idea of the neural network can be described as the following: Firstly, a set of data ($X_1, X_2 \dots X_n$) as raw information are fed into the network at the input layer; then, the neural network will be trained and the complex relationships between inputs and output (y) will be determined during the training process using specified mathematical functions and weights on the connections between the units in the hidden layer and the units in the input layer as well as the output layer; finally, the output can be determined from the weights on the connections between the units in the hidden layer and the output.

Bateni et al. used ANNs and an adaptive neuro-fuzzy inference system (ANFIS) to estimate both the equilibrium and time-dependent scour depth with a large amount of laboratory data [39]. In their study, two ANN models, a multi-layer perception using back-propagation algorithm (MLP/BP) and radial basis using orthogonal least-squares algorithm (RBF/OLS), were used. The equilibrium scour depth was modeled as a function of five variables: flow depth, mean velocity, critical flow velocity, mean grain diameter, and pier diameter. The time variation of scour depth was also modeled in terms of the equilibrium scour depth, equilibrium scour time, scour time, mean flow velocity, and critical flow velocity. Numerical test results in their study indicated that the MLP/BP model provides a better prediction of scour depth than the RBF/OLS and ANFIS models as well as the previous empirical approaches. Lee et al. used the Back-Propagation Neural Network to predict the scour depth around bridge piers and their study showed that scour depth can be efficiently predicted using the BPN [40]. Mohammad et al. also used two ANN models, the feed forward back propagation (FFBP) model and the radial basis function (RBF) model, to predict the depth of the scour hole around a pile group [41]. Their numerical test results indicated that the ANN predictions are generally more satisfactory than those obtained using empirical methods because of their low errors and high correlation coefficients. Through a sensitivity analysis they also found that the pile diameter and the ratio of pile spacing to pile diameter are the two most significant parameters that affect the scour depth.

Bridge Scour Modeling

As discussed earlier, bridge scour is a very complicated process which involves the interaction between the flow around a bridge pier or abutment and the erodible bed surrounding it. To study the complicated bridge scour process, different numerical models as well as laboratory models have been developed in the past few decades.

Numerical Models. In order to verify the accuracy of the developed numerical models, most numerical models were developed along with laboratory models and their results were compared with each other. Fukuoka et al. developed a three-dimensional numerical simulation model for the local scour around a bridge pier [42]. Their study showed that the developed numerical model can obtain, with adequate accuracy, solutions that are in good agreement with the experimental results of the local scour from the large-scale hydraulic model. J. E. Richardson and V. G. Panchang used a fully three-dimensional (3-D) hydrodynamic model to simulate the flow occurring at the base of a cylindrical bridge pier within a scour hole [43]. The results of the numerical simulation were also compared with laboratory observations by B. W. Melville and A. Raudkivi [44]. Strong agreements were achieved between the studies, both quantitatively and qualitatively. They concluded that the discrepancies between the results of the two studies may be attributed to the parameters chosen in the numerical model.

Numerical results for bridge scour were also compared to empirical equations. Young et al. developed a numerical model for clear-water abutment scour depth along with an independent three-dimensional finite element model [45]. In their study, the predicted scour depths were in agreement with the predicted results from the finite element model. They also concluded, from a comparative study, that the HEC-18 prediction overestimates measurement by 22 percent [19]. Kassem et al. at the University of South Carolina, developed a computational fluid dynamics mode, FLURNT, to simulate the field data [46]. Their numerical model was verified against measurements obtained in the laboratory and satisfactory agreements were obtained between the numerical results and measurements. Using the developed model, they demonstrated that the HEC-18 significantly overestimates the scour depth in their case study [19].

Laboratory Models. The advantage of laboratory studies of bridge scour is that they can not only help better understand the effect of different variables and parameters associated with scour and therefore improve the scour prediction equations, but can also help develop alternative or improved scour countermeasures. In the past two decades, a significant amount of research effort has been spent on laboratory investigation of bridge scours. Different laboratory models for bridge scour have been established and tests have been conducted for different purposes.

To study the deep scour hole downstream of a large circular pier at the Imbaba Bridge, one of the major bridges across the Nile River, an undistorted mobile bed model, with a scale 1:60, was constructed at the Hydraulics and Sediment Research Institute (HSRI), Cairo [15]. A series of clear water scour tests were performed to investigate the causes of the local scour

downstream the circular pier. It was found that the large scour hole downstream of the circular pier was produced by the conflicting velocity fields at the intersection of the wake vortex streams from adjacent piers, and increased by the confluence flow. Based upon the results of this investigation, an empirical formula was developed to predict the wake and confluence maximum local scour depth downstream of a circular pier for a clear water condition.

Umbrell et al. investigated clear-water bridge contraction scour caused by pressure flow beneath a bridge without the localized effect of piers or abutments [47]. A tilting flume that measured 70 ft. (21.3 m) long, 5.9 ft. (1.8 m) (0.60 m) wide, and 1.96 ft. (0.60 m) deep was used in their study. A model bridge deck was tested under a variety of laboratory-controlled pressure-flow conditions. Different factors such as approach velocity, pressure-flow velocity under the bridge deck, and sediment size were studied.

D. M. Sheppard and M. William Jr. studied the local clear-water and live-bed scour using laboratory tests for a range of water depths and flow velocities with two different uniform cohesionless sediment diameters (0.01 in. (0.0003 m) and 0.033 in. (0.00084m)) and a circular pile with a diameter of 0.49 ft. (0.15 m) [48]. The tests were performed in a tilting flume 4.9 ft. (1.5 m) wide, 3.9 ft. (1.2 m) deep, and 148 ft. (45 m) long) located in the Hydraulics Laboratory at the University of Auckland in Auckland, New Zealand. Figure 5 shows the measuring instruments for local scour depth used in their study [48]. As shown in Figure 5, the scour depth as a function of time is measured with acoustic transponders and video cameras. Bed forms and bed elevation at the flume walls during the live-bed tests can be monitored with video cameras. Flow velocity, water depth, and temperature can also be measured during the tests. In their experiments, large bed forms were observed migrating through the scour hole during a number of the live-bed scour tests and they concluded that Sheppard's equations appeared to perform well for the range of conditions covered by the experiments [49].

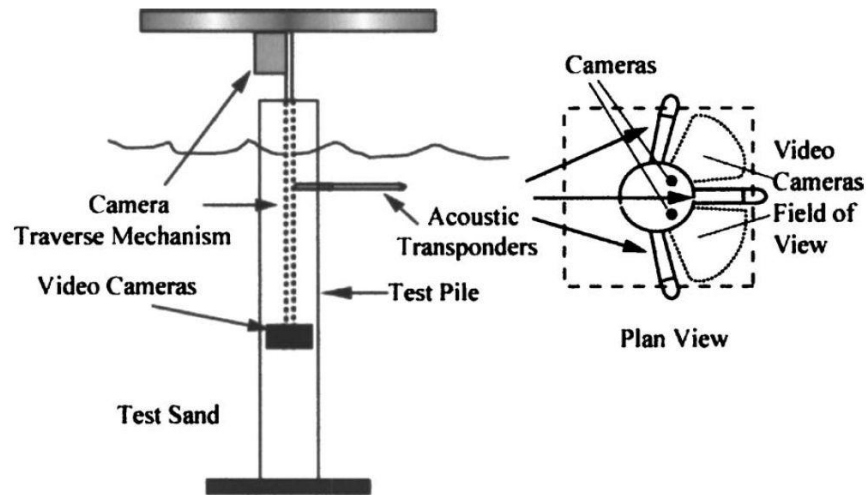


Figure 5
Local scour depth measuring instruments

Field Scour Measurement and Monitoring Instrumentation

Though laboratory studies provide a good way to verify bridge scour theories and a better understanding of the complicated scour process, laboratory results may vary with respect to different laboratory conditions. Also, many times, results from laboratory studies cannot be directly used to guide design practice because of the simplifications and assumptions made in laboratory study which may make the results not applicable to field applications. Therefore, field data are still very important and desirable since they provide critical information of the bridge condition with which engineers can directly use to make important decisions. Field data are also very important with regard to evaluating and verifying existing laboratory scour models and empirical equations.

Over the past half century, the U.S. Geological Survey (USGS) along with the FHWA and state DOTs in the United States have put a significant amount effort into the study of bridge scour in field. In 1987, the FHWA funded the USGS to initiate the National Bridge Scour Program. In 1996, after many years of effort, the USGS published a national bridge scour report, which aimed to guide the practice of engineers [23]. In addition to research effort and the reports released by the USGS, many journal articles and conference proceedings have also been published in the past several decades.

Over the past few decades, measurement and monitoring instrumentation has also been developed for bridge scour. In the early days, radar and sonar were employed successfully to identify the scour depth [50-57].

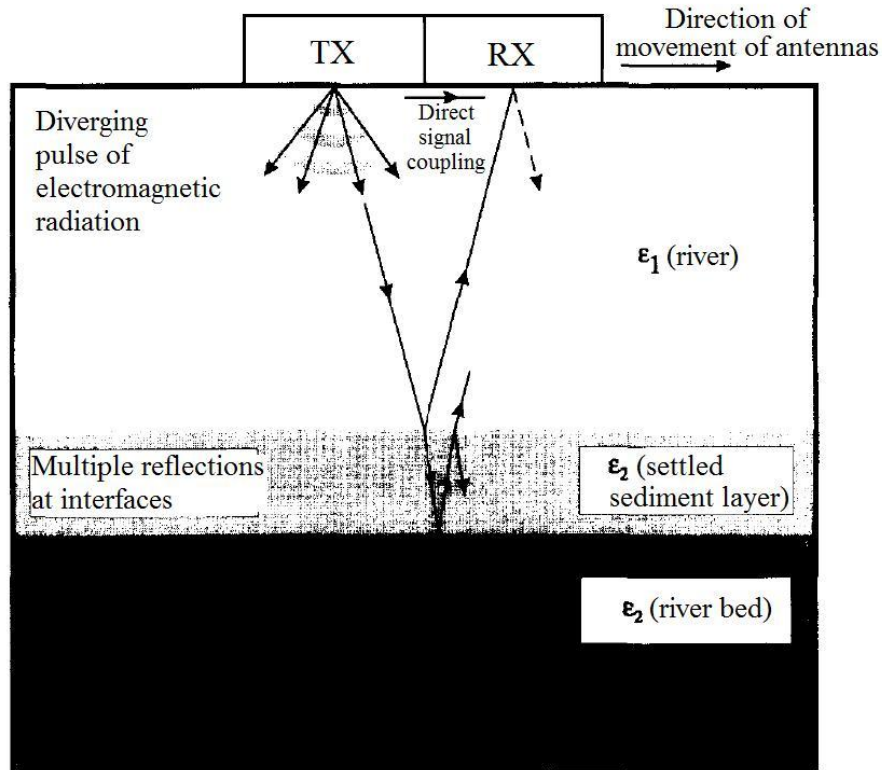


Figure 6
Transmission and deflection of signal in detecting scour using radar

Radar is a system that uses electromagnetic waves to identify the range, altitude, direction, or speed of both moving and fixed objects such as aircraft, ships, motor vehicles, weather formations, and terrain. Figure 6 illustrates how radar can be used to detect bridge scour [52]. In Figure 6, electromagnetic waves are sent out through the transmitting antenna (TX). The majority of the signal sent out will be propagating downward until an interface is reached where the underlying material has different electrical properties to the current layer in which the signal is propagating. At this interface (the interface between the river and sediment layer in Figure 6), part of the radar signal will be reflected back towards the upper surface and may be detected by the receiving antenna (RX). The other part of the signal is, however, refracted at the interface and propagates through the underlying material (the sediment) until it reaches another interface (between the sediment layer and river bed) and will be reflected again. The received radar signal at the receiving antenna will then be used to detect the surface conditions of the interfaces. During the detection process, both the transmitting antenna and receiving antenna move at a constant rate across the surface of interest.

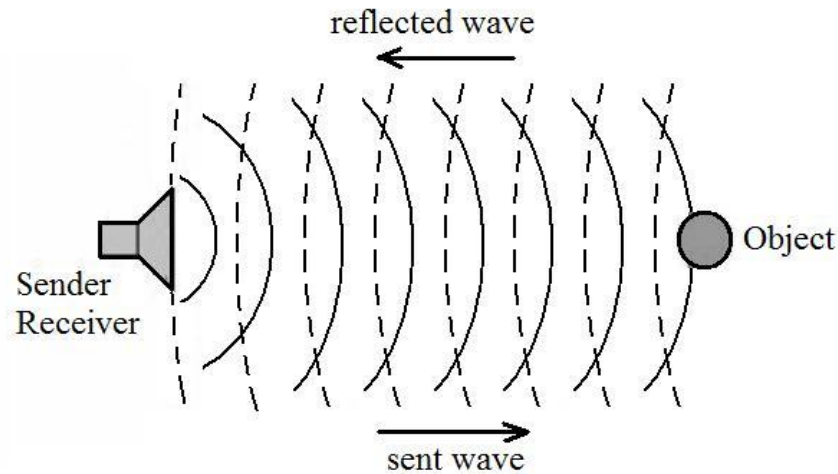


Figure 7
Working principle of sonar

Sonar, originally an acronym for sound navigation and ranging, is a technique that uses sound propagation (usually underwater) to navigate, communicate with, or detect other vessels. The working principle of using sonar to detect scour is similar to that of using radar (Figure 7). To measure the distance to an object, a pulse of sound is sent out and will be reflected back when it reaches an object. The time from transmission of a pulse to reception is measured and can then be converted into a range by knowing the speed of sound. Sonar has been developed and used to characterize the sea bottom information, for example, mud, sand, and gravel, by converting echo parameters into sediment type. Different algorithms exist in different sonar types, but they are all based on changes in the energy or shape of the reflected sounder pings. Sonar can also be used to derive maps of the topography of an area by moving the sonar across it just above the bottom. These properties make the sonar an excellent tool to detect bridge scour.

Though both radar and sonar were successfully used to detect the profile of the bridge scour, they have limited applications in monitoring scour development and are usually only used to determine the final status of the sedimentation surrounding a pier. It is difficult to employ these techniques to continuously monitor the scour process during flood events. Therefore, techniques for continuous monitoring scour process are desirable because real-time scour information can provide warning prior to bridge failures and help bridge engineers make important decisions during floods.

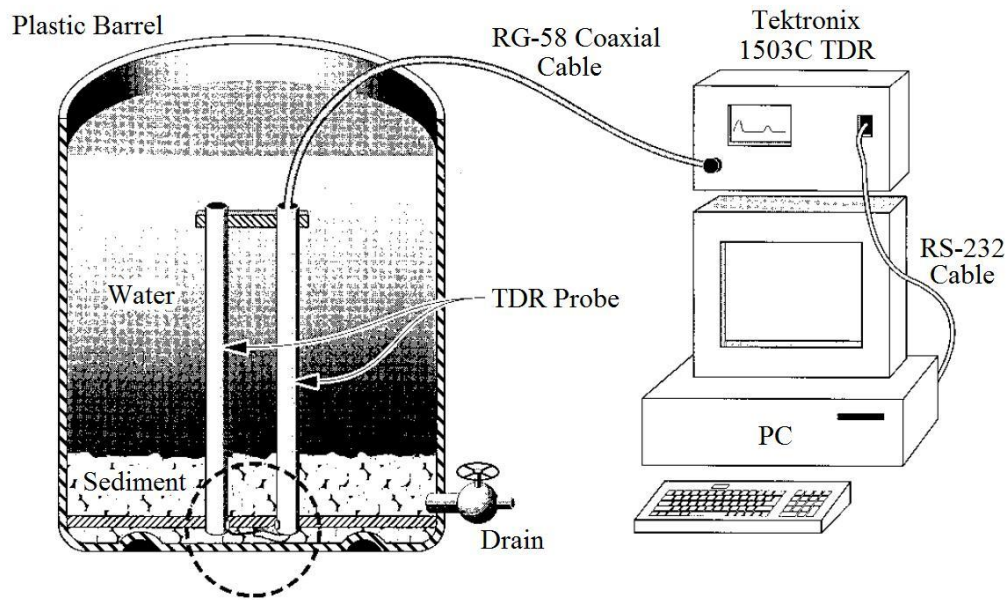


Figure 8
Experimental setup for TDR system

In recent years, techniques using Time-Domain Reflectometry (TDR) and fiber Bragg grating (FBG) sensors have been developed and used for real-time monitoring of bridge scour [1], [58-61]. Figure 8 shows the experimental setup for the TDR system used for scour monitoring [58]. The TDR operates by sending an electromagnetic pulse through the transmission line with a fixed velocity. The pulse propagates down the transmission line until the end of the line or some intermediate discontinuity (air/water interface and water/sediment interface) is reached, where part of the pulse is reflected back to the source. By measuring the returning time of the sent pulse, the physical distance between the line end or the discontinuity and the TDR source can be calculated.

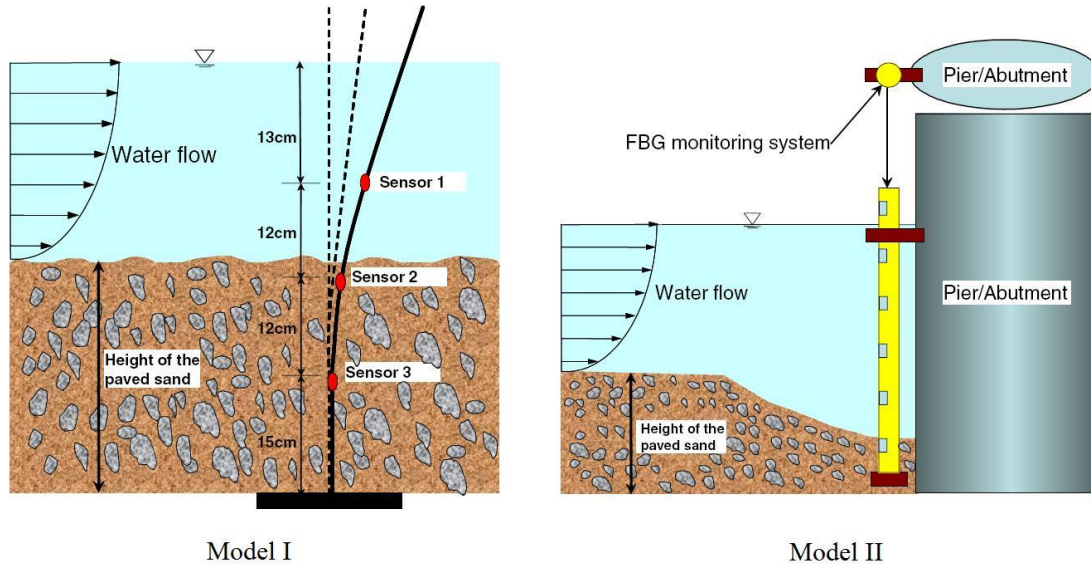


Figure 9
FBG scour monitoring system

Fiber optic sensors have many advantages over traditional sensors such as their long-term stability and reliability, resistance to environmental corrosion, and multiplexity along one single fiber [62]. Lin et al. developed two types of local scour monitoring systems to monitor real-time scour (Figure 9) [61]. In Model I, three FBG sensors are mounted on the surface of a cantilevered beam and arranged in series along one single fiber. In Model II, several FBG sensors are arranged along one single optical fiber, but are mounted on cantilevered plates installed at different levels of a hollow chamber of a steel pile fixed to the pier or abutment. In both models, when the running water flows towards the cantilevered beam or plates, deformations will be generated on the beam or plates by bending moment and strains will be detected by the FBG sensors. However, only the FBG sensors that are exposed to the water flow will pick up the strain information; for those buried under the river bed surface, no or very small strains will be generated because that part of the cantilevered beam or plates has not bent. The scour depth can then be detected by knowing the exposure conditions of the FBG sensors. It should be noted that the resolution of these two scour monitoring systems depends on and can be adjusted by the number of FBG sensors used in the systems.

Lu et al. also used a sliding magnetic collar (SMC) and a steel rod to monitor the total bridge scour during floods [30]. The lower tip of the steel rod, with a diameter of 3.94 in. (100 mm), was initially placed slightly below the riverbed in the main channel. When scour occurs, the steel rod will drop as the surface of the riverbed drops. The scour depth is determined based on the total lowering distance of the steel rod with respect to its initial position. One of the major disadvantages of this instrumentation is that it cannot detect the refilling process of the

scour. They also compared the advantages, disadvantages or limitations, and relative costs of existing instruments for measuring bridge scours, which are summarized in Table 1 [30].

Table 1
Comparison of existing instruments for measuring bridge scour

Instrument	Advantages	Disadvantages or limitations	Relative cost
Bridge mounted sonar	Continuous and accurate record of riverbed	Mild slope river/estuary	Medium
Acoustic Doppler current profilers (ADCP)	Portable; measuring both velocity profile and water depth	Not applicable to high sediment concentration conditions	High
Ground penetrating radar (GPR)	Continuous record of riverbed	Time consuming in operation; specialized training required	High
Fiber Bragg grating (FBG) sensor	Continuous monitoring of riverbed	Limited successful field tests, tests for extreme environment needed	High
Numbered bricks	Commercially available; applicable to highly turbulent or rapid flows	Excavation of riverbed required; suitable for ephemeral rivers	Low
Sliding magnetic collar (SMC)	Easy to operate	Excavation of riverbed required; high maintenance/repairing cost	Low
Steel rod	Easy to operate	Excavation of riverbed required; high maintenance/repairing cost	Low

Scour Countermeasures

Scour mitigation at bridge sites has received much attention in the past. There are many techniques, measures, and practices available for countering scour at existing bridge piers and abutments. Scour countermeasures can be generally categorized into two groups: armoring countermeasures and flow altering countermeasures. The basic idea of armoring countermeasures is the addition of another layer which can act as a resistant layer to the hydraulic shear stress and therefore provides protection to the more erodible materials underneath. Armoring countermeasures do not necessarily alter the hydraulics of approach flows. In contrast, flow altering countermeasures, as their name indicates, aim at changing the hydraulic properties of flows by using spur dikes, guidebanks, parallel walls, collars, etc., and therefore reducing the scour effect at bridge piers and abutments. A comprehensive review of different scour countermeasures for bridge piers and abutments can be found in Lagasse et al. and Barkdoll et al., respectively [63], [64]. A comparison between the working principle, advantages, and problems of the two different types of scour countermeasures is summarized in Table 2.

Table 2
Comparison between armoring and flow-altering scour countermeasures

	Armoring countermeasures	Flow-altering countermeasures
Principle	Protect the bed materials underneath the armoring layer from being scoured away.	Alter the flow alignment or break up vortices and therefore reduce the scour effect.
Advantages	Most commonly used type; easy to use; works well in most situations.	Different designs can be selected for different site conditions to achieve satisfactory results.
Problems	Winnowing of sands through the armor; difficult to keep the armor in place; constrict the channel and cause additional contraction scour.	Special design may be needed for particular site conditions; significant cost and construction of new structures may be needed.

The most commonly used armoring countermeasure is riprap [65]. Other types of armor include tetrapods, cable-tied blocks, grout filled bags, mattresses, concrete aprons, etc. An extensive review of experiments, model studies, and laboratory tests conducted on the use of riprap as a scour countermeasure around bridge piers was provided by Parker et al. [5]. Figure 10 shows the typical pier riprap configurations in Lagasse et al., with (a), (b), (c) representing placing the riprap layer at the surface of the channel bed, in a pre-existing scour hole or in a hole excavated around the pier, and at the depth below the average bed level, respectively [63]. Placing the riprap layer at depth below the average bed level was recommended in their study. C. S. Lauchlan and B. W. Melville experimentally studied the effects of failure mechanisms, stability, and placement level for riprap at bridge piers [65]. Their study also showed that deeper placement level of the riprap layer provides better protection against local scour.

Different flow altering countermeasures have also been proposed, using submerged vanes, sacrificial sill, collars and slots, parallel wall, etc. [66-70]. Figure 11 shows the use of a collar in preventing scour by Zarrati et al. [69].

As can be seen from Figure 11, the collar (with a round shape) divides the approach flow into two regions above and below the collar. The collar acts as an obstacle against the down flow and therefore reduces its strength. The strength of the down flow at the region below the collar is also reduced, so is the strength of the horseshoe vortex. The efficiency of a collar depends on its size and relative location on the pier with respect to the bed.

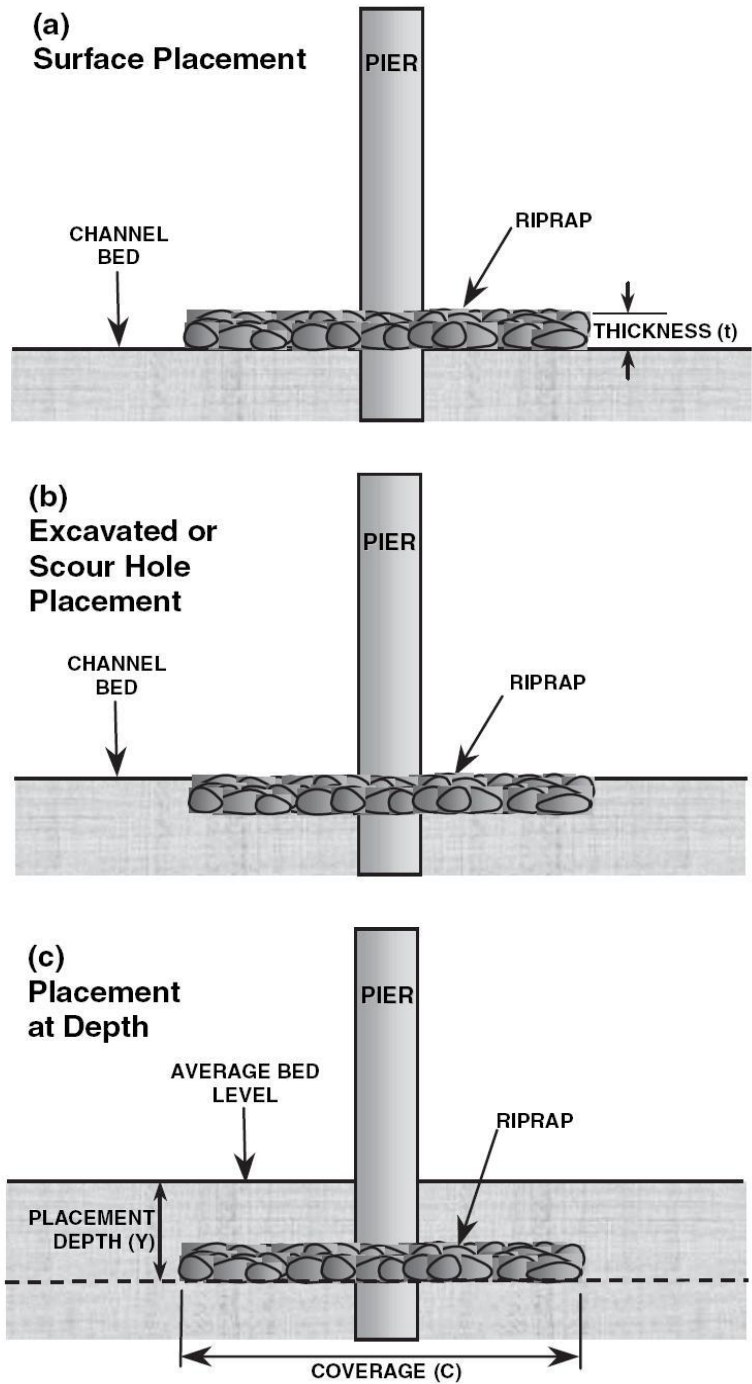


Figure 10
Scour Protection by riprap

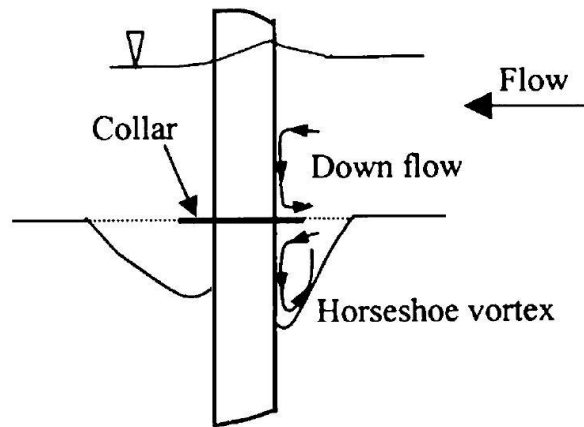


Figure 11
Scour Protection by using collar

Most countermeasures mitigate scour effect by using devices on the upstream side of bridge piers or by changing the geometry of bridge piers facing the approach flow. Grimaldi et al. presented a scour control method at bridge piers by a downstream bed sill (Figure 12) [71]. The reason of setting the bed-sill downstream instead of upstream is to avoid the risk of decreasing the bed elevation due to the general and local scouring downstream of the bed sill. As can be seen in Figure 12, the final bed with the use of the downstream bed-sill is better protected than the case without bed-sill.

The selection of various countermeasures is dependent on the application and the nature of the problem: a local scour at the pier or abutment, contraction scour across the bed at the bridge opening, reach-wide channel degradation, or lateral channel movement or widening [72]. The relative effectiveness, cost, maintenance, and ability to detect failures are also important factors to be considered when selecting a scour countermeasure. Sometimes, different countermeasures need to work together to optimize the scour mitigation effect. Lagasse et al. compared different countermeasures with regard to the type of scour, hydraulic condition, maintenance, and so on, and provided the design guidelines for different countermeasures [73].

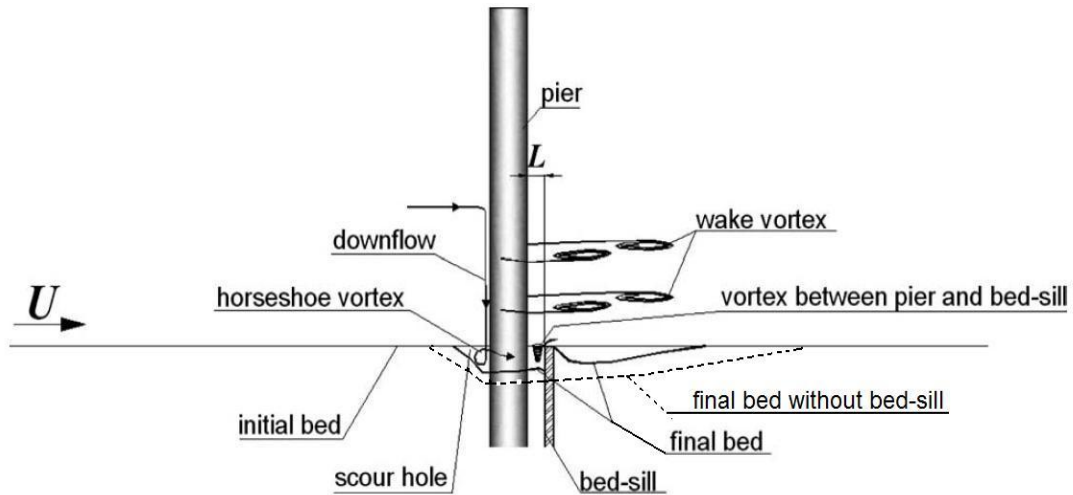


Figure 12
Scour countermeasure using a downstream bed-sill

Since the use of countermeasures often introduces uncertainty due to a lack of systematic testing and unknown potential for failures, P. A. Johnson and S. L. Niezgoda introduced a risk-based method for ranking, comparing, and choosing the most appropriate scour countermeasures using failure modes and effect analysis and risk priority numbers [72]. In their study, the uncertainty was incorporated in the failure modes and effect analysis in the selection process by considering risk in terms of the likelihood of a component failure, the consequence of failure, and the level of difficulty required to detect failures. Risk priority numbers were then used to provide justification for selecting a specific countermeasure and the appropriate compensating actions to be taken to prevent failure of the countermeasure.

In addition to the effort spent on developing appropriate scour countermeasures for existing bridge piers, a significant amount of effort has also been spent on investigating the factors that affect bridge scour, which includes type of soil in the sediment and river bed, geometry and configuration of bridge piers and abutments, foundation geometry, incline of bridge piers, and so on [74-80]. Results from these studies can also be used as references in designing bridge piers and abutments for scour and selecting appropriate scour countermeasures.

A Few DOTs' Practice

After the bridge failure occurred in New York in 1987, many researchers studied the scour phenomena. Lagasse et al. compared the performance of different fixed scour measurement devices including the sonar transducer and magnetic sliding collar [81]. The study focused on testing the instruments in enduring environmental factors and delivering usable data by

installing the magnetic sliding collar and sonar systems independently on different bridges. Schall et al. installed scour detection instruments at two tidal bridges on each coast of Florida [82]. The purpose of the study was to evaluate the transducer performance under open water marine conditions such as tidal effects, salt water, growth of marine life, corrosion, and debris. Previously, scour monitoring systems were installed on river locations. The goal of the study was to evaluate the sonic fathometer and the magnetic sliding collar system for determining the maximum depth of scour.

Following the advisory issued in 1998, the FHWA established a policy intended to assure public safety by requiring the development of formal plans of action for all scour-critical bridges. It is stated that the plan of action for each structure should include appropriate scour countermeasures or correction through scheduled hydraulic or structural construction activities and/or specific measures and instructions to prevent catastrophic failure.

Based on the information from website <http://www.gobridges.com/print.asp?id=786>, during the past four years, the Iowa Department of Transportation (Iowa DOT) has devoted a significant amount of time to evaluating the bridges under its jurisdiction and assigning scour-classification codes to them. The Iowa DOT has completed a scour evaluation for all of the approximately 2,100 bridges over waterways and classified 180 bridges as scour-critical. To predict more accurately which bridges are threatened during destructive flooding events, the Iowa DOT has been using a tool called ScourWatch.

ScourWatch is a web-based monitoring technology developed by U.S. Engineering Solutions Corporation (www.usengineeringsolutions.com) of Hartford, CT. The system identifies the occurrence of a flood event, collects stream and weather data, and matches it against the Iowa DOT's bridge data. Each bridge is given a particular flood stage threshold that is used to automatically trigger e-mail, pager, or cell phone alerts to key field personnel when scouring conditions threaten a bridge.

The Georgia Department of Transportation (GDOT), the Georgia Institute of Technology, and the U.S. Geological Survey, in cooperation with the Federal Highway Administration, are conducting an investigation to improve bridge scour predictions by combining field monitoring, physical modeling in the laboratory, and three-dimensional numerical modeling of bridge scour. Bridge scour field data are being collected at four sites located in different regions of Georgia. These field data will be used to calibrate the physical and three-dimensional numerical models.

Many other DOTs have developed and demonstrated scour monitoring techniques. Most of them use sonar transducer and magnetic sliding collar. Use of fiber optic sensors for scour monitoring is not reported in US, except for some pilot studies in Taiwan.

OBJECTIVE

The proposed research aims to develop a scour monitoring system for bridges using fiber optic sensors and verify the concept in laboratory and field tests. The system may be used for existing or newly-constructed bridges. The existing equations and methods for bridge scour predictions are based primarily on laboratory research and have not adequately been verified with field data. The developed system will be potentially used to collect field data that can be used to verify the applicability and accuracy of the various design procedures for the range of soil conditions, stream flow conditions, and bridge designs in Louisiana and eventually to result in improving existing scour prediction methods.

SCOPE

The scope of this work included theoretical and numerical studies, scour monitoring instrumentation designs and verification by laboratory tests, field installation and tests, and long-term scour monitoring. The scour monitoring system adopted the FBG fiber optic sensors and the field bridge was provided by DOTD to the research team. The scope of this research was achieved through:

Theoretical and numerical study – The scour effect on a single pile foundation was studied theoretically and verified by numerical examples. Based on that, a few scour detection mechanisms were proposed and tested in the laboratory.

Instrument design and laboratory test – Three scour monitoring systems were designed and the third one was recommended based on comparison. A sample of the recommended designed was then fabricated in the laboratory and tested in a flume at LSU.

Installation and field test – Two scour monitoring piles with FBG sensors were fabricated and driven besides the pile foundations of the selected field bridge. The original data was recorded for further comparisons.

Field long-term monitoring – Since the bridge foundation scour is a long term procedure, a long-term scour monitoring strategy was developed for this specific bridge, from which the long-term scour performance of bridges can be monitored.

METHODOLOGY

To achieve the research objective stated earlier, the research work was classified into four parts. The first part studied the scour mechanism from theoretical and numerical analyses and proposed three possible methods for monitoring foundation scour. The second part was to test the proposed monitoring methods using FBG fiber optic sensors. The third part was to design a monitoring instrument for field application and verify it with a laboratory experiment. The final part was to fabricate two test piles with FBG sensors, install them on the field bridge, and implement long-term monitoring for the field bridge.

Theoretical and Numerical Studies on Scour Effect

Bridge scour is a major cause of bridge failures and has emerged as a significant concern for bridge engineers. Most studies focused on investigating causes of the scour but not on its consequences; in other words, very few studies have been carried out on the response and feature changes of structures due to scour. Therefore, this study mainly focused on the scour effect on a single pile or pier. A theoretical solution was derived first to obtain the relationship between the scour depth and the pile response including static and dynamic responses. Since the expression of the solution is tedious and not easy to understand, two examples were used for the demonstration and parametric study. Based on the numerical observation, the present study proposed three possible methods for detecting and monitoring the bridge scour.

Analytical Study on Static Solution

Beams and columns supported along their length are very common structure configurations, and the most routine method to treat the elastic foundation is the Winkler model [83], [84]. A pile embedded in soil is similar to a beam resting on a Winkler elastic foundation. Herein, assume the pile is fully buried in soil at the beginning. After the soil is eroded, the top part of the pile is exposed to the water flow as shown in Figure 13. The pile length is L with the origin at the top of the pile, and the unsupported depth is l that is also the loading length with a distributed load $q(x)$. The unsupported length l , due to initial scour and/or initial construction, is generically called initial scour depth hereafter. The rest of the pile is embedded in the soil with an elastic spring coefficient $k(x)$. The governing equation of the pile with

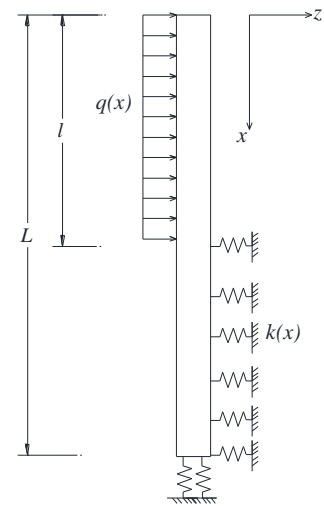


Figure 13
Schematic of pile under scour

a uniform cross-section and flexural rigidity and partially embedded in soil as shown in Figure 13 can be expressed as,

$$\begin{cases} EI \frac{d^4 w}{dx^4} = q & 0 \leq x \leq l \quad (a) \\ EI \frac{d^4 w}{dx^4} + k(x)w = 0 & l \leq x \leq L \quad (b) \end{cases} \quad (8)$$

where, $w(x)$ is the lateral displacement of the pile. Herein, $k(x)$ is considered as a constant. The general solution of equation (8) consists of two parts, namely, the deflection of the pile is divided piecewise as,

$$w(x) = \begin{cases} w_1(x) = C_1 \frac{x^3}{6} + C_2 \frac{x^2}{2} + C_3 x + C_4 + \frac{qx^4}{24EI}, & 0 \leq x \leq l \\ w_2(x) = e^{\beta x}(A_1 \sin \beta x + A_2 \cos \beta x) + e^{-\beta x}(A_3 \sin \beta x + A_4 \cos \beta x), & l \leq x \leq L \end{cases} \quad (9)$$

where, $\beta = (k/4EI)^{1/4}$, C_i and A_i ($i = 1, 2, 3, 4$) are unknown constants. The boundary condition at $x = l$ requires the geometric continuity of displacement and slope, and the continuity of bending moment and shear force, which are expressed as,

$$w_1(l) = w_2(l), \quad w_1'(l) = w_2'(l), \quad w_1''(l) = w_2''(l) \quad \text{and} \quad w_1'''(l) = w_2'''(l)$$

Four additional conditions can be derived from boundaries at $x = 0$ and $x = L$. For a free-fixed pile, there is:

$$w_1''(0) = 0, \quad w_1'''(0) = 0, \quad w_2(L) = 0 \quad \text{and} \quad w_2'(L) = 0$$

From $w_1''(0) = 0$ and $w_1'''(0) = 0$, we have $C_1 = C_2 = 0$. This leads to six condition equations to solve six constants, C_3, C_4 and A_i ($i = 1, 2, 3, 4$). The six equations can be rewritten in the matrix form as,

$$M^* \begin{bmatrix} C_3 \\ C_4 \\ A_1 \\ A_2 \\ A_3 \\ A_4 \end{bmatrix} = \begin{bmatrix} 0 \\ 0 \\ ql^4/24EI \\ ql^3/6 \\ ql^2/2 \\ ql/EI \end{bmatrix} \quad (10)$$

where, $M =$

$$\begin{bmatrix} 0 & 0 & e^{L\beta} \sin L\beta & e^{L\beta} \cos L\beta & e^{-L\beta} \sin L\beta & e^{-L\beta} \cos L\beta \\ 0 & 0 & \beta e^{L\beta} (\cos L\beta + \sin L\beta) & \beta e^{L\beta} (\cos L\beta - \sin L\beta) & \beta e^{-L\beta} (\cos L\beta - \sin L\beta) & -\beta e^{L\beta} (\cos L\beta + \sin L\beta) \\ -l & -1 & e^{L\beta} \sin \beta l & e^{L\beta} \cos \beta l & e^{-L\beta} \sin (\beta * l) & e^{-L\beta} \cos (\beta * l) \\ -1 & 0 & \beta e^{L\beta} (\cos \beta l + \sin \beta l) & \beta e^{L\beta} (\cos \beta l - \sin \beta l) & \beta e^{-L\beta} (\cos \beta l - \sin \beta l) & -\beta e^{-L\beta} (\cos \beta l + \sin \beta l) \\ 0 & 0 & 2\beta^2 e^{L\beta} \cos \beta l & -2\beta^2 e^{L\beta} \sin \beta l & -2\beta^2 e^{-L\beta} \cos \beta l & 2\beta^2 e^{-L\beta} \sin \beta l \\ 0 & 0 & 2\beta^3 e^{L\beta} (\cos \beta l - \sin \beta l) & -2\beta^3 e^{L\beta} (\cos \beta l + \sin \beta l) & 2\beta^3 e^{-L\beta} (\cos \beta l + \sin \beta l) & 2\beta^3 e^{-L\beta} (\cos \beta l - \sin \beta l) \end{bmatrix}$$

This equation can be solved very conveniently by mathematical tools, such as Mathcad or MATLAB. The six constants, expressed as the function of the scour depth and other variables, are not presented here because they are very tedious. For a pinned–pinned pile, the boundary conditions are expressed as,

$$w_1(0) = 0, \quad w_1''(0) = 0, \quad w_2(L) = 0 \quad \text{and} \quad w_2''(L) = 0$$

and equations and solutions can be similarly obtained.

Analytical Study on Dynamic Solution

As for the dynamic free vibration, the equation of motion of the same system is derived as

$$\begin{cases} EI \frac{\partial^4 w(x,t)}{\partial x^4} + \rho A \frac{\partial^2 w(x,t)}{\partial t^2} = 0, & 0 \leq x \leq l \quad (a) \\ EI \frac{\partial^4 w(x,t)}{\partial x^4} + \rho A \frac{\partial^2 w(x,t)}{\partial t^2} + k(x)w(x,t) = 0, & l \leq x \leq L \quad (b) \end{cases} \quad (11)$$

where, $w(x, t)$ is the time-dependent displacement of the pile, ρ is the mass density, and A is the cross-section area. The coefficient $k(x)$ is also considered as a constant, K . A general solution can be obtained easily by separating the variables into time and space domains using

$$w(x, t) = W(x)e^{i\omega t} \quad (12)$$

The solution of the governing equation thus reduces to that of

$$\begin{cases} \frac{d^4 W(x)}{dx^4} - \lambda^4 W(x) = 0, & 0 \leq x \leq l \quad (a) \\ \frac{d^4 W(x)}{dx^4} - (\lambda^4 - K/EI)W(x) = 0, & l \leq x \leq L \quad (b) \end{cases} \quad (13)$$

in which $\lambda = \sqrt[4]{\omega^2 \rho A / EI}$. The characteristic roots of equation (13b) are derived as

$$m_{1,2,3,4} = \pm \sqrt{\pm \sqrt{\lambda^4 - K/EI}} = \pm \sqrt{\pm \sqrt{(\omega^2 \rho A - K)/EI}}$$

Depending on the relationship between λ^4 and K/EI , different solutions can be obtained next.

If $\lambda^4 > K/EI$, the general solution is

$$W(x) = \begin{cases} W_1 = C_1 \sin \lambda x + C_2 \cos \lambda x + C_3 \sinh \lambda x + C_4 \cosh \lambda x, & 0 \leq x \leq l \\ W_2 = A_1 \sin \lambda_2 x + A_2 \cos \lambda_2 x + A_3 \sinh \lambda_2 x + A_4 \cosh \lambda_2 x, & l \leq x \leq L \end{cases} \quad (14)$$

where, $\lambda_2 = \sqrt[4]{(\omega^2 \rho A - K)/EI}$.

If $\lambda^4 < K/EI$,

$$\begin{aligned}
& W(x) = \\
& \left\{ \begin{aligned} & W_1 = C_1 \sin \lambda x + C_2 \cos \lambda x + C_3 \sinh \lambda x + C_4 \cosh \lambda x, & 0 \leq x \leq l \\ & W_2 = e^{\lambda_2 x} (A_1 \sin \lambda_2 x + A_2 \cos \lambda_2 x) + e^{-\lambda_2 x} (A_3 \sin \lambda_2 x + A_4 \cos \lambda_2 x), & l \leq x \leq L \end{aligned} \right. \quad (15)
\end{aligned}$$

where, $\lambda_2 = \sqrt[4]{(K - \omega^2 \rho A)/4EI}$.

If $\lambda^4 = K/EI$, namely, $\omega^2 = K/\rho A$,

$$\begin{aligned}
& W(x) = \\
& \left\{ \begin{aligned} & W_1 = C_1 \sin \lambda x + C_2 \cos \lambda x + C_3 \sinh \lambda x + C_4 \cosh \lambda x, & 0 \leq x \leq l \\ & W_2 = A_1 \frac{x^3}{6} + A_2 \frac{x^2}{2} + A_3 x + A_4, & l \leq x \leq L \end{aligned} \right. \quad (16)
\end{aligned}$$

Similar to the static solution, the boundary condition at $x = l$ requires the geometric continuity of displacement and slope, and the continuity of bending moment and shear force. They are expressed as:

$$W_1(l) = W_2(l), \quad W_1'(l) = W_2'(l), \quad W_1''(l) = W_2''(l) \quad \text{and} \quad W_1'''(l) = W_2'''(l)$$

Four additional conditions from the boundaries at $x = 0$ and $x = L$ depend on the particular geometry under consideration. For a free-fixed pile, we have:

$$W_1''(0) = 0, \quad W_1'''(0) = 0, \quad W_2(L) = 0 \quad \text{and} \quad W_2'(L) = 0$$

From $W_1''(0) = 0$ and $W_1'''(0) = 0$, we have $C_1 = C_3$ and $C_2 = C_4$. The rest six equations can be rewritten in the matrix form as:

$$M * [C_1 \ C_2 \ A_1 \ A_2 \ A_3 \ A_4]^T = 0 \quad (17)$$

The frequency equation is given by setting the determinant of the coefficient matrix M to be zero, i.e., $|M| = 0$. Different coefficient matrices can be derived for the three cases discussed above. Therefore, the natural frequency in different ranges should be solved by different frequency equations derived from the corresponding coefficient matrix, as described below.

If $\omega > \sqrt{K/\rho A}$, i.e. $\lambda^4 > K/EI$, the coefficient matrix is derived from equation (14) and denoted as M_1 . The natural frequencies are obtained by solving $|M_1| = 0$.

If $\omega < \sqrt{K/\rho A}$, i.e. $\lambda^4 < K/EI$, the coefficient matrix is derived from equation (15) and denoted as M_2 . The natural frequencies are obtained by solving $|M_2| = 0$.

If $\omega = \sqrt{K/\rho A}$, the natural frequencies are automatically obtained.

Numerical Examples and Parametric Analyses

On the basis of the above analytical solution, an example was used for a demonstration of the static solution. A square concrete pile with properties: $L = 40$ ft., $A = 24 \times 24$ in², $EI = 599424$ kips-ft², and $q = 10$ kips/ft. The elastic coefficient of soil per unit is $k = 5760$ kips/ft². The pile head is free and the pile bottom is assumed to be fixed. A program was developed in MATLAB to solve the analytical equations. In the case of $l = L$, the pile without soil supporting is identical to a cantilever beam with a distributed loading, which is a special case and can be used for validation. Figure 14 shows that the pile deflections of both cases (cantilever beam and $l/L = 1$) are exactly the same as they are supposed to be, which validates the numerical solution procedure of the present study.

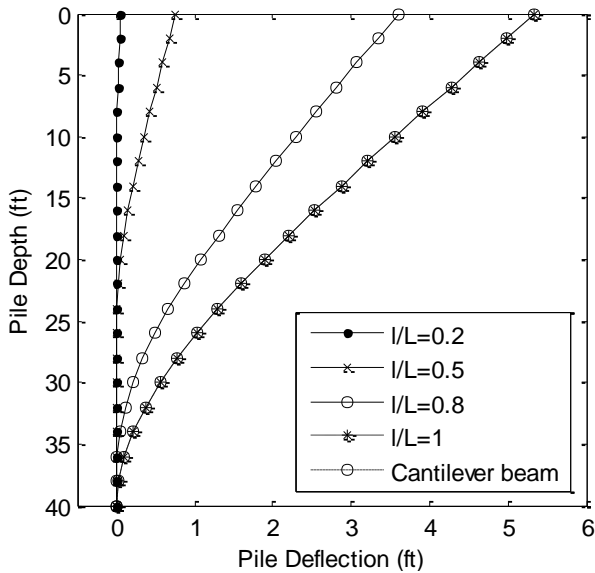


Figure 14
Pile deflections at varied scour ratios

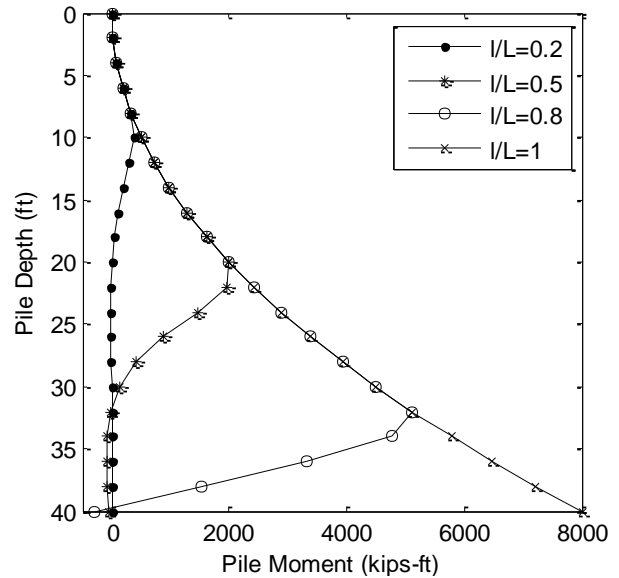


Figure 15
Pile moments at varied scour ratios

The scour ratio is defined as the ratio between the length without soil supporting and the pile length, l/L , and ranges from 0 to 1. The pile deflection and moment at various scour ratios are shown in Figure 14 and Figure 15. It can be easily seen that the pile displacement, moment, and the location of the maximum moment increase with the increase of the scour ratio. There exists a turning point in the moment curve at a location close to the interface between the water and soil. More details are described in the next section. Figure 16 shows the pile displacement at different positions versus the scour ratio and all the curves have the same

trend. Figure 17 shows the pile moment (curvature) at different positions versus the scour ratio. It is found that for any position of the pile, if it is buried deeply in the soil, its moment is not significant. Only if the scour depth approaches to that position, the moment becomes significant. Take the $x = 0.8L$ section as an example. As the scour ratio increases from 0 to about 0.6, the moment of this section is small and hardly changes because the section is buried in the soil. However, when the scour ratio is larger than 0.6, the moment increases quickly from a small negative value to a positive value. It reaches the maximum at the scour ratio of 0.8 and remains constant since the section is totally exposed to the water at and after this scour ratio. Figure 18 and Figure 19 demonstrate the influence of pile stiffness represented by $\beta = EI/k$ and soil stiffness represented by k .

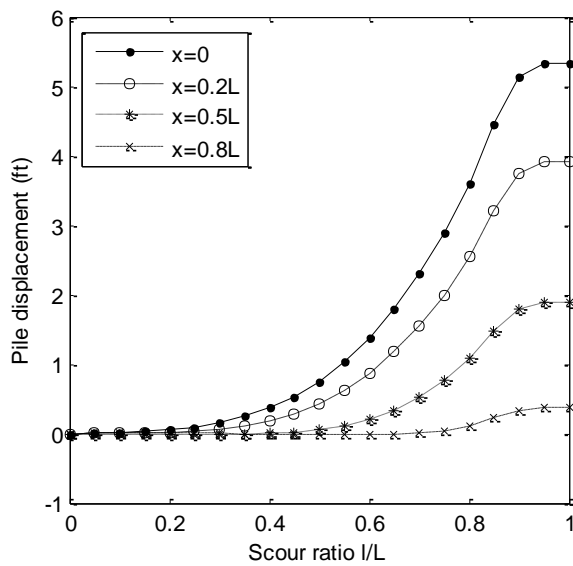


Figure 16
Pile displacements at different positions

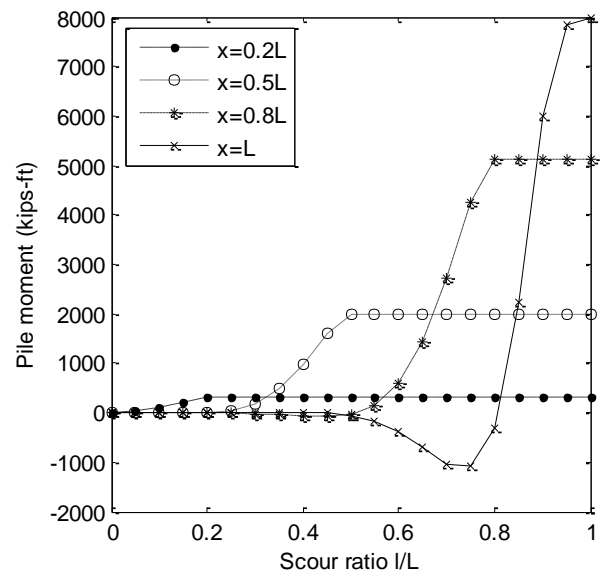


Figure 17
Pile moments at different positions

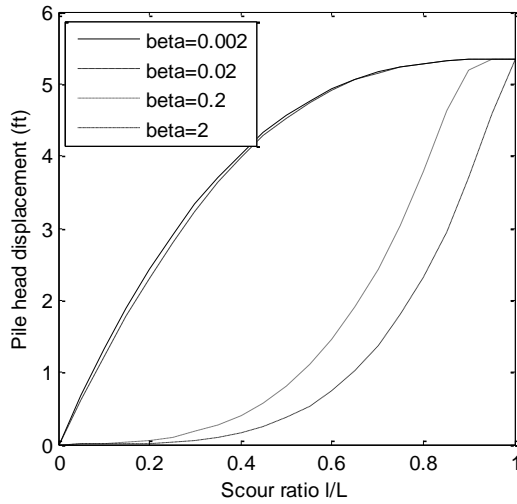


Figure 18
Pile head deflections with different beta

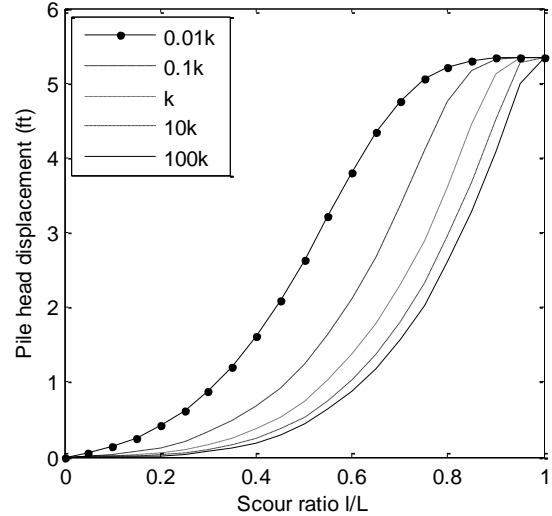


Figure 19
Pile head deflections with different k

Meanwhile, a pile similar to example 1 was adopted for a demonstration of the dynamic solution: $L = 40$ ft., $A = 24 \times 24$ in², $E = 3122$ ksi, $I = 1.333$ ft⁴, and density = 150 pcf. In order to validate the relationship between ρA and K for different cases, the coefficient of soil here is 57.6 kips/ft². The pile head is free and the pile bottom is assumed to be fixed. A program was developed in MATLAB to obtain the frequency equation from the determinant and then to solve the equations. Again, the special case of $l = L$ was used for verification. The first four natural frequencies from the present study are 0.4957 Hz, 3.1059 Hz, 8.6986 Hz and 17.038 Hz, respectively; while from the reference are 0.4957 Hz, 3.1065 Hz, 8.6992 Hz and 17.0459 Hz, respectively, which are very close to each other [85].

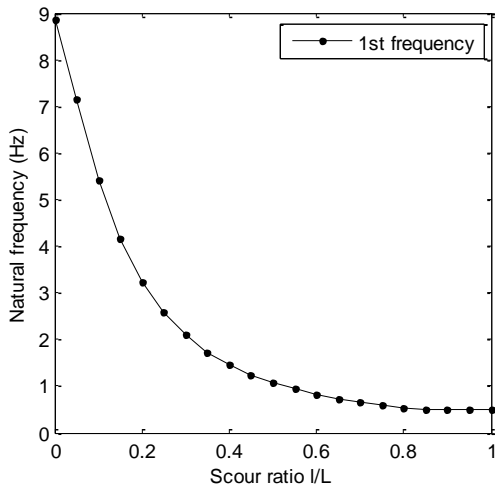


Figure 20
1st frequency changing with scour ratio

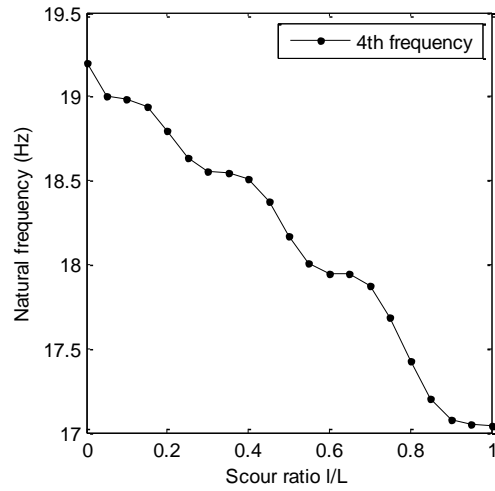


Figure 21
4th frequency changing with scour ratio

Figure 20 and Figure 21 show the first and fourth natural frequencies of the pile versus the scour ratio. The natural frequency decreases as the scour ratio increases, with the frequency of the first mode dropping much faster than that of the fourth mode. It means that the scour effect on the lower mode is more significant than on the higher mode, which will benefit the scour monitoring discussed later. Figure 22 shows the effect of the soil stiffness on the first natural frequency, and it mainly affects the natural frequency when the scour ratio is small.

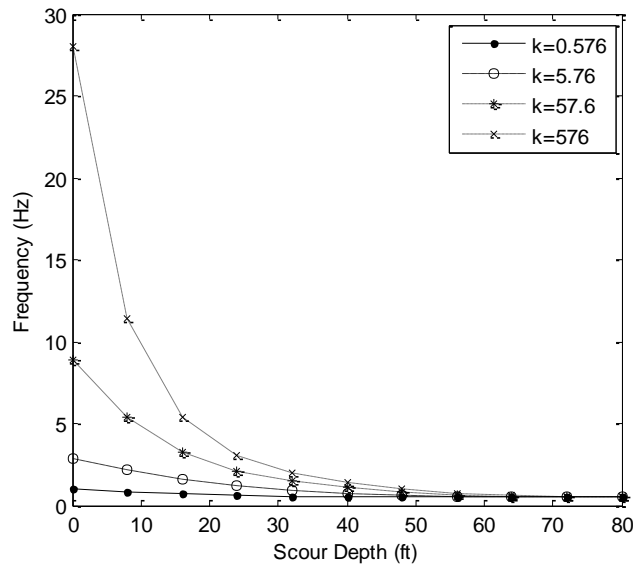


Figure 22
First frequency with various k

Proposed Methods for Scour Detection and Monitoring

Many methods have been developed for the short-term detection and long-term monitoring of bridge scour. In the early days, methods based on geophysical techniques, such as radar and sonar, were employed to identify the scour depth. However, most of them have found very limited applications due to difficulties such as the result interpretability, high noise sensitivity, and different issues during flood events [86]. In recent years, techniques using Time-Domain Reflectometry (TDR) and fiber Bragg grating (FBG) sensors are under development and used for real-time field monitoring. Due to their advantages over traditional sensors, such as their long-term stability and reliability, resistance to environmental corrosion, and multiplexity along one single fiber, fiber optic sensors become popular in structural performance monitoring [87]. The challenge of FBG applications in bridge scour is how to design the instruments and mount the sensors to obtain useful data. Lin et al. developed two types of local scour monitoring systems, using a cantilever beam or plate that is fixed to the pier [61]. Lu et al. used a sliding magnetic collar (SMC) and a steel rod to monitor bridge scour [88].

In the present study, methods based on a single pile were proposed. Instead of attaching an instrument to the bridge pier/pile, a separate pile or similar structure installed with FBG sensors was adopted and driven beside the monitored pile group. Anti-collision piers can be used for this purpose. Based on the analytical and numerical analyses of scour effects on the pile response discussed earlier, three possible methods to detect and monitor the foundation scour were proposed and discussed below. They are the methods based on (a) the pile's natural frequency change, (b) bending moment profile, and (c) modal strain profile.

Scour monitoring based on frequency change

The first step of damage detection is to determine the occurrence of damage [89]. From the results of example 2 shown in Figure 20 ~Figure 22, it is found that the reduction of soil around the pile will reduce the pile's natural frequency, especially the low order frequencies. Since the low order frequencies are easily measured, the change of frequency is an alternative feature for detecting the occurrence of scour damage. Figure 23 presents the change ratio of the first natural frequency versus the initial scour depths (the initial position of the interface between soil and water) for three different additional scour ratios, namely 5% [scour depth=4 ft. (1.22 m)], 10% [8 ft. (2.44 m)] and 15% [12 ft. (3.66 m)]. It can be seen that for this 80 ft. pile, when the initial soil position is above the 50 ft. line (measured from the pile top), an additional scour ratio of 5% [4 ft. (1.22 m)] can result in more than 10% change in the first natural frequency. It implies that if an additional scour with a ratio of more than 5% occurs on a pile with an unsupported length of less than 62.5% ($50/80 =$

0.625), it can be detected through the change of the fundamental frequency. Figure 24 displays the same observation on the piles supported with soil of different stiffness.

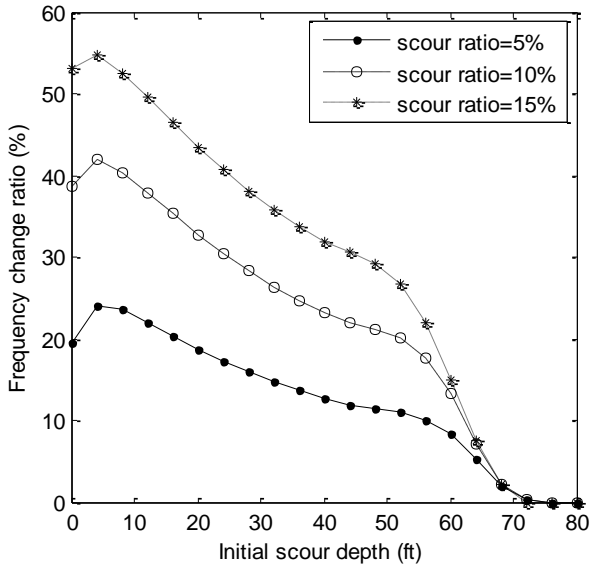


Figure 23
Change ratio of 1st frequency

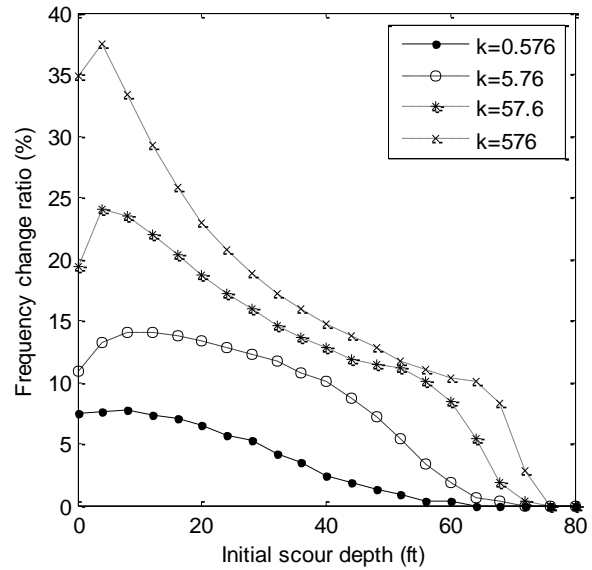


Figure 24
Change ratio of 1st frequency
with scour ratio=5% (4 ft.)

Scour monitoring based on bending moment profile

Figure 15 and Figure 17 showed that the maximum moment of the pile changes with the scour ratio and its location is slightly below but close to the scour depth. Therefore, a method based on the bending moment profile was proposed here for scour monitoring. As shown in Figure 25, the turning points of the three curves are 8.8 ft. (2.68 m), 16.8 ft. (5.12 m), and 24.8 ft. (7.56 m), compared to the total unsupported length (scour depth) of 8 ft. (2.44 m), 16 ft. (4.88 m), and 24 ft. (7.32 m), respectively. As expected, the detected turning point of moments is typically lower than the true soil (scour) line because the soil provides an elastic (not rigid) support to the pile. The turning point of the pile moment profile can still be considered as the detected scour depth since it is very close to the true scour depth. From an engineering practice point of view, the top soil is typically weak after being disturbed and does not provide much support to the pile. Therefore, the fact that the detected scour depth is slightly lower than the true soil position has a practical significance. For a single pile, it is easy to obtain the moment profile through strain sensors attached along the pile under applied testing loads or hydraulic loads.

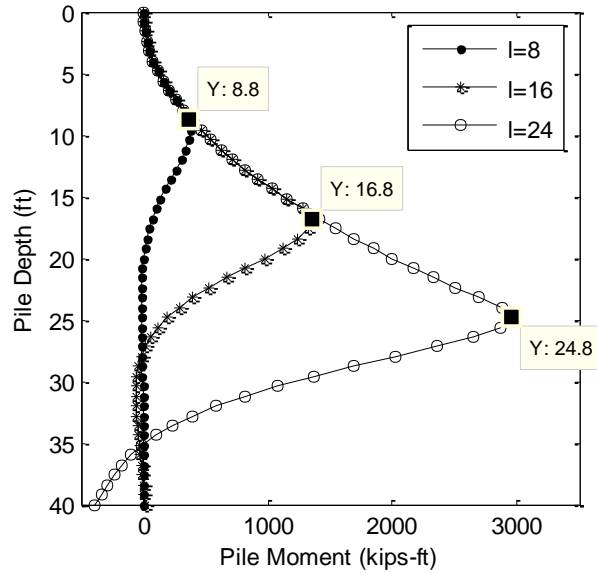


Figure 25
Bending moment profile

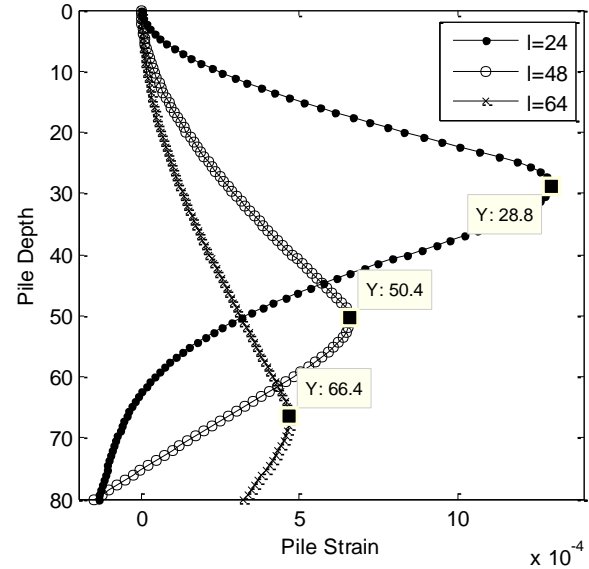


Figure 26
First modal strain profile

Scour monitoring based on modal strain profile

The modal information such as natural frequency and mode shape is easy to obtain from the time history data recorded from dynamic tests, which makes it attractive for damage and scour detection. Similar to the moment profile method, a strategy based on the modal strain (curvature) profile was also proposed in the present study. As shown in Figure 26, the modal strain extracted from the first modal shape is similar to the bending moment profile. The detected scour based on this strategy would be 28.8 ft. (8.78 m), 50.4 ft. (15.4 m), and 66.4 ft. (20.2 m), compared to the true scour depth 24 ft. (7.32 m), 48 ft. (14.64 m), and 64 ft. (19.5 m), respectively. Just as in the bending moment case, the detected turning point of strains is typically lower than the true soil (scour) line because the soil provides an elastic (not rigid) support to the pile. Since the modal information is related to the physical property of the structure, it should be more applicable and practical than the bending moment from static loading.

Laboratory Test on Scour Mechanisms

The laboratory test was designed and conducted to verify the structural behavior under static and dynamic loadings and the feasibility of the proposed scour monitoring mechanisms. Some of the conceptual tests were carried out using the water tank and shaking table available at LSU.

The present study developed a scour monitoring system using Fiber Optic Sensors (FOSs) that have wide applications in long-term monitoring of structures, especially in harsh

environments. The major benefits of choosing FOSs for scour applications are: good corrosion-resistance and long-term stability that make it possible to be embedded in soil and submerged in water; distributed sensing and multiplexing capabilities that make it possible to install a series of sensors along a single cable to collection information along the depth of the foundation; small size and light weight with little disturbance to the structure and soil; immunity to electromagnetic/radio frequency interference, etc.

Test Design

This study developed a system using relatively inexpensive instrumentation and a robust, permanent sensor arrangement. Figure 27 shows the basic concept. Fiber optic sensors can be glued onto or embedded into the fiber reinforced polymer (FRP) bar. The reason to choose a FRP bar is due to its durability and corrosion resistance features. The optic fiber can measure the strain along the optic fiber. When the sensors are located in the water or soil, they are expected to behave differently. By identifying the strain distribution, the interface between the water and soil could be located, from which the soil elevation can be decided.

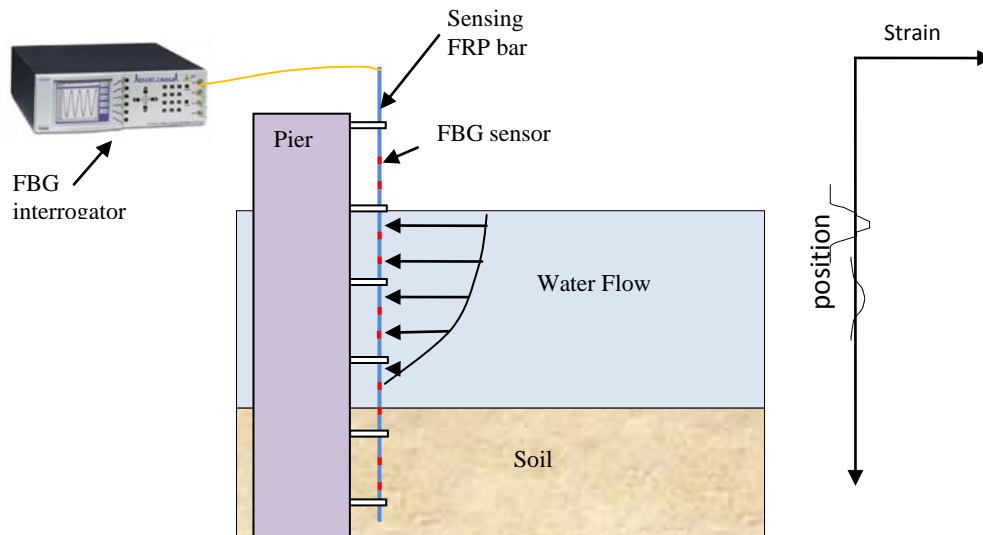


Figure 27
Concept of scour monitoring using FBG sensors

Test Configuration

The FRP bar with an economical sensor array can be placed adjacent to or at some distance from structural elements of bridge piers, foundations, or abutments. In order to investigate the applicability and sensitivity, two designs have been developed as follows:

The first design adopted a FRP bar clamped on the steel tube. The FRP bar with FBG sensors is installed close to the steel tube by a number of clamps, as shown in Figure 28. This design is better for existing piers/piles. The FRP bar vertically standing in the water tank is held

with clamps on the steel tube or stick to the glass fiber reinforced polymer (GFRP) pipe. The steel tube and the GFRP pipe are fixed at the bottom. The lower part of FRP bar is buried in a sand container, and the rest of the tank is filled with water and air. The heights of water and sand are adjustable as needed. As shown in Figure 28, the bottom 1.31 ft. (0.4 m) of the FRP bar is in the sand and the top 1.31 ft. (0.4 m) is in the water. FBG sensors are located along the FRP rebar with an interval of 0.66 ft. (0.2 m). The shaking table exerts the stroke simulating the water flow action. A velocimeter is used to measure the water velocity.

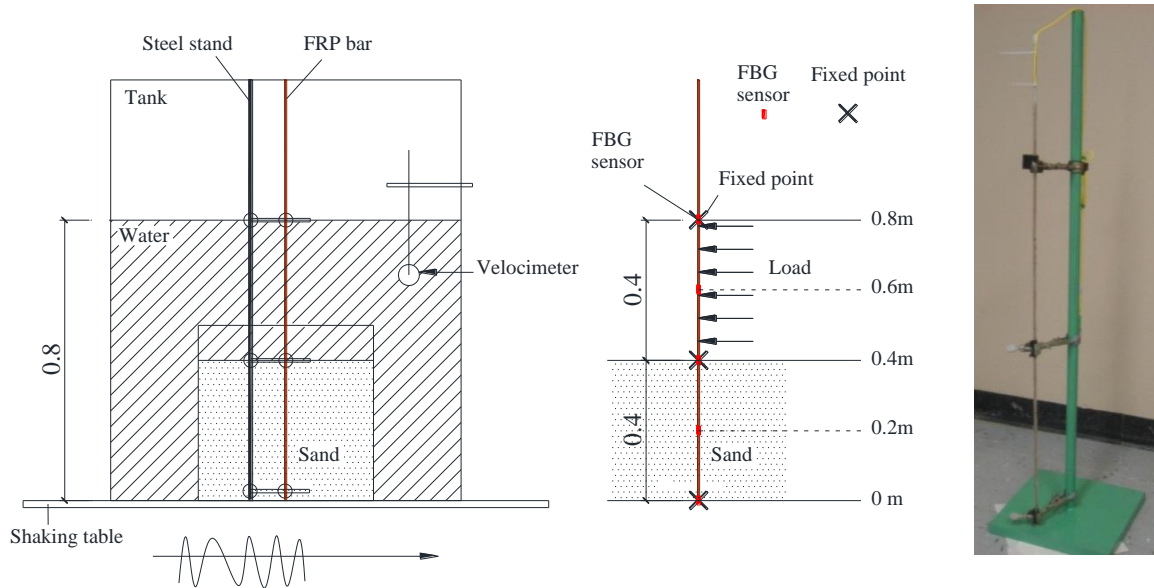


Figure 28
Design of FRP bar on steel tube

The second design adopted a FRP bar stick to the GFRP pipe. The FRP bar with FBG sensors are glued on the GFRP pipe in a certain interval as shown in Figure 29. This design is better for new foundations, with which the sensors are buried together. A pipe made of glass fiber reinforced polymer (GFRP) buried in sand was used to simulate the pile structure in soil, which is schematically depicted in Figure 29. A fiber reinforced polymer (FRP) bar attached with FBG sensors was mounted on the GFRP pipe at 0.0 ft. (0.0 m), 1.31 ft. (0.4 m), and 2.62 ft. (0.8 m) to measure the response of water impact. Both the pipe and the bar were fixed on a steel plate at the bottom. To simulate the water flow action, a shaking table was used to exert the stroke to the water tank sitting on the table. The water in a real river flows in one direction, but goes back and forth in the tank. In order to reduce the drag force of water, the specimen was put close to one side in the tank. Five sensors were deployed both on the GFRP pipe and the FRP bar in an interval of 0.66 ft. (0.2 m), namely, at the position of 0.0 ft., 0.66 ft. (0.2 m), 1.31 ft. (0.4 m), 1.97 ft. (0.6 m), and 2.62 ft. (0.8 m). For tests in water, the specimen was partially buried in a sand container and then submerged in the water tank. The heights of water and sand were adjusted as needed. Figure 29 shows an example where

the bottom 1.31 ft. (0.4 m) was in the sand and the top 1.31 ft. (0.4 m) was in the water. A velocimeter was also used to measure the water velocity. Figure 30 shows the test specimen and layout. The property of the GFRP pipe is: outer diameter = 4.5 in. (0.114 m), inner diameter = 4 in. (0.102 m) and the axial Young's modulus obtained through the material test is $1.13E06 \text{ k/ft}^2$ (5.4 GPa). The frequency filter is 250 Hz.

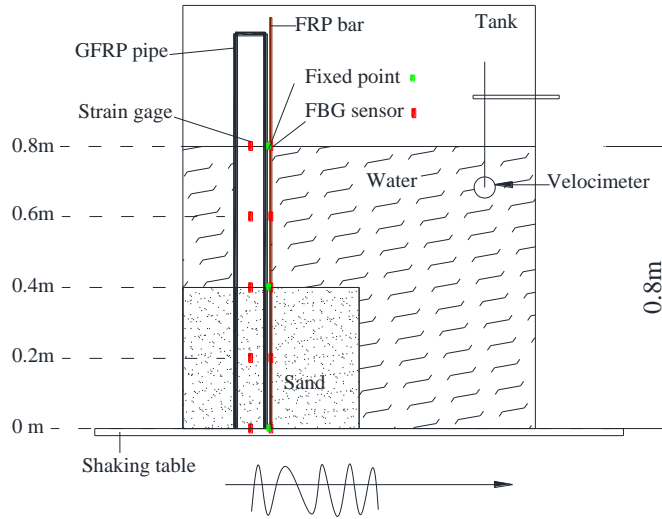


Figure 29
Schematic drawing of test design



Figure 30
Test specimen and layout on shaking table

Three monitoring mechanisms were tested. The first one detected the scour occurrence through the frequency change by clicking the GFRP pipe. The second one was the bending moment mechanism due to the static loading or the water flow as shown in Figure 31(a).

Herein a force was applied on the top of the pipe to produce the bending moment. The third one was the high frequency response of the FBG sensors to water flow or debris impact as shown in Figure 31(b). A hanging weight was used to simulate the debris in river water, and the sensors on the FRP bar was specially designed for this mechanism.

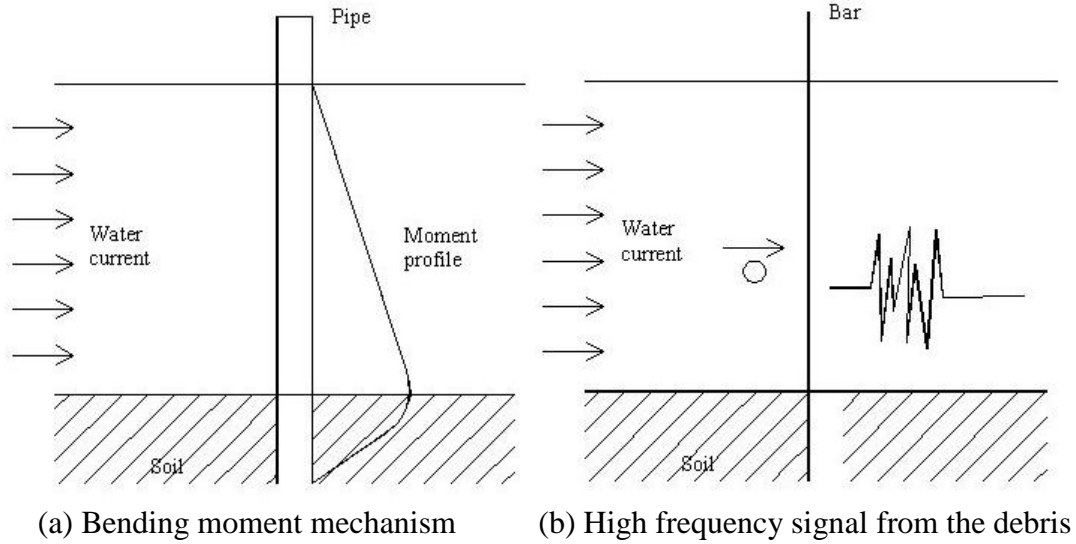


Figure 31
Monitoring mechanisms to be tested

Test Loads

Three types of loads were considered:

(1) Pseudo static loading

$$y = vt \tag{18}$$

where, v is the equivalent fluid speed, which is designed to be 1.64 ft/s (0.5 m/s), 1.23 ft/s (0.375 m/s), 0.82 ft/s (0.250 m/s) corresponding to line I, II, and III, respectively.

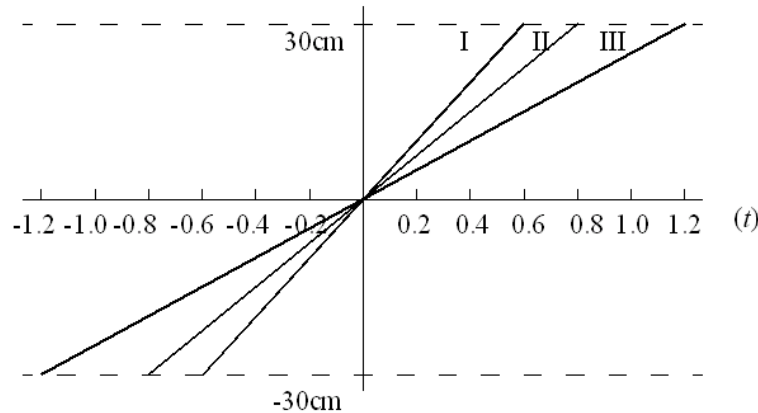


Figure 32
Pseudo static loading

(2) Noise

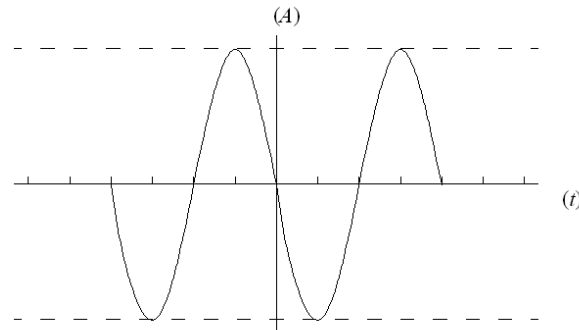


Figure 33
Noise loading

The noise considered here is, $y = A\sin(2\pi ft)$, where f is the fluid frequency, A is the stroke amplitude of the shaking table. To keep the equivalent fluid speed the same, the frequency and the amplitude are chosen this way:

	Case 1	Case 2	Case 3	Case 4
f (Hz)	1	2	5	10
A (ft)	0.82	0.41	0.16	0.082

(3) Current drag force

$$f = \frac{1}{2} \rho C_D A U^2 \quad (19)$$

where, ρ = fluid density, A = structure projected area normal to the flow, U = uniform flow velocity, and C_D is a constant known as the drag coefficient. The drag coefficient C_D is a function of the Reynolds number as shown in Figure 34, Re based on mean current velocity and member diameter [90]. For a circular cylinder across the flow, D is the diameter of the cylinder.

$$Re = u_0 D / \nu \quad (20)$$

where, u_0 = water particle velocity amplitude, D = kinematic viscosity of water.

Table 3 shows dynamic and kinematic viscosity of water at various temperatures.

- $Re < 200$, laminar flow; smooth, constant fluid motion
- $200 < Re < 5000$, transition mode between laminar flow and turbulent flow (Figure 35)

- $Re > 5000$, fully turbulent flow, figures random eddies, vortices and other flow fluctuations.

Table 3
Dynamic and kinematic viscosity of water in SI units

Temperature - t - ($^{\circ}C$)	Dynamic Viscosity - μ - ($N\ s/m^2$) $\times 10^{-3}$	Kinematic Viscosity - ν - (m^2/s) $\times 10^{-6}$
0	1.787	1.787
5	1.519	1.519
10	1.307	1.307
20	1.002	1.004
30	0.798	0.801
40	0.653	0.658
50	0.547	0.553
60	0.467	0.475
70	0.404	0.413
80	0.355	0.365
90	0.315	0.326
100	0.282	0.294

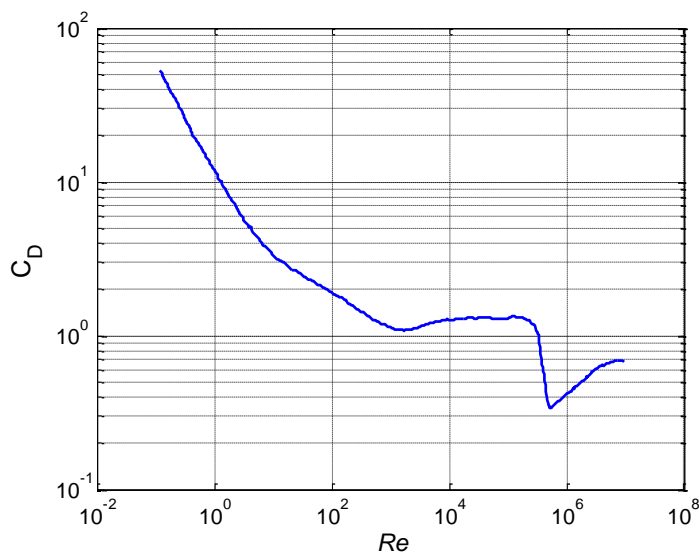


Figure 34
Drag coefficient for a smooth circular cylinder in steady flow



Figure 35
Turbulent flow around an obstacle

FRP Bar Response

The FRP bar with a length of 1.64 ft. (0.5 m), fixed at two points, was subjected to the loading from the water flow. The frequency of the bar can be obtained as,

$$f = \frac{1}{2\pi} \sqrt{\frac{k}{m}} \quad (21)$$

where, m is the mass, k is rigidity, $k = \frac{24EI}{l^3}$, and l is half of the length between the two fixed points. E is Young's modulus, 97 GPa; I is moment of inertia, for round cross section, $I = \frac{\pi D^4}{64}$ where D is the section diameter, 0.24 in; $I = 7.41 \text{ E-9 ft}^4$. When the length is 1.64 ft, the frequency of the rebar is listed in the table below with differential diameter.

Table 4
Rebar frequencies

Diameter (in)	1 st (Hz)	2 nd (Hz)	3 rd (Hz)	4 th (Hz)	5 th (Hz)
0.275 (7 mm)	63.142	174	345	575	966
0.315 (8 mm)	72.162	199	395	658	1105
0.354 (9 mm)	81.182	224	444	740	1243
0.394 (10 mm)	90.202	249	493	822	1381
0.433 (11 mm)	99.222	274	543	904	1519

The bending moment along the FRP bar can be calculated as

$$M_l = \frac{ql^2}{12} \left[-1 + 6\left(\frac{x}{l}\right) - 6\left(\frac{x}{l}\right)^2 \right] \quad (22)$$

Where q is the load density, for $x = 0$ and $x = l$, $M_l = -\frac{ql^2}{12}$, for $x = l/2$, $M_l = \frac{ql^2}{24}$.

The strain can be calculated by $\varepsilon = \frac{My}{EI}$.

Therefore, at 20 °C, the strain at $x = 0$ under different water velocity can be obtained as,

Water velocity(ft/s)	0.82 (0.25 m/s)	1.64 (0.5 m/s)	2.46 (0.75 m/s)	3.28 (1 m/s)
Re	1500	3000	4500	6000
C_D	1.09	1.14	1.21	1.24

$q(\text{lb/ft})$	13.98	58.93	139.78	253.53
$M(\text{lb}\times\text{ft})$	2.95	13.28	31.72	57.53
$\varepsilon(\text{m/m}\times 10^6)$	2	9	20	38

From the next table, the critical scour speed is about 1.64 ft/s.

Table 5
Incipient motion formulas

Reference	Formula	Vc(ft/s)
Neill (1998)	$V_c = \left(\frac{Y}{d}\right)^{0.167} [24.55(S_s - 1)d]^{0.5}$	1.81
Melville (1998)	$V_c = 5.75u_{*c} \log(5.53 \frac{Y}{d_{50}})$ $u_{*c} = 0.0115 + 0.0125d_{50}^{1.4} (0.1\text{mm} < d_{50} < 1\text{mm})$ $u_{*c} = 0.0305d_{50}^{0.5} - 0.0065d_{50}^{-1} (1\text{mm} < d_{50} < 100\text{mm})$	1.84
Julien (1995)	$\hat{\sigma}_{*c} = 0.5 \tan \epsilon \quad d_* < 0.3$ $\hat{\sigma}_{*c} = 0.25 d_*^{-0.6} \tan \epsilon \quad 0.3 < d_* < 19$ $\hat{\sigma}_{*c} = 0.013 d_*^{0.4} \tan \epsilon \quad 19 < d_* < 50$ $\hat{\sigma}_{*c} = 0.06 \tan \epsilon \quad d_* > 50$ $d_* = d_{50} [(G-1)g / i^2]^{1/3}$ $u_{*c} = [\hat{\sigma}_{*c}(G-1)gd_{50}]$ $V_c = 5.75u_{*c} \log(5.53 \frac{Y}{d_{50}})$	1.75

Scour Monitoring Instrumentation Design for Field Application

Scour is one of the main causes of bridge failures. Developing a real-time, reliable, and robust system is very desirable for local scour monitoring. It also needs to be easily installed in a riverbed near the bridge piers or abutments and collect the data safely. To this end, an innovative scour monitoring system including the instrumentation design, is proposed using fiber Bragg grating (FBG) sensors. In this scour monitoring system, the application of FBG sensors can make the monitoring flexible, stable, and durable in harsh environments with the advantages of lightweight, highly temperature and radiation tolerant, and, especially, immunity from electromagnetic interference. In addition, the protection measures designed in the system are able to protect the sensors away from floating debris in the water. Based on the wavelength response and multiplexing capability, FBG sensors can be easily multiplexed in a series of arrays along a single optical fiber to reduce the possible attenuation during the signal transmission in a long cable length. In contrast to other sensor networks, the proposed design can provide a real-time monitoring for the entire scouring process to correctly observe the maximum scour depth during floods.

In order to measure and monitor scour depth variations including deposition (refilling) process, three designs for a scour monitoring system using fiber Bragg grating (FBG) sensors are discussed in this study. By a comparative study, one of them is recommended in this study and its instrumentation manufacture process is also introduced in details. Using this recommended design, the advantages of FBG sensors for monitoring, such as immunity from electromagnetic interference and multiplexing capability, can be fully utilized. Both scour depth variations and entire scour development process including deposition process can be correctly monitored in real time by continuously identifying the locations of emerging FBG sensors from the riverbed. A reliable sensor protection measure is also designed for FBG sensors in harsh environments, especially in floods. Finally, a verification test using a flume is carried out in the laboratory and three experimental cases are conducted to demonstrate the capability of FBG sensors and applicability of the recommended scour monitoring system.

Fiber Bragg Grating Sensor

Fiber Bragg gratings are made by laterally exposing the core of a single-mode fiber to a periodic pattern of intense ultraviolet light [87], [90]. The exposure produces a permanent increase in the refractive index of the fiber's core, creating a fixed index modulation according to the exposure pattern. This fixed index modulation is called a grating. At each periodic refraction change, a small amount of light is reflected. All the reflected light signals combine coherently to one large reflection at a particular wavelength when the grating period is approximately half the input light's wavelength. This is referred to as the Bragg condition, and the wavelength at which this reflection occurs is called the Bragg wavelength. Light signals at wavelengths other than the Bragg wavelength, which are not phase matched, are essentially transparent or transmitted. The principle of FBG sensors is shown in Figure 36.

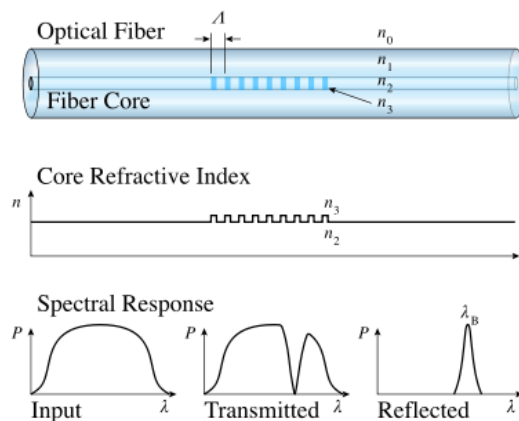


Figure 36
Work principle of FBG sensors

The Bragg wavelength λ_B depends both on the physical characteristics of the fiber and geometrical characteristics of the grating:

$$\lambda_B = 2n_e\Lambda \quad (23)$$

where, n_e = effective refractive index of the grating in the fiber core; and Λ = grating period. Both the effective refractive index and grating period vary with the change in strain $\Delta\varepsilon$, temperature change ΔT , and pressure change ΔP , imposed on the fiber. An applied strain and pressure will shift the Bragg wavelength through expansion or contraction of the grating periodicity and through the photo elastic effect. Temperature affects the Bragg wavelength through thermal expansion and contraction of the grating periodicity and through thermal dependence of the refractive index. If only the dominant linear effects of these three factors on FBG sensors are considered, neglecting higher-order cross-sensitivities, the amount of Bragg wavelength shift can be given by [92]:

$$\Delta\lambda_B / \lambda_B = K_\varepsilon\Delta\varepsilon + K_T\Delta T + K_P\Delta P \quad (24)$$

where, K_ε , K_T , and K_P = respective wavelength sensitivity coefficients for strain, temperature, and pressure for FBG sensors, respectively, which are further given by:

$$K_\varepsilon = \{1 - 0.5n_e[\rho_{12} - \nu(\rho_{11} - \rho_{12})]\}\lambda_B \quad (25a)$$

$$K_T = (1 + \xi)\lambda_B \quad (25b)$$

$$K_P = [-(1 - 2\nu) / E + n_e^2(1 - 2\nu)(2\rho_{12} + \rho_{11}) / 2 / E]\lambda_B \quad (25c)$$

where, ρ_{11} and ρ_{12} = components of the fiber optic strain tensor; ν = Poisson's ratio; ξ = thermo-optic coefficient; and E = Young's modulus.

In equation (24), even if assuming the pressure unchanged ($\Delta P = 0$), temperature and strain still cannot be measured simultaneously with one single grating since only one sensing parameter, wavelength shift, is required in the FBG sensor application. To separate the strain signal from the temperature signal, different compensation methods of temperature effects have been reported in the literature [92-96]. Practically, with a matrix inversion technique, most of the applications utilize two superimposed FBG sensors written at two different wavelengths to decouple the strain and temperature [92], [93], [95], [96].

Therefore, fiber Bragg gratings, i.e., FBG sensors, can be used as direct sensing elements for strain and temperature. Based on the work principle introduced above, applying FBG sensors to a scour monitoring system in the present study can give such advantages as below:

- (1) High resolution, dynamics, and accuracy. The resolution of FBG sensors, the capability of detecting a very small variation of the measured quantity, can be of 0.1 parts per million (ppm), resulting in $0.1\mu\epsilon$ of minimum measurable deformation. The dynamics of FBG sensors, the capability to measure a given quantity in a wide variation range with a specified resolution, allows length variations of over 10000 ppm, which makes a maximum measurable deformation over $\pm 10000\mu\epsilon$. The accuracy of FBG sensors, the maximum mismatch between the measured and the real value of a given quantity, is about 2 ppm, i.e., $\pm 2\mu\epsilon$. These performances make FBG sensors sufficiently sensitive to the pressure from flowing water/flood impact force.
- (2) Immunity to electromagnetic noise. This is an intrinsic characteristic of FBG sensors due to the material (glass) of which they are comprised. Because glass is a dielectric material, electromagnetic fields cannot induce electric currents into the fiber optics, nor modify the wavelength or the intensity of the optical signal. For this reason FBG sensors, compared to some traditional techniques such as TDR, are very suitable for installation in harsh environments such as flooding rivers.
- (3) Long term stability. Durability and stability is another important characteristic of FBG sensors. They can work for years without influence of negative effects due to aging, corrosion, and action of atmospheric agents that in general contribute to degrade the conventional sensors. This feature is especially important when applying FBG sensors in a sensing system of scour monitoring which usually requires a long term or permanent installation lasting for many years.
- (4) Long distance installation. Due to the very low attenuation of fiber optics, FBG sensors can be installed at a distance of the order of tens of km from the interrogator system via fiber optic cables. For this reason, it is possible to create a scour monitoring system with a reliable connection requirement of a very long distance.
- (5) Good physical performance. The small size and light weight of FBG sensors including fiber connection is a very useful feature when there is a very small space for the installation or in those cases where traditional sensors might load the structure. This makes FBG sensors an excellent choice in both surface-mounted and embedded sensing applications.
- (6) Multiplexing capability. FBG sensors are highly attractive also because of their multiplexing capability in a distributive sensing network. They can be easily multiplexed in a series of arrays along a single optical fiber. For scour monitoring, it

is a valuable and practical feature to create multiple sensing points in different depths using only one cable.

All the features of FBG sensors introduced above are important and will be applied in the following proposed scour monitoring system, which surely are the fundamental knowledge of this new design and make this new design more practical and effective over other scour monitoring systems.

Monitoring System and Instrumentation Design

Based on the discussion above, FBG sensors are identified as very useful and attractive devices to measure scour depths for the scour monitoring over other methods. Although FBG sensors have already demonstrated their advantages and applicability in many researches, their application in scour monitoring is actually very new, only a few pilot applications in Taiwan [61]. How to design an efficient and reliable scour monitoring system and instrumentation with FBG sensors is still a significant issue in the practical application. In addition, FBG sensors cannot be applied directly in the field because, after certain experimental evaluations, they are found to be unable to withstand the conditions encountered in floods due to their brittleness [61]. The present study is to design an innovative monitoring system not only to fully exploit all the advantages of FBG sensors in the scour monitoring but also to protect FBG sensors in the field. To this end, three designs of the scour monitoring system using FBG sensors are proposed. The recommended design will be given after a comparison.

Design 1

In this design, FBG sensors are arrayed at a certain interval along a single optical fiber in series on a steel bar (details in Figure 37). This steel bar is supported as a continuous beam using fixed joints inside a steel tube which is a hermetic space (B-B in Figure 37). Each FBG sensor in this system is covered by a waterproof rubber seal like a button, which goes through the steel tube from a hole (A-A and B-B in Figure 37). The detailed sketch of Design 1 is shown in Figure 37.

Based on this design, when the scour occurs, FBG sensors should emerge from the riverbed where they used to be buried in the soils. There are two phenomena that can be sensed by FBG sensors: the flowing water pressures and flowing water impact forces. Specifically, the flowing water pressures, through the waterproof rubber seal, can bend/deform the steel bar (dashed line in Figure 38) and this bending can be sensed as strain variations by the FBG sensors glued on the steel bar. The impact forces of flowing water toward the sensors can also be directly sensed by FBG sensors. Both of the sensed phenomena are regarded as the

significant signs to indicate the successful detection and monitoring of scour. Along with the development of scour, more and more FBG sensors emerge from the riverbed. Depending on the position of the emerging FBG sensors, it is easy to notice where the scour develops and the whole process of scour can also be monitored and recorded in real time. In other words, both the actual maximum scour depth and deposition process (soil backfilling) can be clearly observed in addition to the final scour depth after floods. The waterproof rubber seal including an L-shaped steel bumper should be able to prevent damages to FBG sensors in case of a flood flowing at an excessive velocity beyond the protection criterion, or if debris in the flow strikes with excessive impact forces. The monitoring principle of this design is shown in Figure 38.

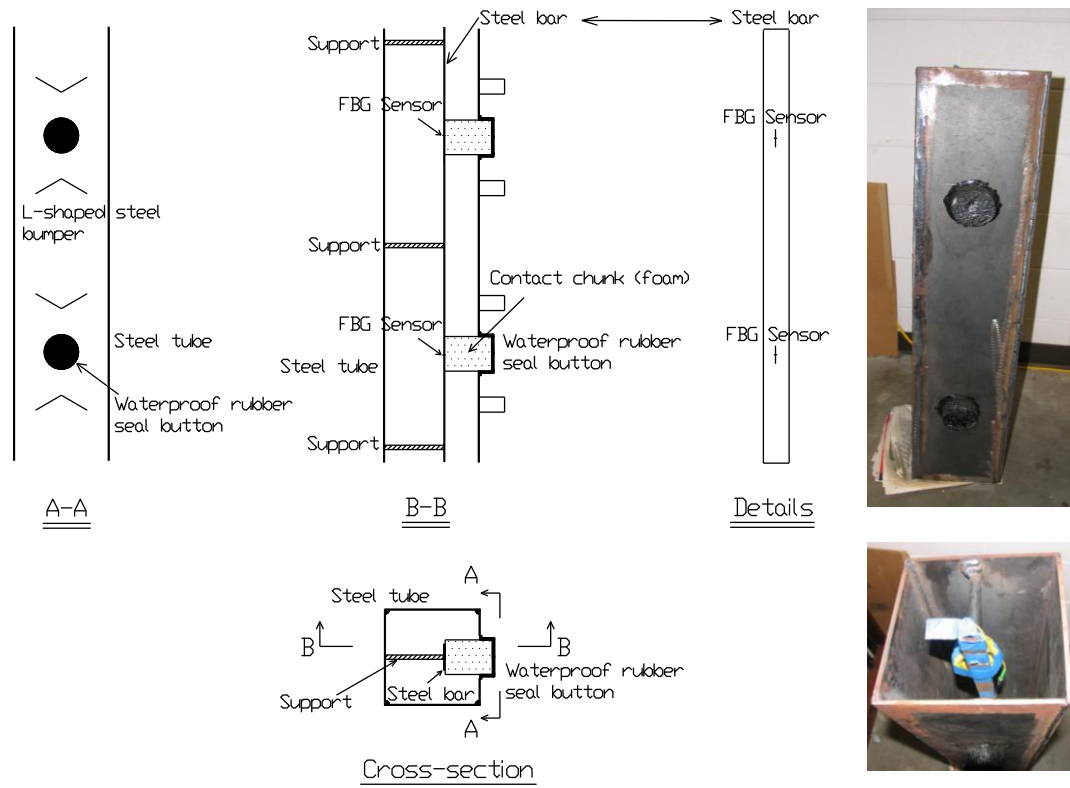


Figure 37
Detailed sketch of Design 1

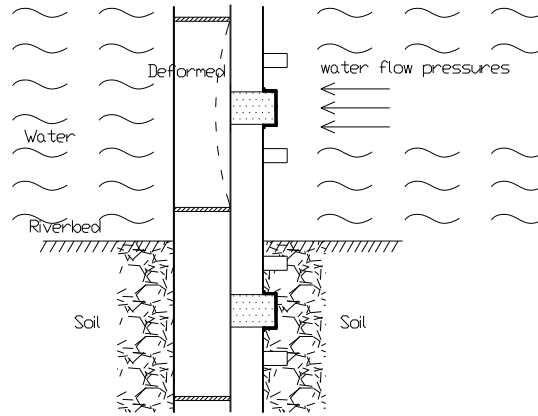


Figure 38
Monitoring principle of Design 1

However, this design has a few problems when it comes to practical applications. One of them is the influence from the hydrostatic pressures in the water or rivers, which may make the waterproof rubber seal buttons not function as intended. Due to a tube design which is a hermetic space, the hydrostatic pressures applying on FBG sensors on the steel bar through the buttons are actually very significant especially near the bottom of rivers. The steel bar or other structure components not only sustain the flowing water pressures and flowing water impact forces but also the hydrostatic pressures which may be much higher than the former. However, as a matter of fact, the hydrostatic pressures are nothing but negative for the instrumentation design, which could make the steel bar unnecessarily strong (high thickness or large width) and also make the buttons relatively insensitive to the external forces. For instance, if the highest velocity of flowing water (usually in floods) is assumed as 11.48 ft/s (3.5 m/s) and the cross-section area of waterproof rubber seal is 0.054 ft² (0.005 m²) (radius = 0.13 ft), the flowing water force acting on a waterproof rubber seal or an FBG sensor can be calculated as about 67.4 lb. (300 N) based on the following equation:

$$F_D = C_D A_s \rho \frac{V^2}{2} \quad (26)$$

where, F_D = flowing water force acting on a waterproof rubber seal or an FBG sensor; C_D = coefficient representing the pressure and friction effects, which is related to the Reynolds number, herein is about 1.0 based on the shape of waterproof rubber seal and Reynolds number; A_s = cross-section area of waterproof rubber seal; ρ = water density; and V = flowing water velocity.

Based on the strength design, this 67.4 lb. of flowing water force requires 0.13 ft. (0.040 m) for the width of steel bar and 0.197 in. (0.005m) for its thickness. However, if assuming 13.12 ft. (4 m) river depth after scour, 1.64 ft. (0.5 m) interval between two sensors, and still

the same cross-section area of waterproof rubber seal, the hydrostatic pressures only results in a force that requires at least another 0.13 ft. (0.040 m) increase for the width of steel bar and another 0.197 in. (0.005 m) increase for its thickness. This is obviously unnecessary and uneconomical. In addition, the doubled thickness obviously can weaken the mechanical response (strains) of the steel bar, which may reduce the sensing sensitivity of FBG sensors for scour monitoring.

Design 2

Similar to Design 1, FBG sensors in Design 2 are also arrayed at a certain interval along a single optical fiber in series on a steel bar (A-A and B-B in Figure 39). However, there are two major differences in Design 2. Firstly, in order to solve the hydrostatic pressure problem, two channel beams are used to form a hollow structure where the flowing water can pass through the tube (Cross-section in Figure 39). By doing this, the hydrostatic pressures on the monitoring system, especially on the steel bar, can be totally ignored because it is self-balanced. Secondly, the steel bar is changed from a supported continuous beam with two fixed joints to a cantilever beam, which is more sensitive to the flowing water pressures and impact forces. Steel protection sticks are added on the channel beams to prevent direct damage to the FBG sensors if debris in the flow strikes with excessive impact forces (A-A in Figure 39). The detailed sketch of Design 2 is shown in Figure 39.

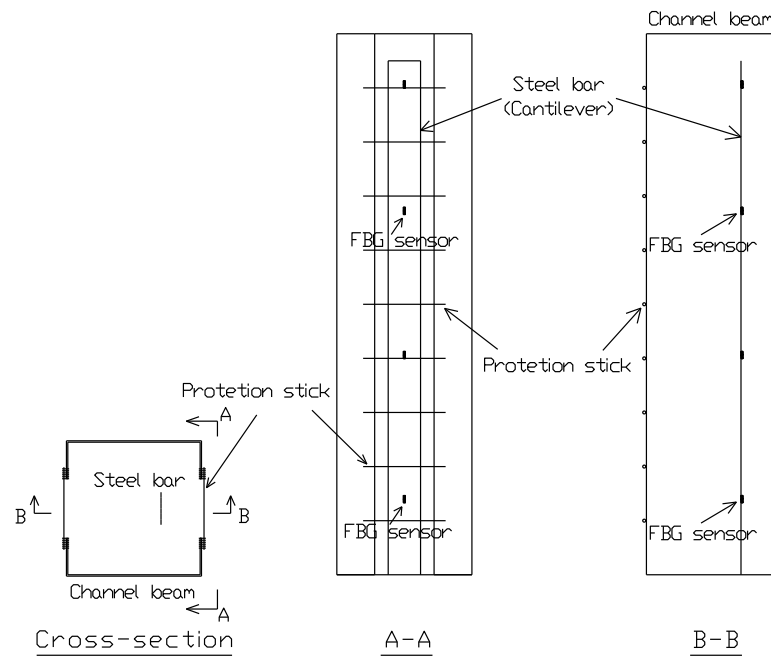


Figure 39
Detailed sketch of Design 2 segment

Similar to Design 1, the scour monitoring based on this design is also conducted by sensing the same flow information from the emerging FBG sensors. Along with the scour development, FBG sensors emerge from the riverbed one after the other from the top to bottom of the steel bar. Considering the steel bar as a cantilever, the later emerging FBG sensors, more towards the bottom of the cantilever beam, obviously can sense more response from the flowing water pressures and impact forces (dashed line, i.e., deformed steel bar, in Figure 40). This not only shows where the scour develops but also can be regarded as an increasing alert along with the constantly developing scour. Figure 41 gives a schematic drawing for different responses of every FBG sensors when the riverbed locally drops due to the scour development (in the ideal condition). It is easy to understand that the whole process of scour (the actual maximum scour depth and deposition process) can be also monitored and recorded by this design.

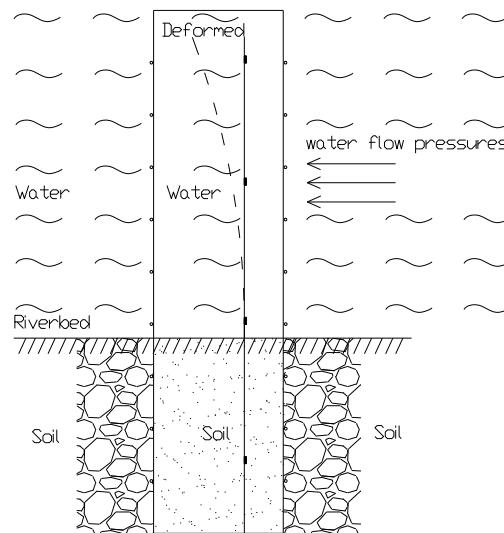


Figure 40
Monitoring principle of Design 2

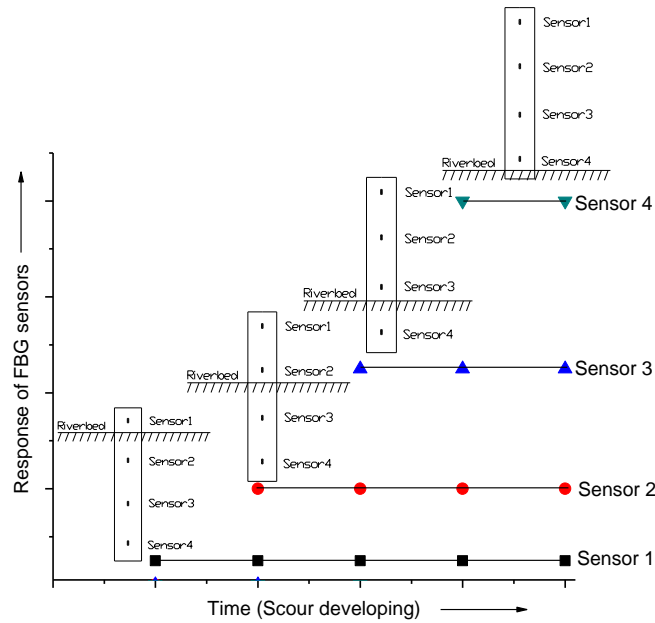


Figure 41
Schematic description for the response of each FBG sensor

However, after the preliminary test in the laboratory, it was found that the protection sticks could stop the soil in the hollowed tube from flowing away; as a result, the FBG sensor will not function as intended. This would cause a significant influence to the monitoring accuracy on the entire scour process. If simply removing the protection sticks, FBG sensors should be easily damaged in flooding environments.

Design 3 (recommended)

The main monitoring principle and system design in Design 2 are still applicable in Design 3. However, much attention was paid here to the issue of how to assure the soil level inside the tube was exactly the same as the riverbed level outside the tube. To this end, the steel bar was moved near to the open side of the tube in order to make FBG sensors as close as possible to the soil outside the tube, which represents the real riverbed level (A-A and B-B in Figure 42). There were no protection sticks in this design. Instead, a protection system was directly used on the surface of the FBG sensors on the steel bar. Therein, epoxy resin was used as a sensor protection to fulfill the groove formed by two pieces of steel angles attached on the steel bar (Figure 43). By doing this, the FBG sensors can be entirely covered by epoxy resin to prevent direct damage to the FBG sensors from the debris in flowing water. The two steel angles themselves can also stop the direct hit to FBG sensors from the debris.

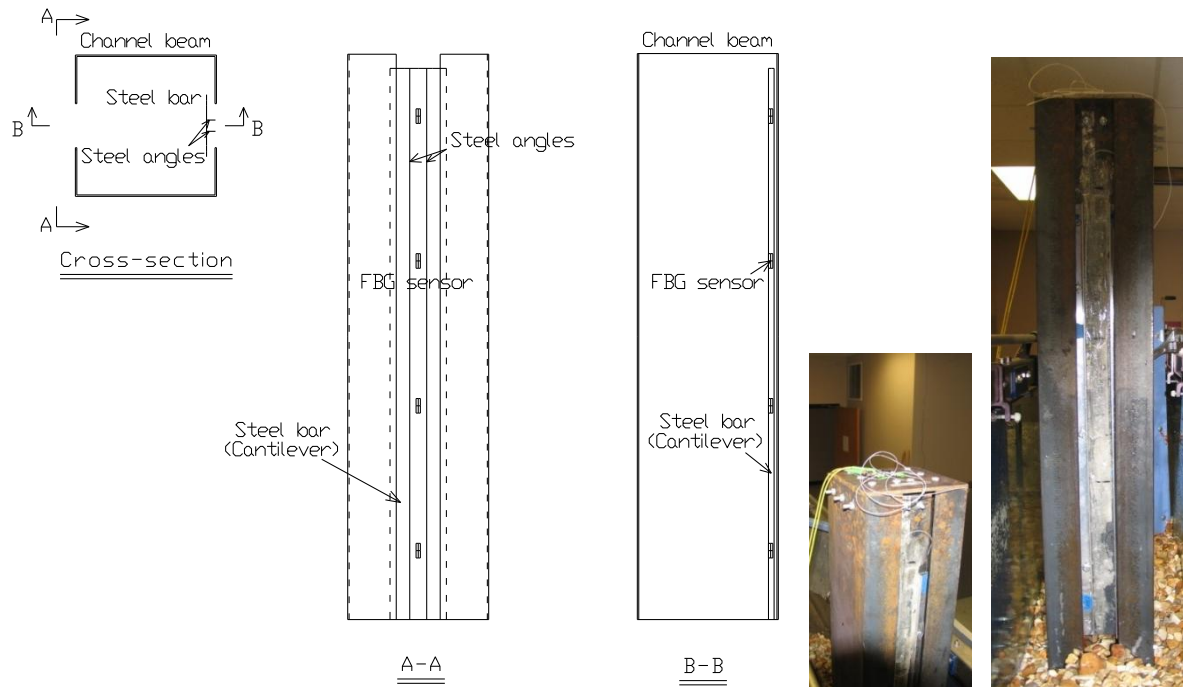


Figure 42
Detailed sketch of Design 3

As in the previous designs, the scour monitoring based on this design is conducted by sensing the flowing water information from the emerging FBG sensors. As discussed in Design 2, a cantilever design of the steel bar can reserve all the advantages introduced earlier. The whole process of scour (the actual maximum scour depth and deposition process) can be monitored and recorded in real time under a reliable sensor protection system by this design. The monitoring principle of this design is shown in Figure 44.

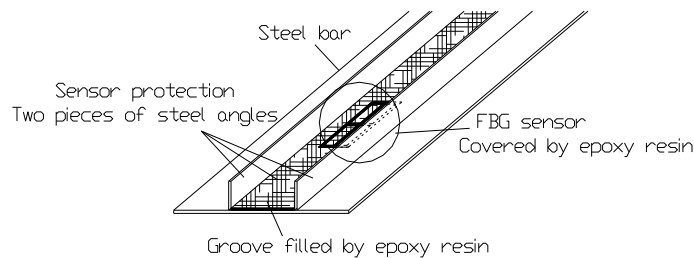


Figure 43
Design of sensor protection system

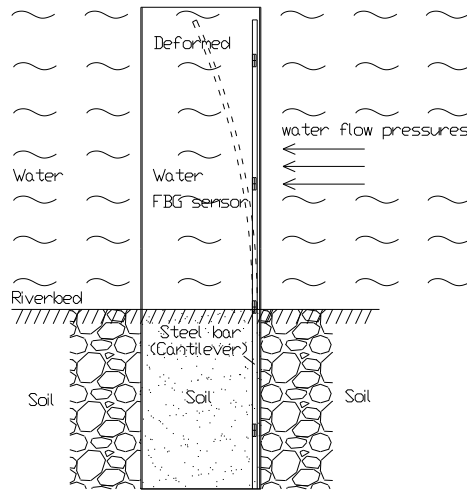


Figure 44
Monitoring principle of Design 3

Table 6 shows the comparison results among the three scour monitoring designs introduced earlier.

Table 6
Comparison results

Designs	Design 1	Design 2	Design 3
Eliminating unnecessary hydrostatic pressures	NO	YES	YES
Sensing sensitivity for flowing water	NO	YES	YES
Sensing accuracy for riverbed level	YES	NO	YES
Showing increasing alert when scour develops	NO	YES	YES
Monitoring whole process of scour	YES	YES	YES
Protecting FBG sensors	YES	NO	YES

As can be seen from the comparison in Table 6, Design 3 has many advantages over the other two designs especially from the viewpoints of sensing sensitivity, sensing accuracy, and sensor protection system. In the present study, Design 3 is highly recommended for the scour monitoring using FBG sensors and verification in a laboratory test.

Experimental Setup

Usually, at least 13.12 ft. (4 m) depth below the riverbed needs to be monitored for the purpose of scour detection. It is inconvenient to build the instrument with the whole depth/length all at once. In the present study, the proposed instrument is manufactured as several 1m-depth-segments. Each segment has a complete scour monitoring system with FBG sensors introduced in Design 3. Each segment is assembled by several steel components using screws, which is more flexible than using weld (Figure 45). Through connecting every

segment in field, the monitoring instrument with any required depth/length can be easily installed for a specific bridge (Figure 45).

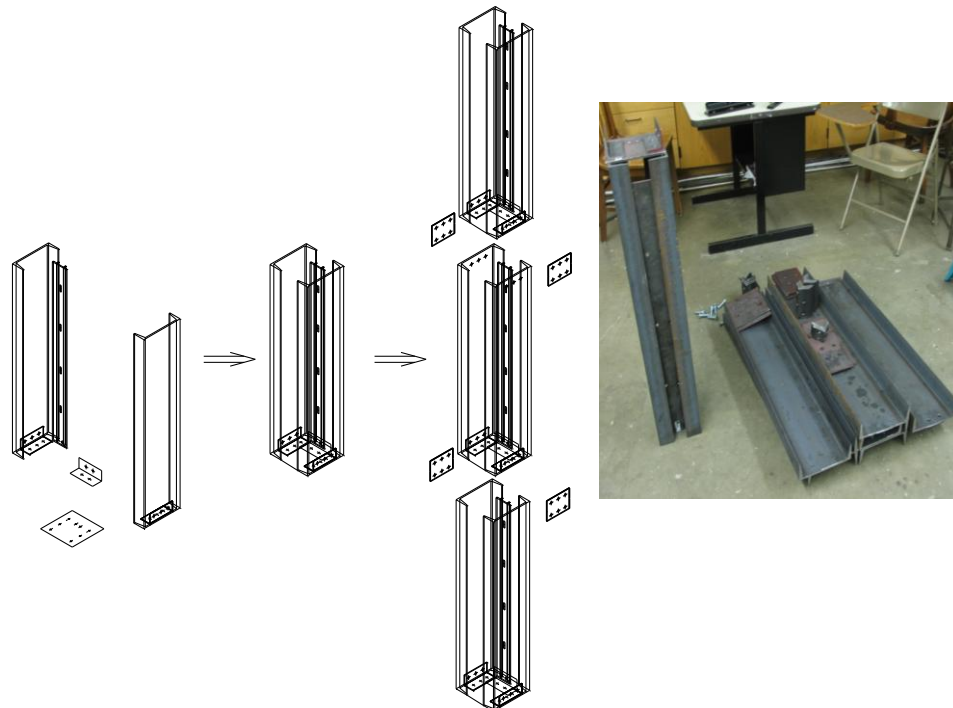


Figure 45
Instrumentation assembling

Based on the recommended design of Design 3, installation of FBG sensors and building their protection system is another important process in the instrumentation manufacture. Figure 46 demonstrates this process in detail. Herein, FBG sensors manufactured by T&S Communication, Ltd. (Bandwidth@3dB: <0.3, Min. SLSR: > 15dB, Min. Reflectivity: >90%) and an arc fusion splicer (FSM-50S) manufactured by Fujikura, Ltd. are used to connect FBG sensors in series with connection protection.

The experiments were conducted in a 32.8-ft. (10-m) long, 1.31-ft. (0.4-m) wide, and 2.13-ft. (0.65-m) deep flume with glass sidewalls at LSU, which is shown in the left hand of Figure 47. The scour monitoring instrument was placed in the middle of the flume paved by sands and gravels with “riverbed” elevation of around 1.64 ft. (0.5 m) The prescribed discharge and its corresponding depth for each experimental case were controlled by adjusting the inlet valve and tailgate in the flume. Three sensors, each sensor with a desired wavelength, were mounted on the surface of a cantilevered steel bar and arranged in series along one single optical fiber. These three sensors, namely sensors 1, 2, and 3, were mounted at 1.82 ft. (0.55 m), 1 ft., and 0.18 ft. (0.055 m) away from the bottom of the cantilevered steel bar partially

submerged with the largest flowing water level of 1.97 ft. (0.5 m) in the experiment, see the right hand of Figure 47. The scour at riverbed can be simulated by washing away the sands and gravels through the flowing water in this experiment setup.

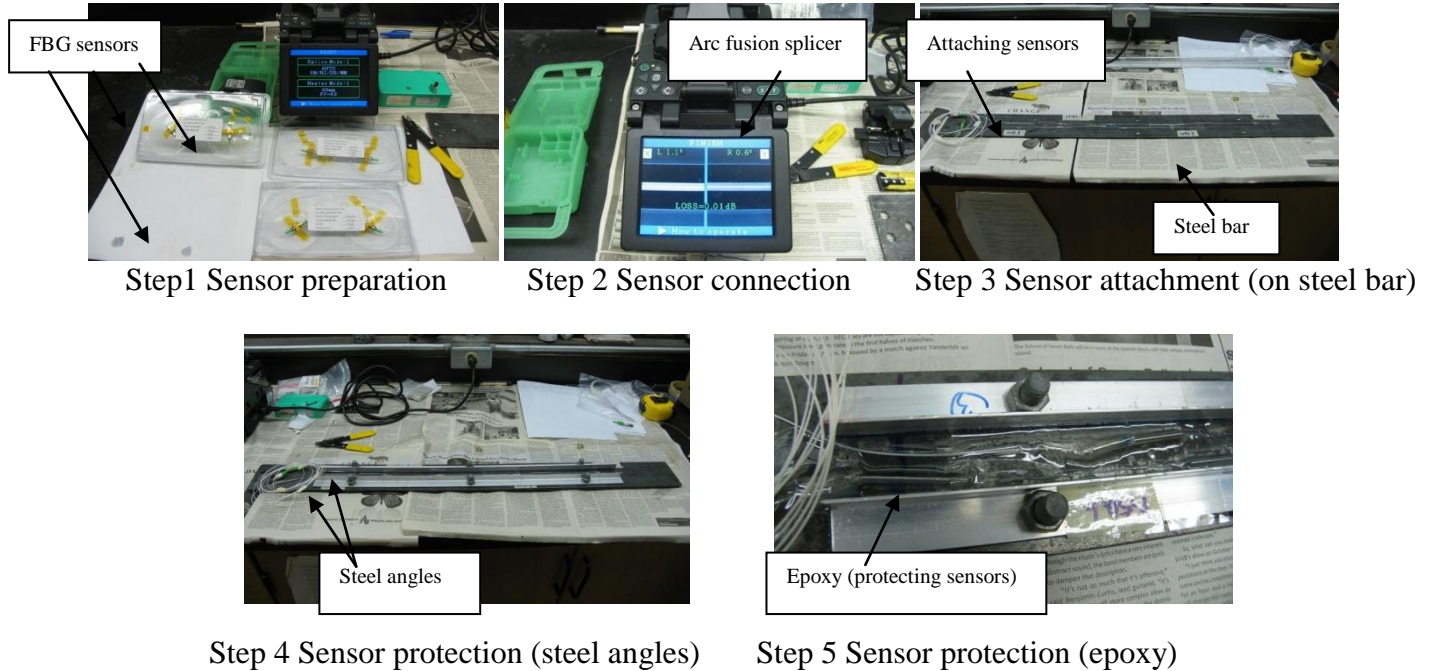


Figure 46

Installation of FBG sensors and their protection system

There were three runs, namely cases 1, 2, and 3, with different flowing water velocities and different discharge processes in this experiment. When the running water flowed towards the cantilevered steel bar in these cases, a deformation strain was generated by the bending moments and flowing water impact forces. If FBG sensors are buried below the riverbed surface, there is no or small response for FBG sensors. Once FBG sensors emerge from the riverbed due to the developing scour, the scour depth can be directly detected from the sensor responses, the corresponding varying wavelengths, and the sensor positions.



Figure 47
Water flume and experimental setup

Field Installation and Test

Based on the above instrumentation design and test in the laboratory, the third design is recommended for application in the field. Two 18-ft. (5.5-m) long instruments (similar to a pile) with FBG sensors are fabricated and driven besides the foundations of the field bridge. Each pile is assembled with six 3-ft. (0.92-m) long segments designed as the sample in the laboratory.

Bridge Description

The bridge shown in Figure 48, located in East Baton Rouge Parish, Louisiana, crosses over the Redwood Creek on Louisiana Highway 67. The bridge, built in 1965, is 300 ft. (91.4 m) long and consists of twelve 25-ft. (7.62-m) reinforced concrete slab spans supported by concrete pile bents with a reinforced concrete bent cap. The bent types consist of five square precast concrete piles with different sizes. The bents are skewed 75° relative to the roadway centerline.

Waterway information: The Redwood Creek in the vicinity of the bridge site is a medium [100- to 500-ft. (30.5-m to 152-m) wide] sinuous stream with a perennial flow habit. The streambed material is primarily sand with underlying clay. The channel boundaries are alluvial, and the floodplain is wide (greater than ten times the channel width). None of the pile bents are currently protected from scour. This bridge is susceptible to light drift build-up.

Scour history: Table 7 documents the soil conditions. The maximum scour of the bridge has occurred at Bent 5 in 2005, approximately 13.5 ft. (4.11 m) (as shown in Figure 49). The

record shows a general trend of channel degradation at Bents 2, 3, 4, and 5 that transits to a general trend of channel aggradation at Bents 9, 10, and 11. Substantial erosion adjacent to Bent 13 was observed during the Phase III site visit causing undermining of the cap. Typical erosion holes averaging from 2.5 ft. to 6 ft. (0.76 m to 1.83 m) deep were noted around the bents on each bank under the bridge. This site appears to have a history of bank erosion underneath the bridge.

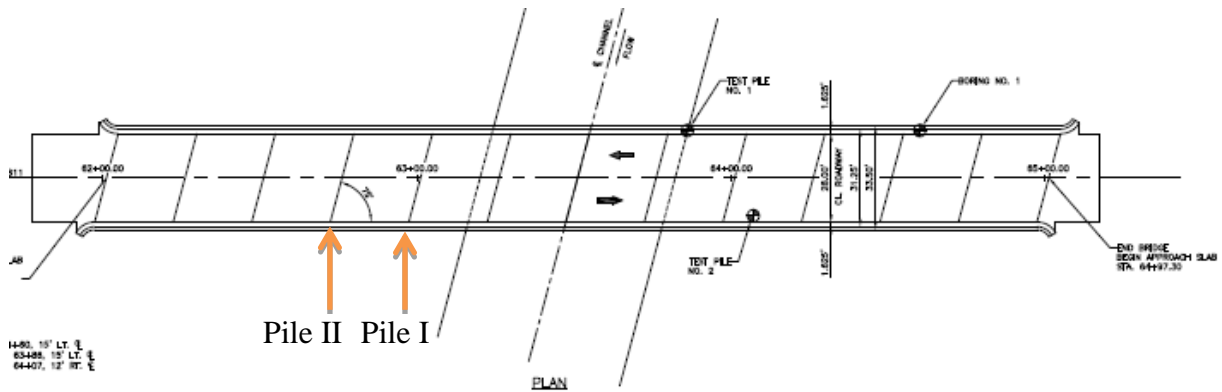


Figure 48
Bridge layout

Table 7
Soil condition

Bent No.	As-Built Ground Elev. 1965	Phase II Ground Elev. 1999	Current Ground Elev. 2009	Mudline Change ¹ (ft)	Phase II Predicted 100 Year Scour Elev. (ft)	Pile Tip Elev. (ft)	Pile Length (ft)	Critical Scour Elev. (ft)	Debris Critical?	Remaining Depth to Critical Scour Elev. ² (ft)	Soil Type for Remaining Depth to Critical Scour Elev.
1	94.2	94.0	95.7	-1.5	78.9	63.7	30.0	--	--	--	--
2	93.0	91.5	91.0	2.0	72.0	58.7	35.0	89.0	N	2.0	sand
3	86.0	82.0	79.9	6.1	70.0	48.7	45.0	72.8	Y	7.1	sand
4	80.0	76.0	71.7	8.3	67.8	43.7	50.0	69.0	Y	2.7	sand
5	74.0	71.0	68.4	5.6	62.8	43.7	50.0	65.8	Y	2.6	sand
6	66.5	70.0	69.1	-2.6	61.8	38.7	55.0	65.2	Y	3.9	sand
7	66.5	69.5	66.1	0.4	61.3	38.7	55.0	65.2	Y	0.9	sand
8	66.5	73.5	69.7	-3.2	65.3	38.7	55.0	65.2	Y	4.5	sand
9	76.0	79.5	78.3	-2.3	71.3	43.7	50.0	69.0	Y	9.3	sand
10	78.0	81.0	82.2	-4.2	72.8	48.7	45.0	72.8	Y	9.4	sand
11	82.0	84.0	85.3	-3.3	72.5	48.7	45.0	72.8	Y	12.5	sand
12	93.0	92.0	91.7	1.3	77.6	53.7	40.0	79.5	Y	12.2	sand
13	94.2	94.0	94.7	-0.5	82.6	53.7	40.0	--	--	--	--

1. Mudline Change = As Built Mudline Elev. - Current Mudline Elev.

2. Remaining Depth to Critical Scour Elev. = Current Mudline Elev. - Critical Scour Elev.

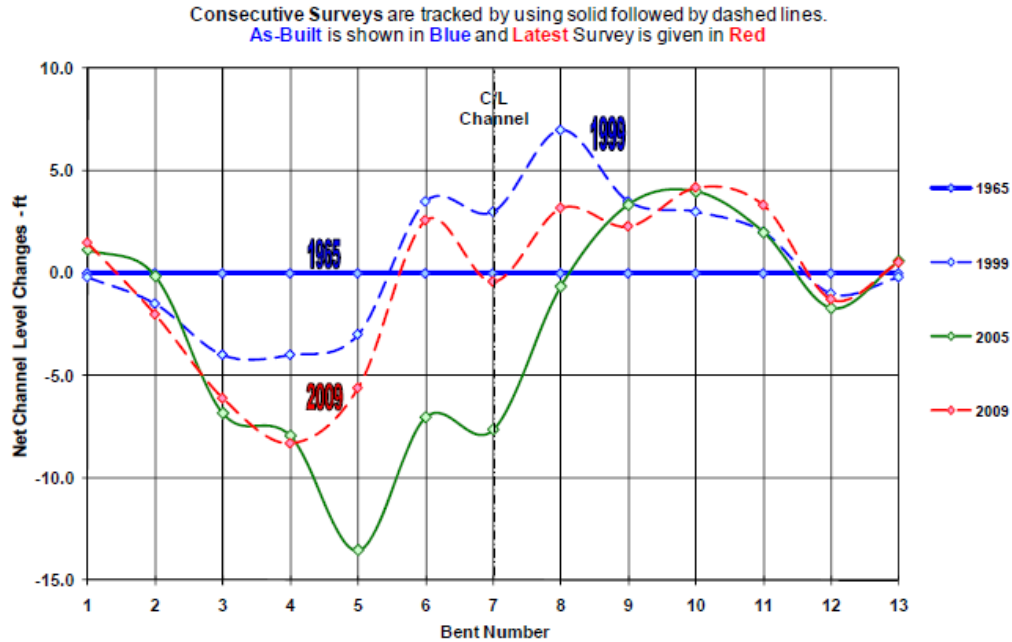


Figure 49
Pattern of ground line change

Data Acquisition Systems - FBG Interrogator

Strain measurements from the FBG sensors were collected using the si425 Optical Sensing Interrogator from Micron Optics, Inc. (Figure 50). It is a multi-FBG sensor system that can support up to 512 sensors on four fibers, powered by a high output power swept laser source. The current si425- 500 system has four functional channels on the main unit, which has a working wavelength range of 1510-1590 nm. The scan rate is 250 Hz for less than 100 sensors used simultaneously. An additional coupler extension module can increase the number of available channels further. This system can be controlled and monitored remotely through a complete set of Ethernet controls. The interrogator provides rapid, accurate measurements of hundreds of optical sensors in real time.

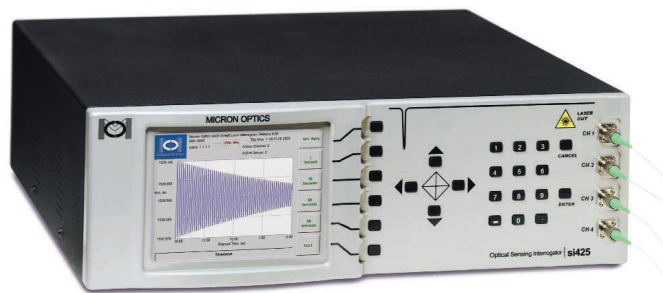


Figure 50
Si425 optical sensing interrogator

Instrument Fabrication and Sensor Preparation

As discussed earlier, the third design was selected for the field application. Two test piles were fabricated and each of them consisted of six 3-ft. (0.92-m) long segments [totally 18 ft. (5.5 m)]. In each segment, four sensors were attached on the steel plate and protected with epoxy as shown in Figure 51 (a). The four sensors were divided into two groups, each with two sensors were multiplexed in a series along a single optical fiber and parallel and independent to the other sensors. Six segments were then assembled into a test pile, as shown in Figure 51 (b) and (c). Before being transported to the bridge field, the cables connecting the FBG sensors were pulled to one end of the pile. After that, the sensors were tested using the FBG interrogator in the workshop, as shown in Figure 51 (d).



(a) Sensors and protection system



(b) Assemble test pile



(c) Sensor connection



(d) Sensor testing

Figure 51
Fabrication and sensor testing

In-situ Installation

The two test piles were transported to the bridge field by DOTD vehicles. With the help of District 61, DOTD, the two test piles were in position as shown in Figure 52 and Figure 53. Pile II (side) is near the downstream of the Bent 4, and pile I (middle) is near the downstream of Bent 5, as shown in Figure 48.



Instrument moving



Dig holes



Drive the middle pile



The middle pile in position

Figure 52
In-situ installation of the middle pile



Preparation using extractor



Preparation using drilling machine



Drive the side pile



The side pile in position

Figure 53
In-situ installation of the side pile

After the test piles were in position, the sensor cables were led through a tube to the bridge deck as shown in Figure 54, such that the future monitoring can be conducted on the deck even during the flooding process. Due to the fragility of the sensors, a few sensors were broken during the fabrication, transportation, and installation processes. After the two piles were in position, 10 sensors survived on the middle pile (Pile I), named as sensor I-1 to I-10, and 14 sensors for the side pile (Pile II), named as sensor II-1 to II-14 as shown in Figure 55.



The status after installation



Leading cables to the deck

Figure 54
The original status of instrument

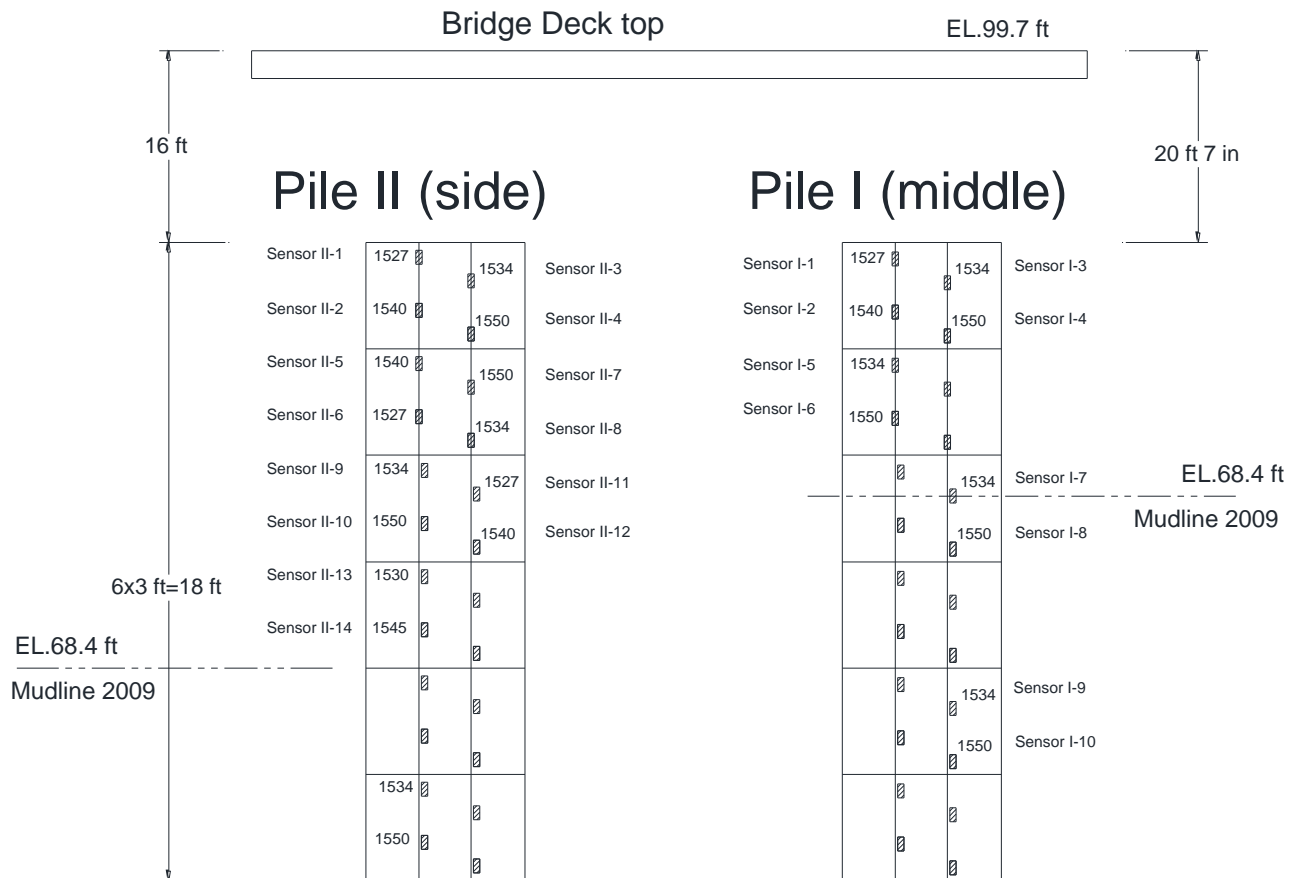


Figure 55
Sensor layout after installation

DISCUSSION OF RESULTS

Laboratory Test Results

Specimen Test

Before doing tests in the water tank, five tests were conducted on the FRP specimen to investigate the sensitivity of the sensors that respond to the click and water impact, as shown in Figure 56, Figure 68, and Figure 70. The specimen was fixed at one end with a clip using two rubber pads for holding, and free in the other end. Due to the elasticity of the rubber pads, the fixed end had a little rotation and was not rigid. Table 8 lists the detailed information, that is, test1~4 are clicking the specimen with different levels of force and different condition, and test 5 is the water flow impact test. The sampling frequency is 250 Hz.

Table 8
Test detailed information

	Description
Test 1	Click the specimen with gentle force
Test 2	Click the specimen with moderate force
Test 3	Click the specimen with heavy force
Test 4	Click the specimen with or without sand
Test 5	Water flow impact test

(1) Clicking test

The strain responses are shown in Figure 57~Figure 59. With increasing force, the responses increase accordingly. The wavelength amplitude of each test is about 60pm, 100pm and 300pm, respectively.



Figure 56
Clicking test of FRP specimen

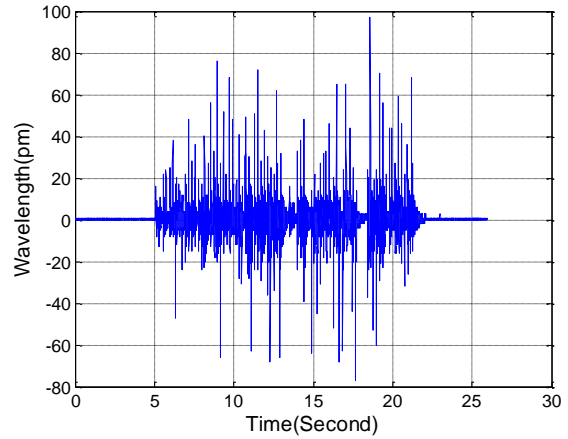


Figure 57
Strain response of gentle clicking

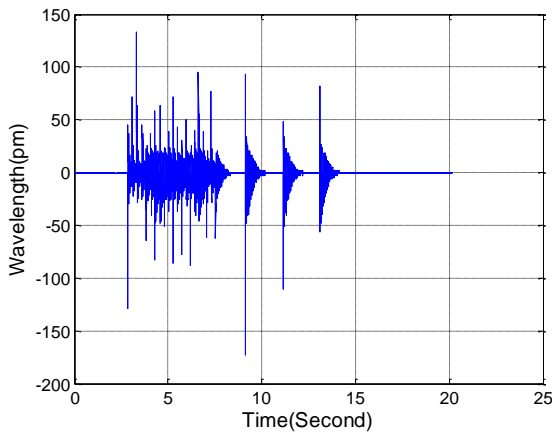


Figure 58
Strain response of moderate clicking

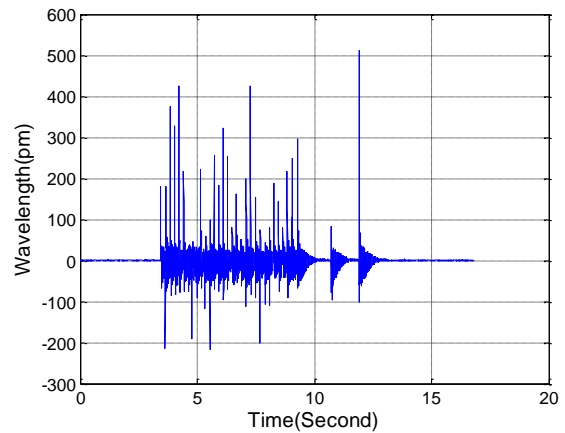


Figure 59
Strain response of heavy clicking

Fractions are picked from the response histories and its frequency characteristics are analyzed through FFT technique as shown in Figure 60~Figure 67. As shown in Figure 61, when the responses from two clicks overlap, broader frequency contents are identified. The fundamental frequency of the specimen with the boundary mentioned above is about 35Hz. The frequency identification has not been influenced evidently by the clicking force intensity, which means that slight click is sufficient to induce meaningful information.

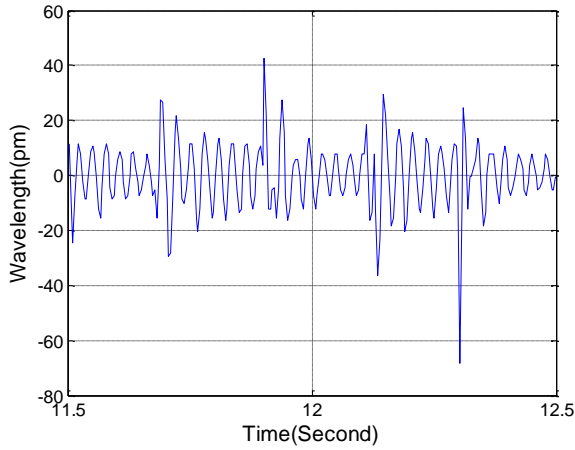


Figure 60

Strain response of test 1 at 11.5s~12.5s

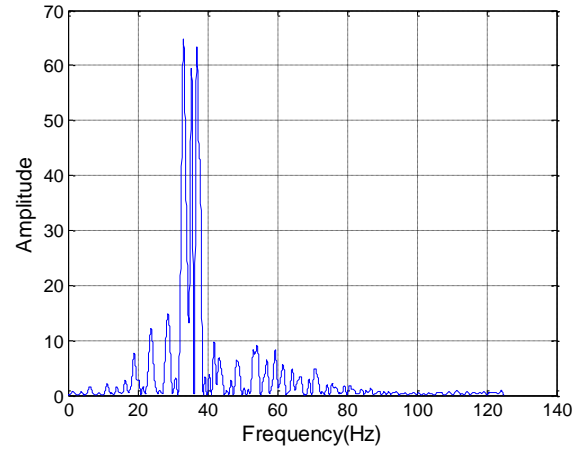


Figure 61

FFT of strain response of test 1 at 11.5s~12.5s

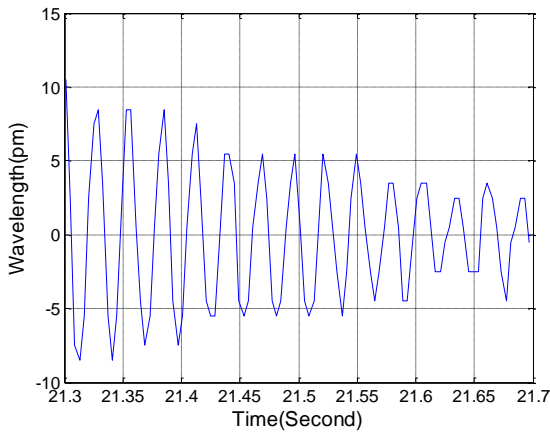


Figure 62

Strain response of test 1 at 21.3s~21.7s

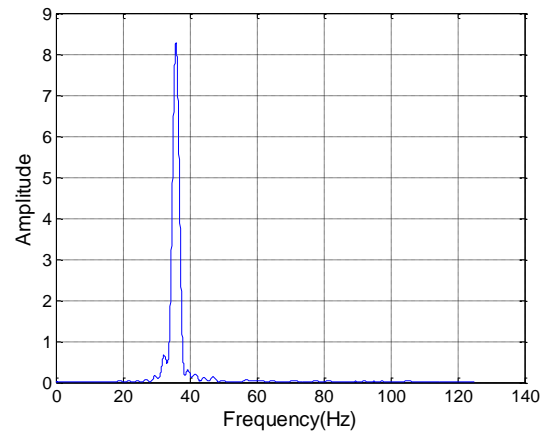


Figure 63

FFT of strain response of test 1 at 21.3s~21.7s

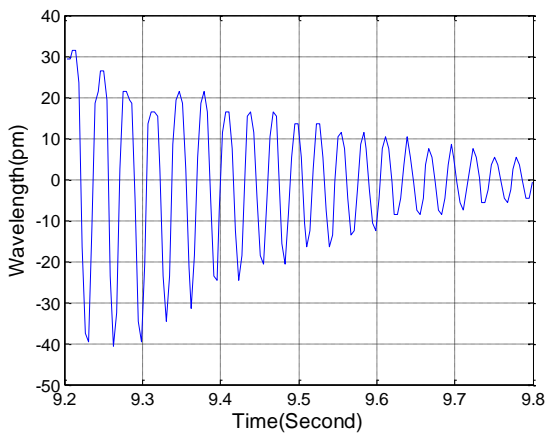


Figure 64

Strain response of test 2 at 9.2s~9.8s

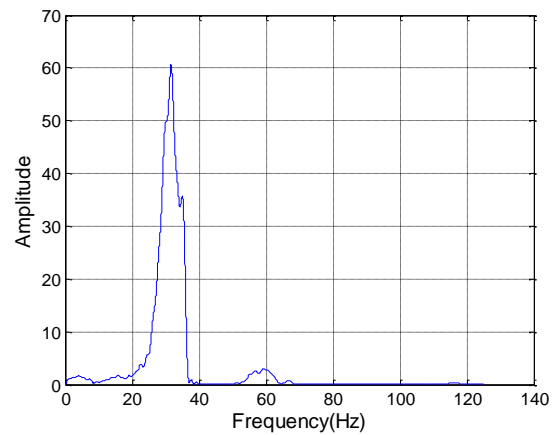


Figure 65

FFT of strain response of test 2 at 9.2s~9.8s

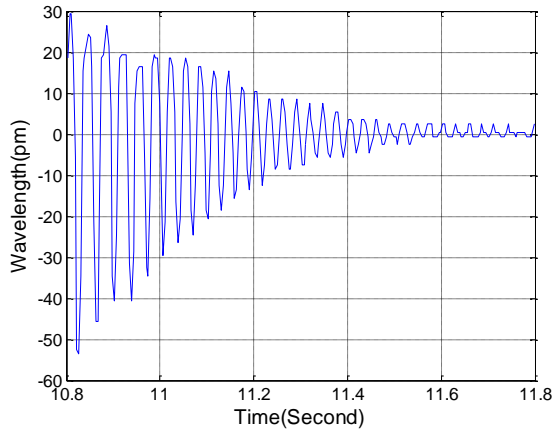


Figure 66
Strain response of test 3 at 10.8s~11.8s

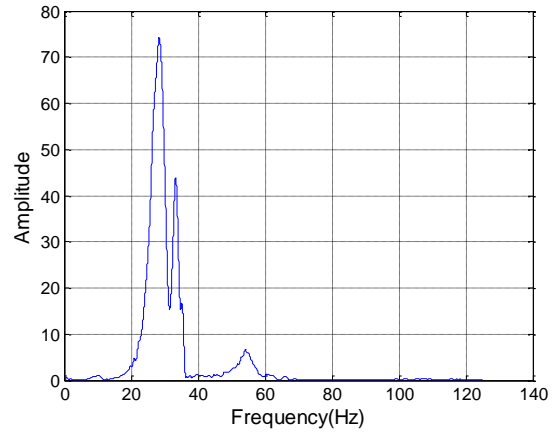


Figure 67
FFT of strain response of test 3 at 10.8s~11.8s

(2) Clicking test with sand

The specimen was fixed in the edge of a pail under the condition of empty and full of saturated sand, as shown in Figure 68. The strain response under the clicking with hammer is shown in Figure 69. It was found that the sensor buried in the saturated sand works as well as the one exposed in the air.

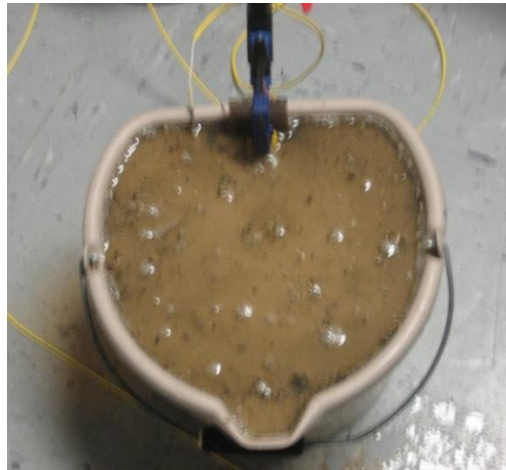


Figure 68
Clicking test of FRP specimen

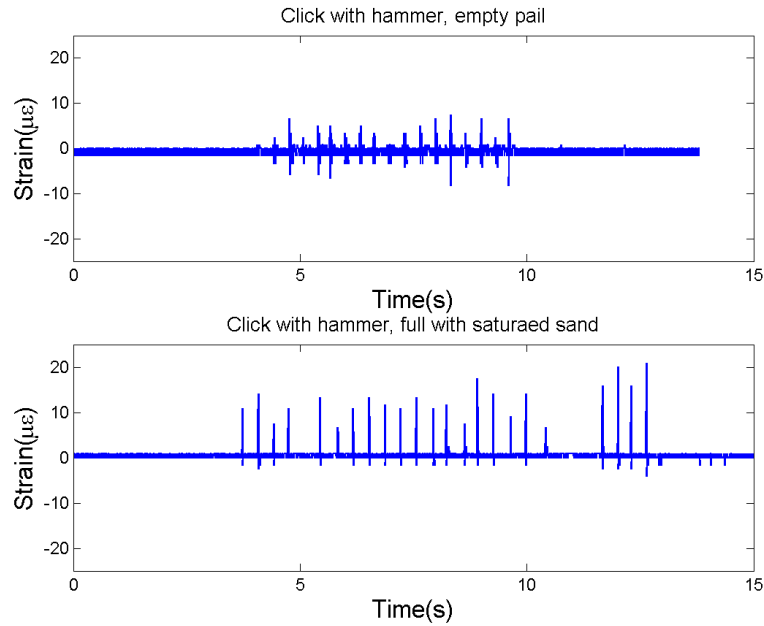


Figure 69
Comparison of the strain response clicked by the hammer

(3) Water flow test

The specimen was soaked in the water tank, and the water was pushed toward the specimen to simulate the water impact. As shown in Figure 71, a wavelength change of 160 pm was generated in the first 200 seconds, due to the temperature change after the specimen was soaked in the water. From the 400th second to the test end, the water in the container was scooped out by a small cup, leaving the water level decreasing gradually, which corresponds with the declining segments in the figure. The water was pushed toward the specimen in the tank, inducing strain responses of the specimen with amplitude of about 15pm, with more details given below.



Figure 70
Water flow test of FRP specimen

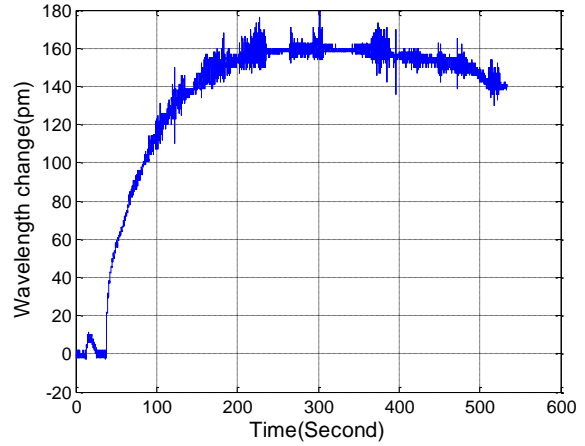


Figure 71
Strain response of water flow test

Some fractions of the strain response are picked and the frequency characteristics are obtained through an FFT technique (Figure 72~Figure 79). The water flow frequency is various, ranged in 0~5Hz.

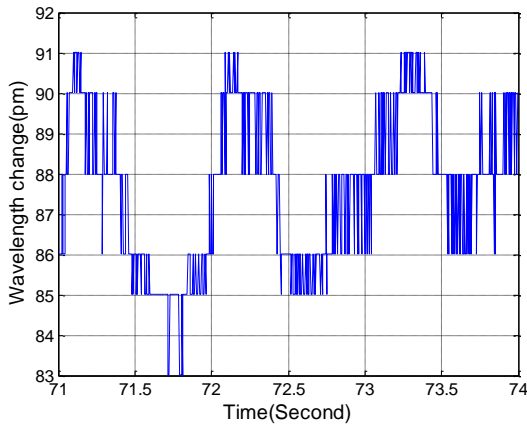


Figure 72
Strain response during 71s~74s

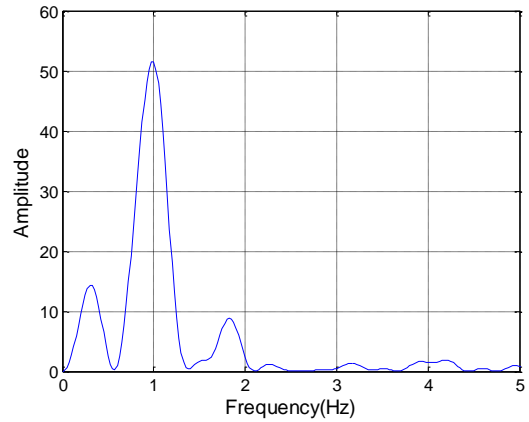


Figure 73
FFT of strain response during 71s~74s

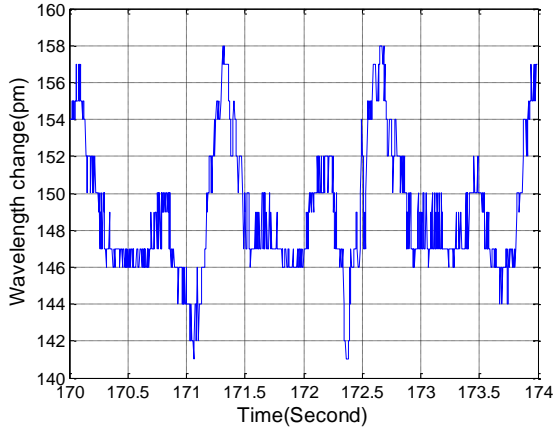


Figure 74

Strain response during 170s~174s

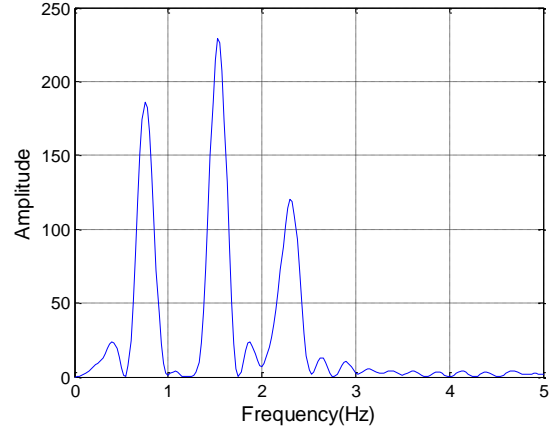


Figure 75

FFT of strain response during 170s~174s

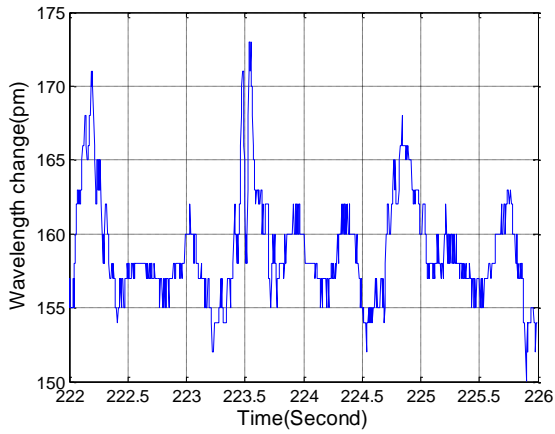


Figure 76

Strain response during 222s~226s

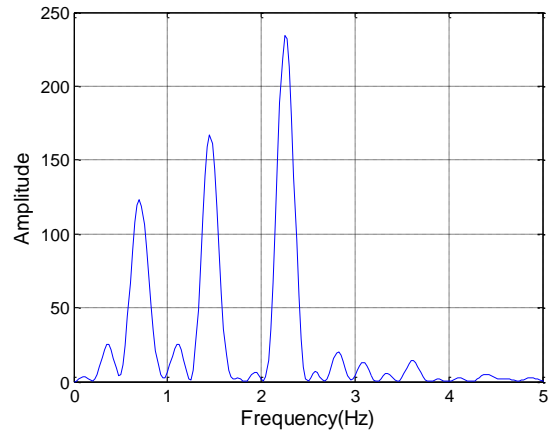


Figure 77

FFT of strain response during 222s~226s

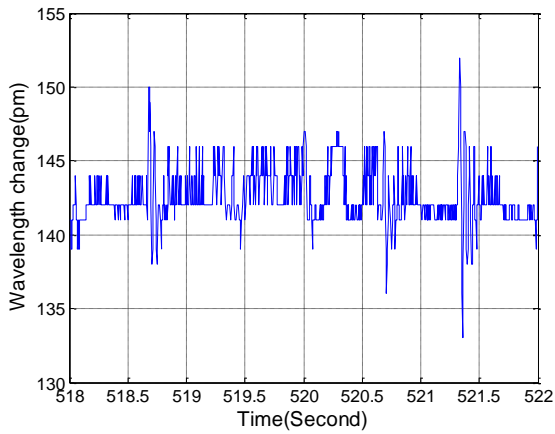


Figure 78

Strain response during 518s~522s

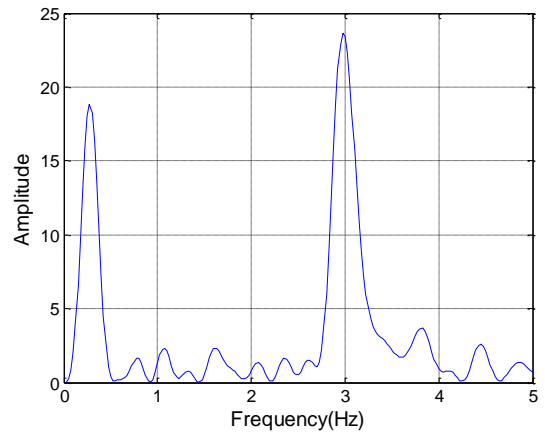


Figure 79

FFT of strain response during 518s~522s

Test of FRP Bar on Steel Tube (stand)

For the FRP bar held on the steel stand, the following tests have been conducted:

- Pressing the FRP bar in different positions to investigate the influence of each sensor,
- Bending the steel stand on the top to simulate the pier bending on the top,
- Clicking the top of the steel stand, and
- Impact testing in the water tank on the shake table, with and without the hanging weight.

(1) Pressing the rebar

Subsequently press the rebar at the position of 0.66 ft. (0.2 m), 1.97 ft. (0.6 m), and 2.95 ft. (0.9 m). The strain responses are shown in Figure 80~Figure 83. The FRP bar is designed as two fixed segments and one cantilever segment through fixing in the position of 0 ft., 1.31 ft. (0.4 m), and 2.62 ft. (0.8 m). It can be seen that when the pressing in one span, the other spans also have response, which means the FRP bar behaves as a continuous beam instead of two fixed beams. Therefore, all the sensors will response wherever the loading is.

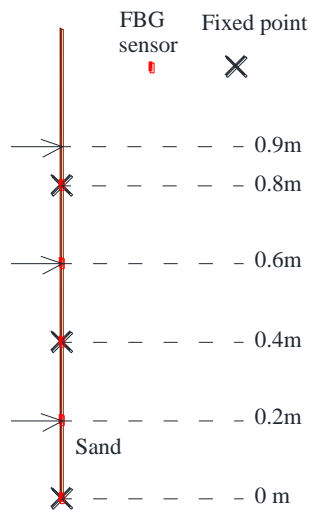


Figure 80
Schematic drawing of test

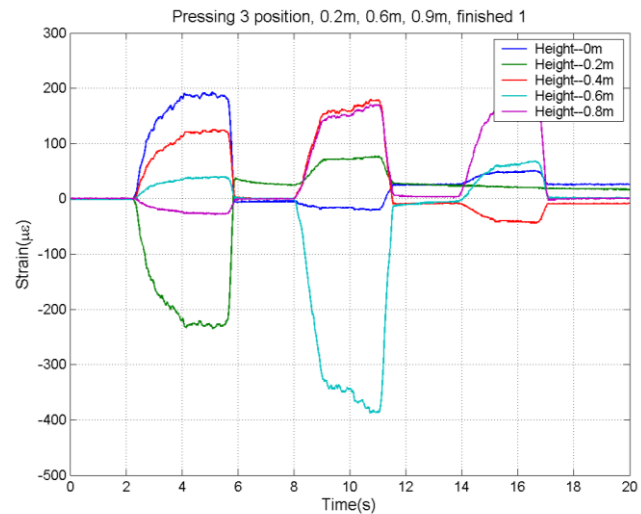


Figure 81
Strain response of test 1

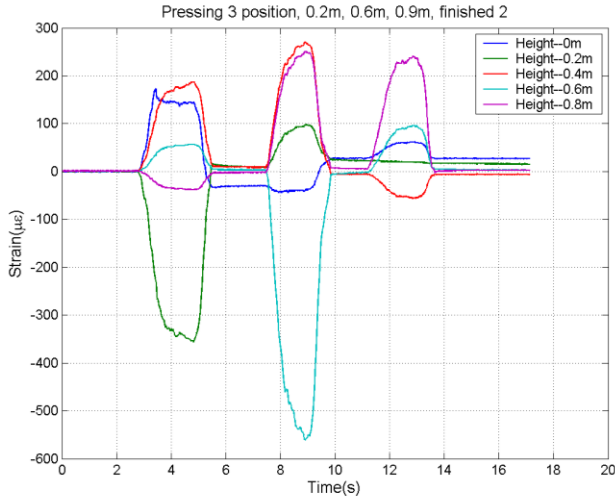


Figure 82
Strain response of test 2

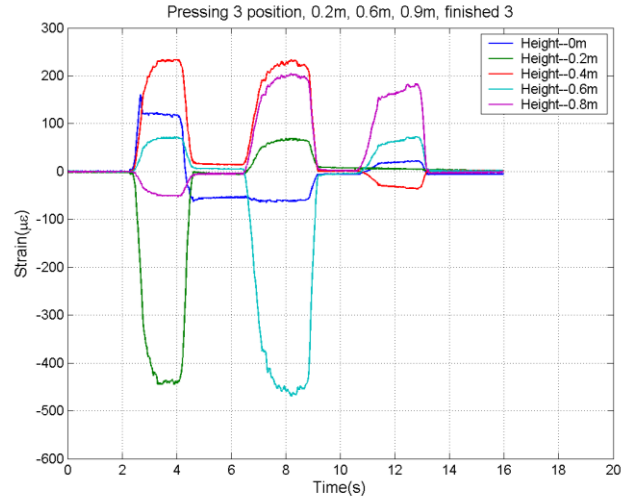


Figure 83
Strain response of test 3

(2) Bending on the top

A bending test on the top of the FRP bar was conducted before it was fixed on the steel tube, that is, only the bottom is fixed. The strain results shown in Figure 85 indicate good performance of the sensors.

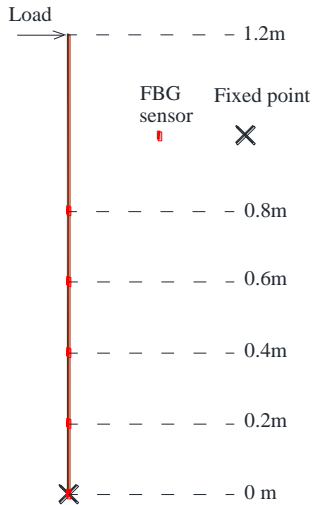


Figure 84
Bending on the top

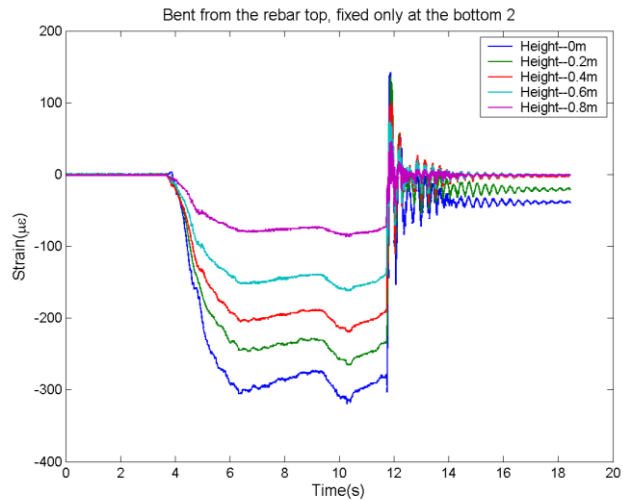


Figure 85
Strain response of bending test

After the fixation finished, a screwdriver was used to apply a bending moment on the top of the steel tube, as shown in Figure 86. From the results in Figure 87~Figure 89, it can be seen that the strain distribution along the height is different from that of a continuous beam. For a continuous beam without sand, the strain along the height should be like the dash curve in

Figure 89, namely, the maximum moment should be at the bottom instead of at the position of 0.66 ft. (0.2 m). The solid curve in Figure 89 indicates that the top part of the sand provides the resistance for moment, which leads to the maximum moment at the position of 0.66 ft. (0.2 m) and almost a zero at the bottom.

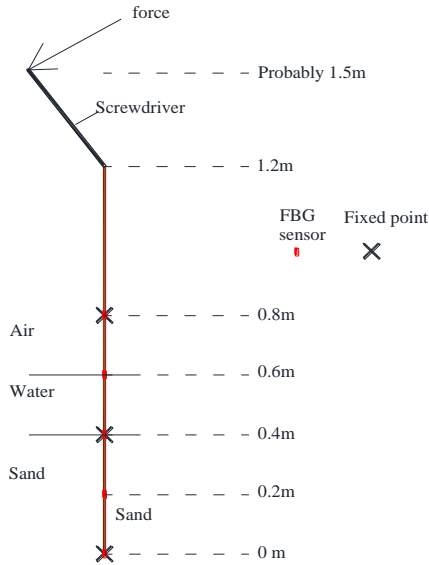


Figure 86
Bending on the top of steel tube

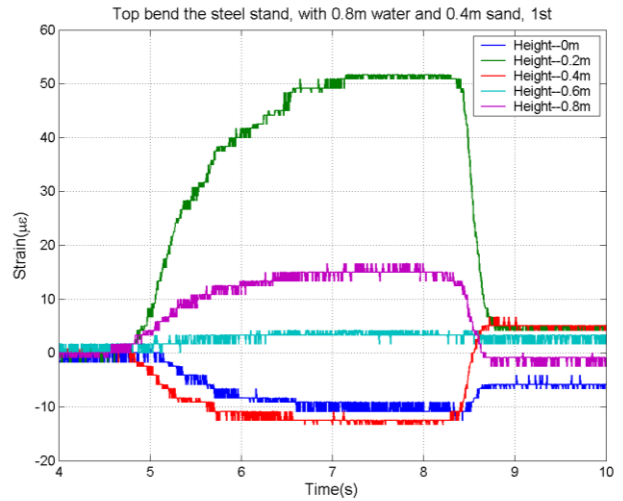


Figure 87
Strain response of test 1

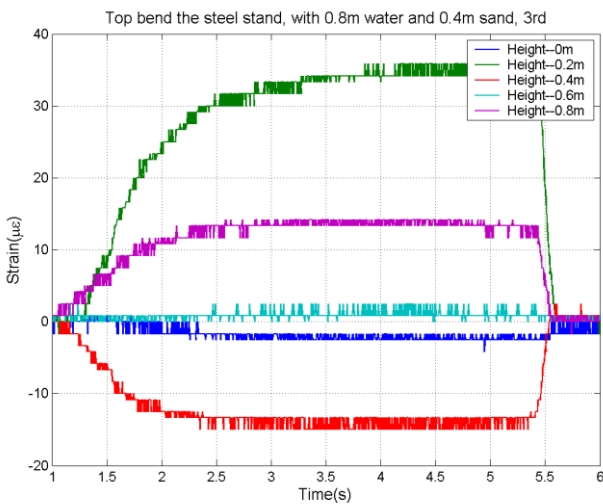


Figure 88
Strain response of test 2

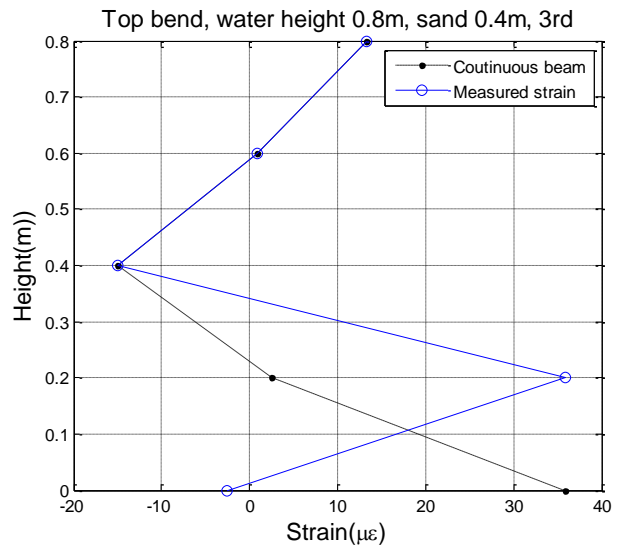


Figure 89
Strain response of test 3

(3) Clicking test

The FRP is buried in the sand with the height of 1.31 ft. (0.4 m) and submerged in the water of 1.97 ft. (0.6 m). Above 1.97 ft. (0.6 m), the bar is exposed in the air. As shown in Figure 90, the FRP rebar is clicked at position of 2.95 ft. (0.9 m). Figure 91~Figure 93 shows the strain response and the maximum amplitude of the response is about 100 $\mu\epsilon$. The sensors buried in the sand, at the position of 0 ft. and 0.66 ft. (0.2 m), have almost no response. It gives an idea that the bottom sensors with little response when clicking on the top are still in the sand, and can be used to locate the water and sand interface in the certain range.

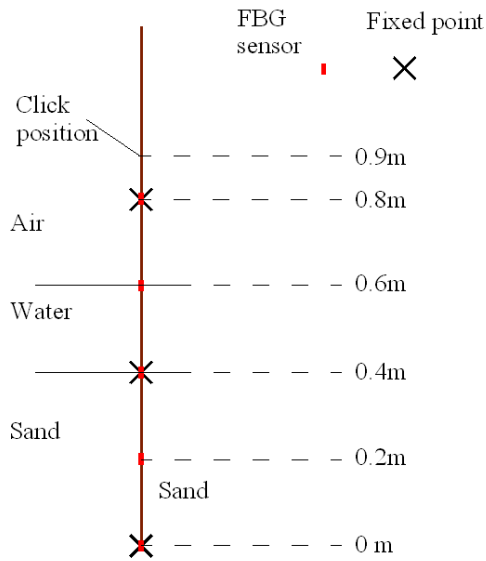


Figure 90
FRP bar clicked at 2.95 ft position

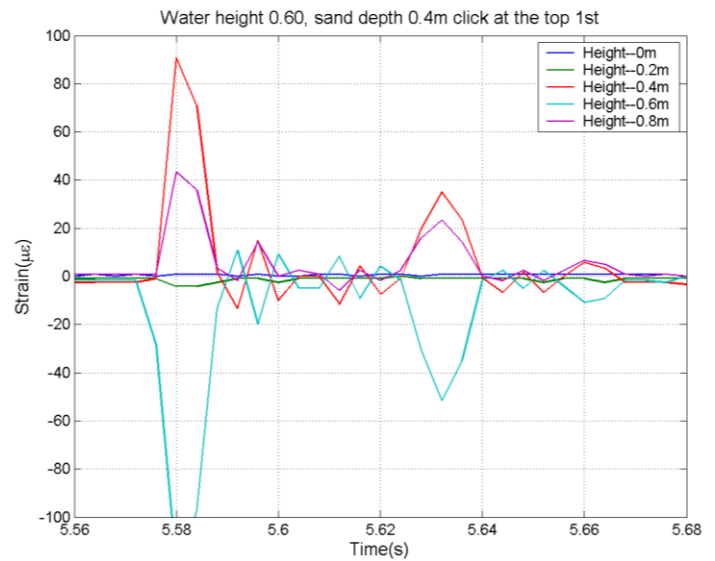


Figure 91
Zoomed strain response under clicking, 1st run

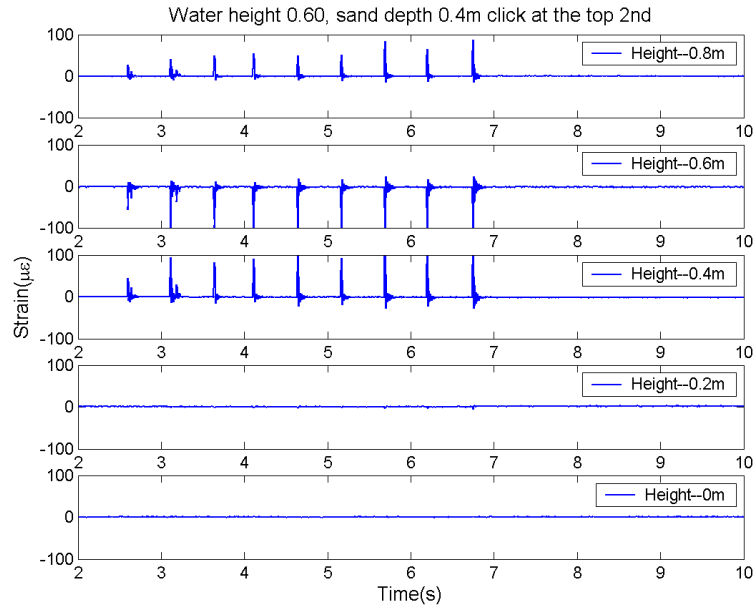


Figure 92
Strain response under clicking, 2nd run

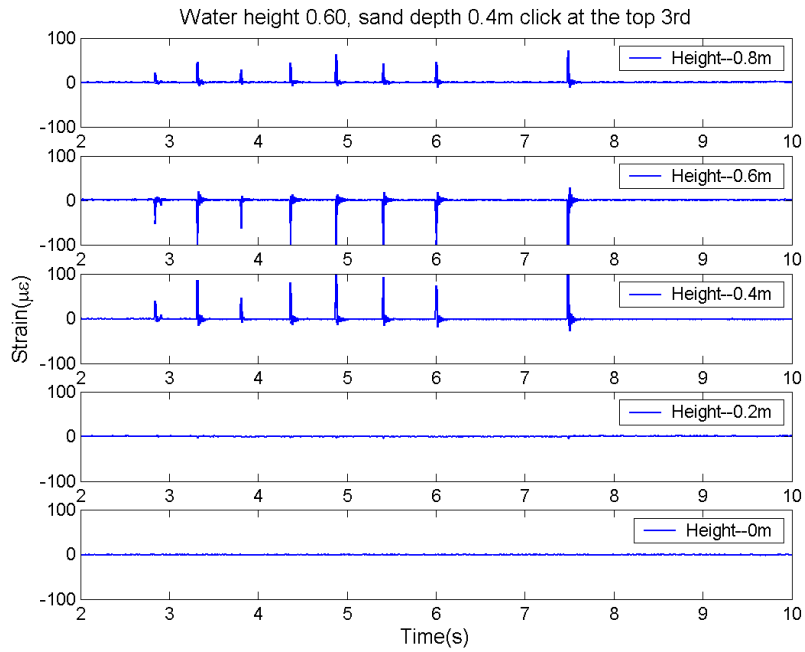


Figure 93
Strain response under clicking, 3rd run

(4) Shaking table test

The specimen was placed in the water tank on the shaking table to test under different heights of soil and water, as shown in Figure 94.

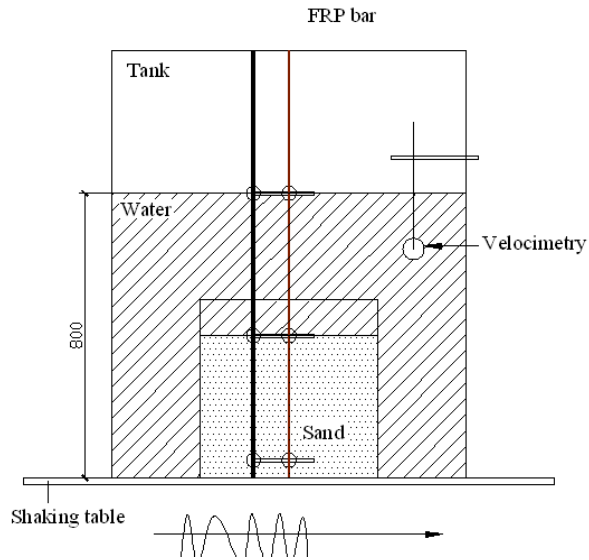


Figure 94
Layout of the specimen

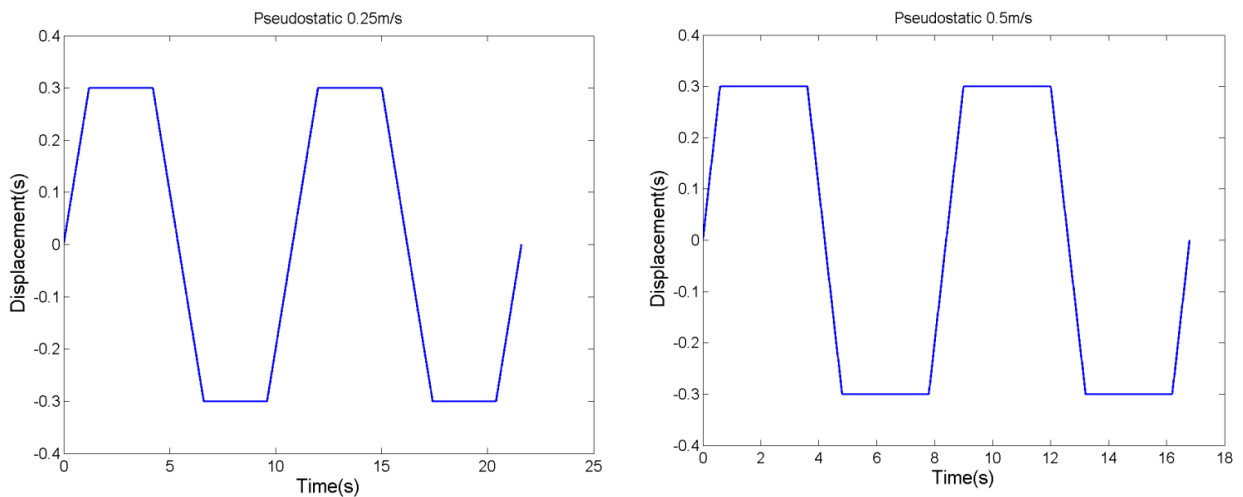


Figure 95
Loading procedure of 0.82 ft/s and 1.64 ft/s

In order to investigate the water effect, the height of the water is set as 0.66 ft. (0.2 m), 1.31 ft. (0.4 m), 1.97 ft. (0.6 m), and 2.62 ft. (0.8 m), respectively. Each height has the speed of 0.82 ft/s (0.25 m/s) and 1.64 ft/s (0.5 m/s) for the shaking table, as shown in Figure 95. For the height of 0.66 ft. (0.2 m), 1.31 ft. (0.4 m), and 1.97 ft. (0.6 m), three runs were conducted; for the height of 2.62 ft. (0.8 m), two runs were conducted, but this report only lists the results of one run.

Water at a height of 0.66 ft (0.2 m): Figure 96~Figure 99 shows the strain response when the water height is 0.66 ft. At the speed of 1.64 ft/s (0.5 m/s), the sensor at the position of 0.66 ft is significant compared to other positions. The maximum strain is about $40 \mu\epsilon$.

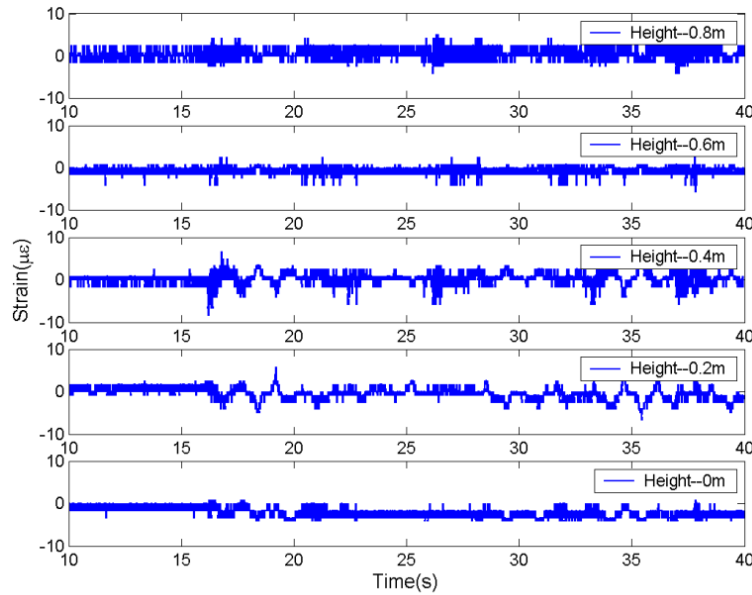


Figure 96
Strain response, water 0.66 ft, 0.82 ft/s

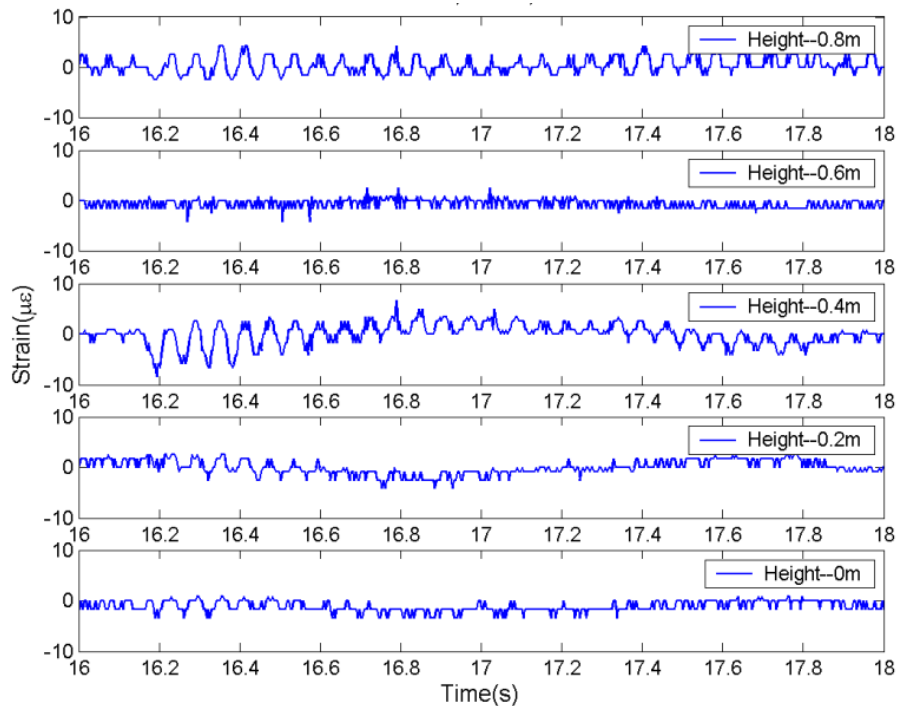


Figure 97
Zoomed strain response, water 0.66 ft, 0.82 ft/s

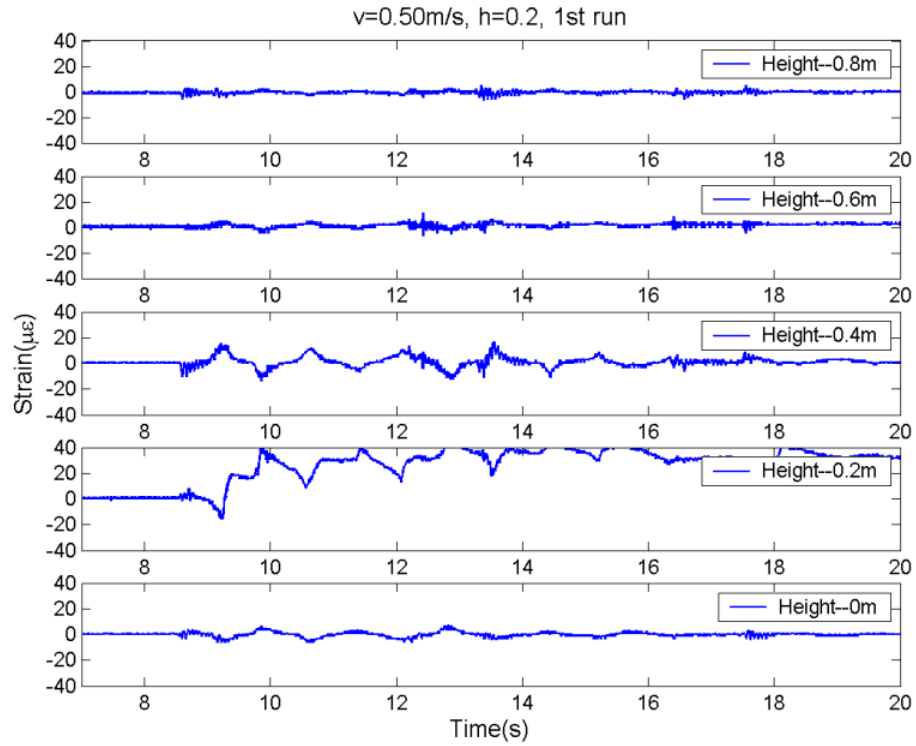


Figure 98
Strain response, water 0.66 ft, 1.64 ft/s

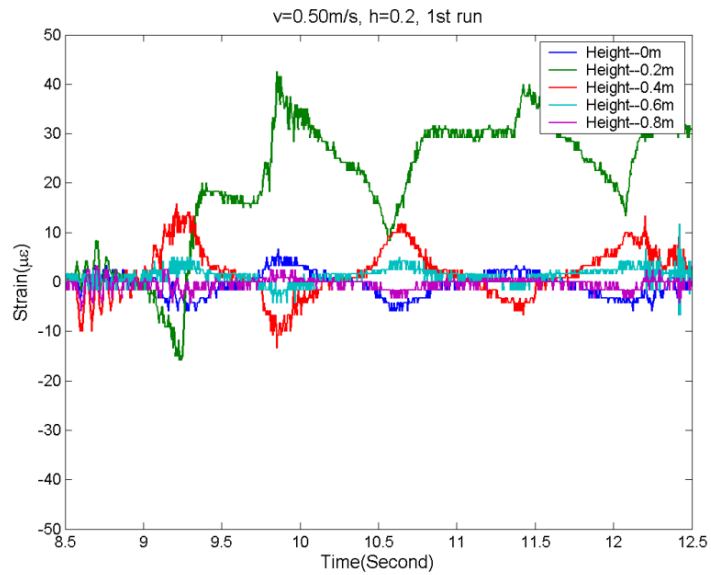


Figure 99
Zoomed strain response, water 0.66 ft, 1.64 ft/s

Water at a height of 1.31 ft (0.4 m): Figure 100~Figure 103 shows the strain response when the water height is 1.31 ft. (0.4 m). At the speeds of 0.82 ft/s (0.25 m/s) and 1.64 ft/s (0.5 m/s), the sensors at the position of 0.66 ft. (0.2 m) and 1.31 ft. (0.4 m), are significant compared to other positions. The maximum strain is about $30 \mu\epsilon$.

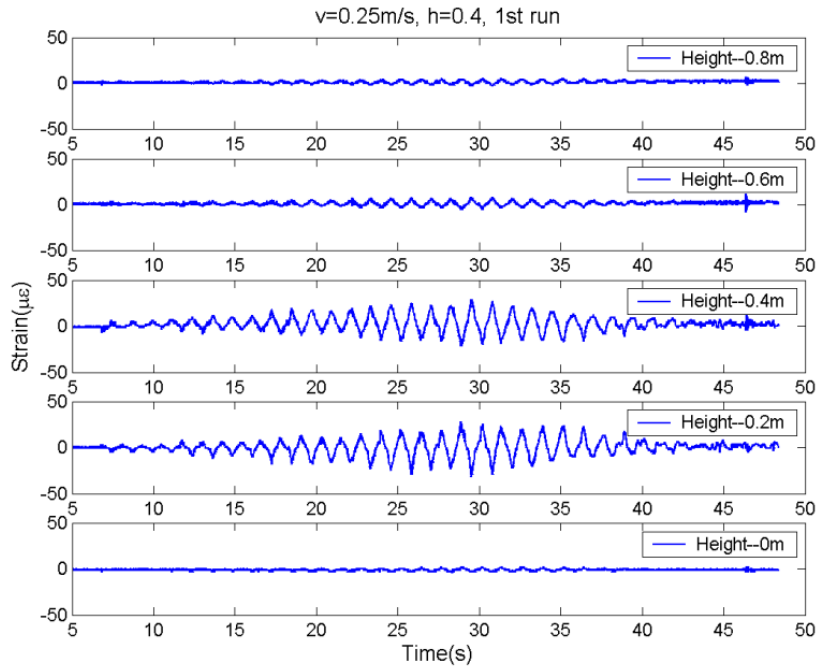


Figure 100
Strain response, water 1.31 ft, 0.82 ft/s

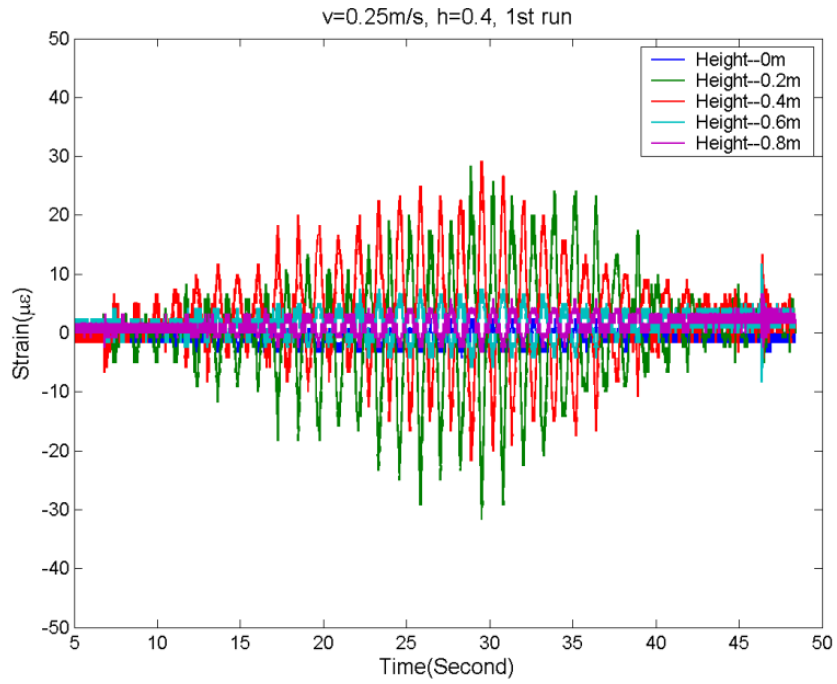


Figure 101
Zoomed strain response, water 1.31 ft, 0.82 ft/s

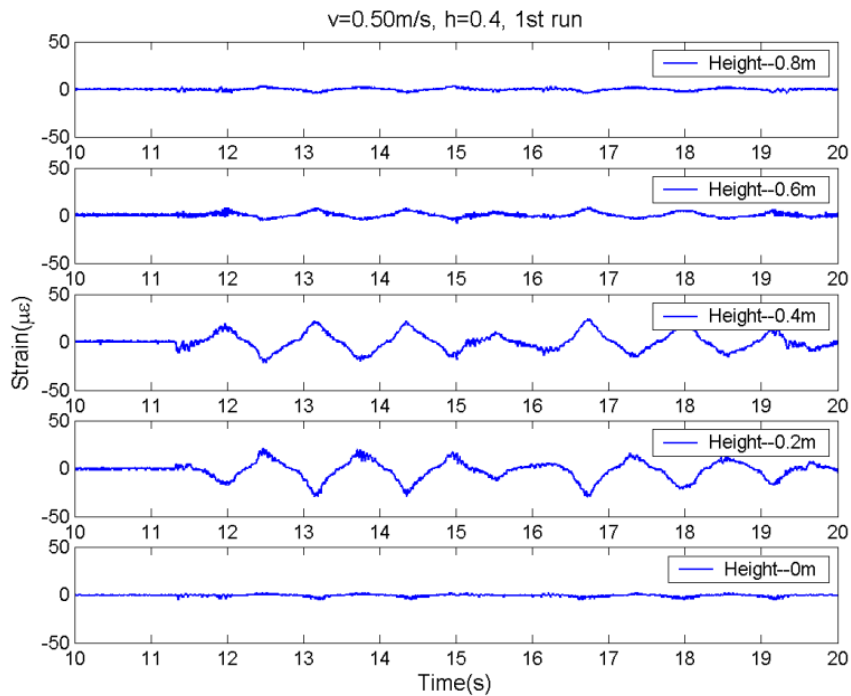


Figure 102
Strain response, water 1.31 ft, 1.64 ft/s

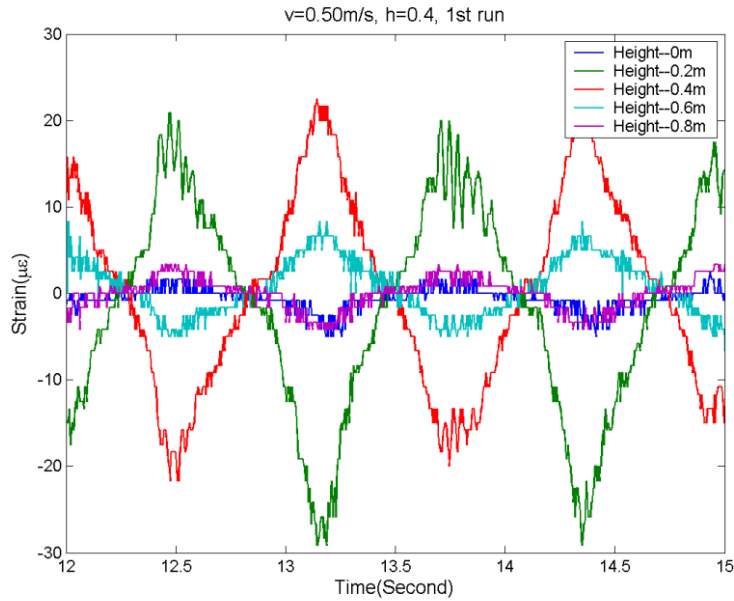


Figure 103
Zoomed strain response, water 1.31 ft, 1.64 ft/s

Water at a height of 1.97 ft. (0.6 m): Figure 104~Figure 107 shows the strain response when the water height is 1.97 ft. (0.6 m). At the speed of 0.82 ft/s (0.25 m/s), the difference of responses at each position is not very obvious. At the speed of 1.64 ft/s (0.5 m/s), the sensors at the position of 1.31 ft. (0.4 m) and 1.97 ft. (0.6 m) become significant compared to other positions. The maximum strain is about 20 $\mu\epsilon$.

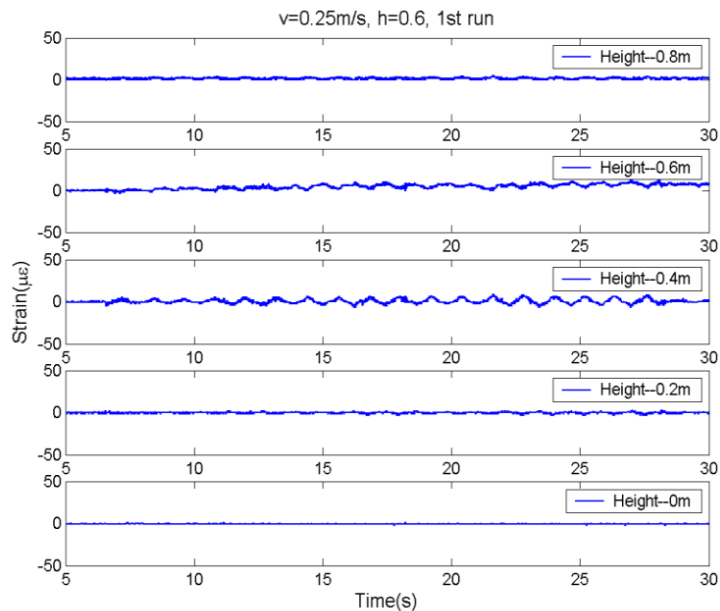


Figure 104
Strain response, water 1.97 ft, 0.82 ft/s

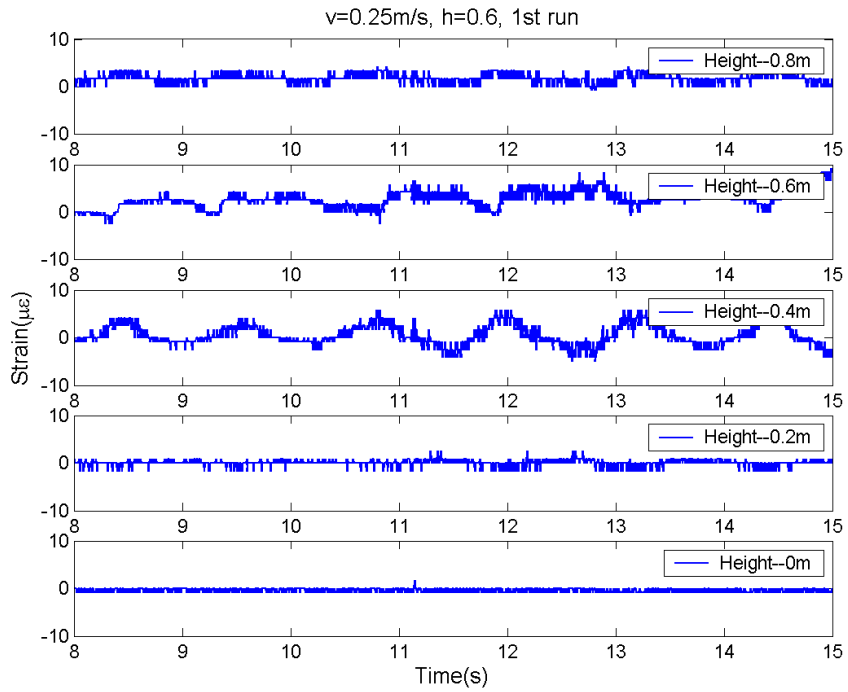


Figure 105
Zoomed strain response, water 1.97 ft, 0.82 ft/s

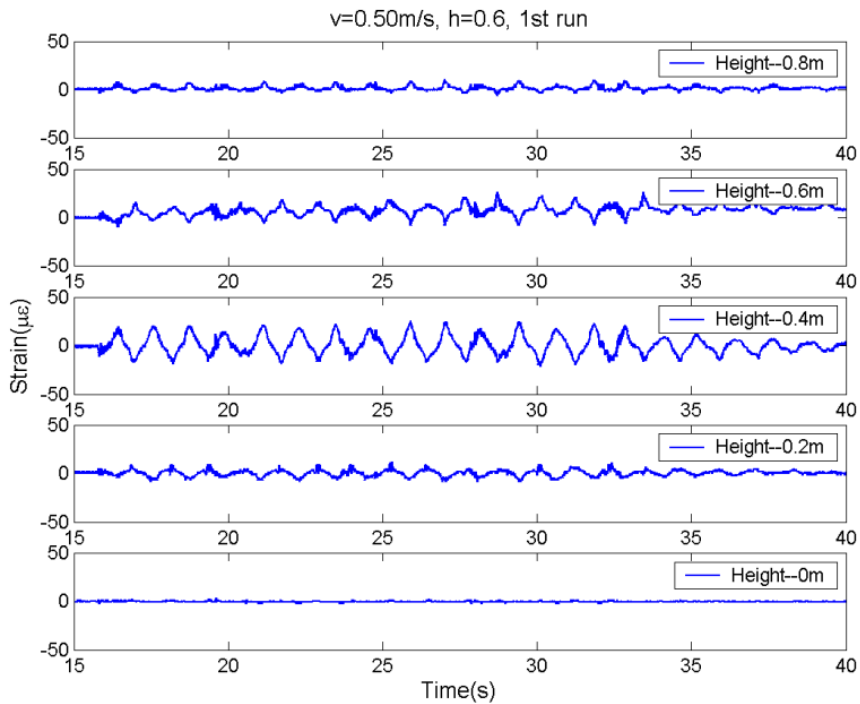


Figure 106
Strain response, water 1.97 ft, 1.64 ft/s

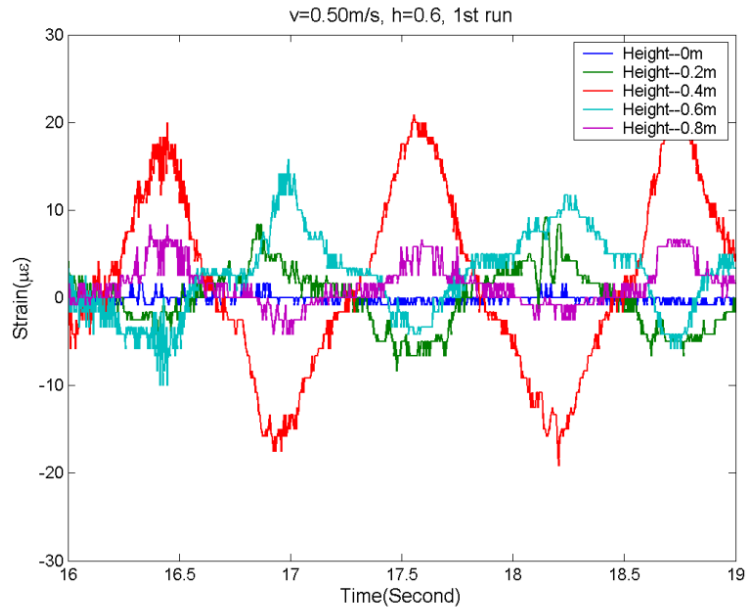


Figure 107
Zoomed strain response, water 1.97 ft, 1.64 ft/s

Water at a height of 2.62 ft (0.8 m): Figure 108~Figure 111 shows the strain response when the water height is 2.62 ft. (0.8 m). The frequency of the water is about 1.2 Hz. At the speed of 1.64 ft/s, the sensors at the position of 1.31 ft. (0.4 m), 1.97 ft. (0.6 m), and 2.62 ft. (0.8 m) are significant compared to other positions. The maximum strain is about 20 $\mu\epsilon$. At the position of 0.66 ft. (0.2 m) and 0.0 ft. there is barely any strain response, which means that the shaking table barely propels the bottom water in the tank.

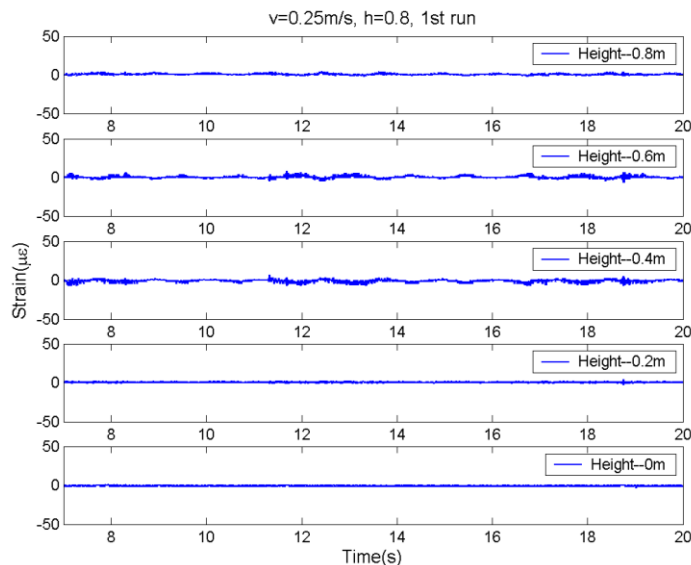


Figure 108
Strain response, water 2.62 ft, 0.82 ft/s

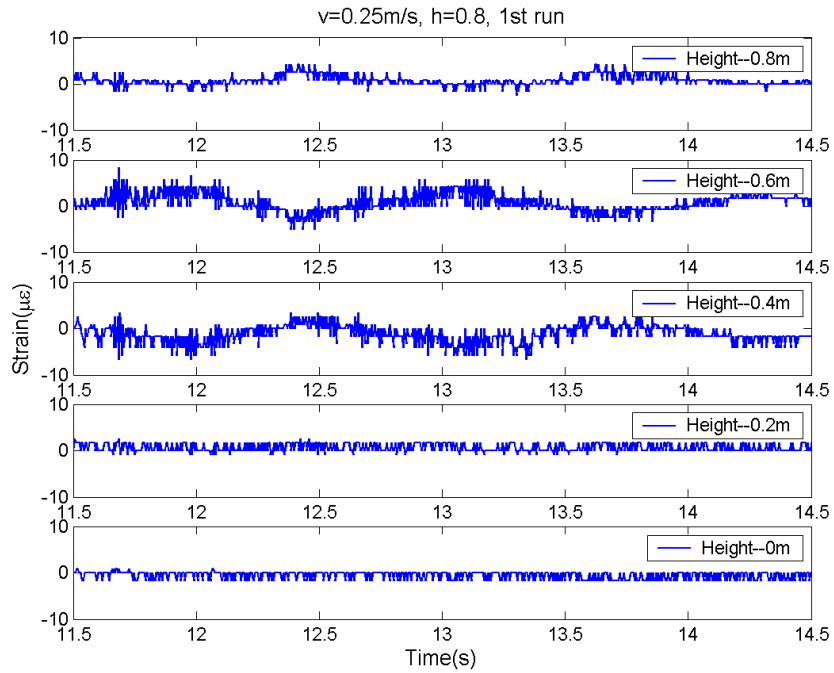


Figure 109
Zoomed strain response, water 2.62 ft, 0.82 ft/s

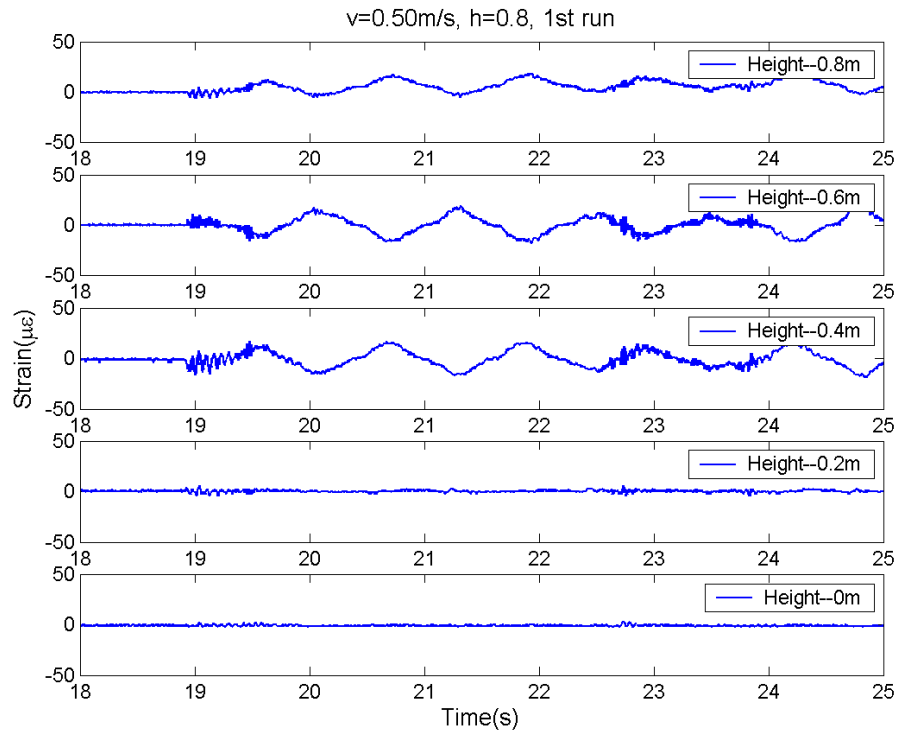


Figure 110
Strain response, water 2.62 ft, 1.64 ft/s

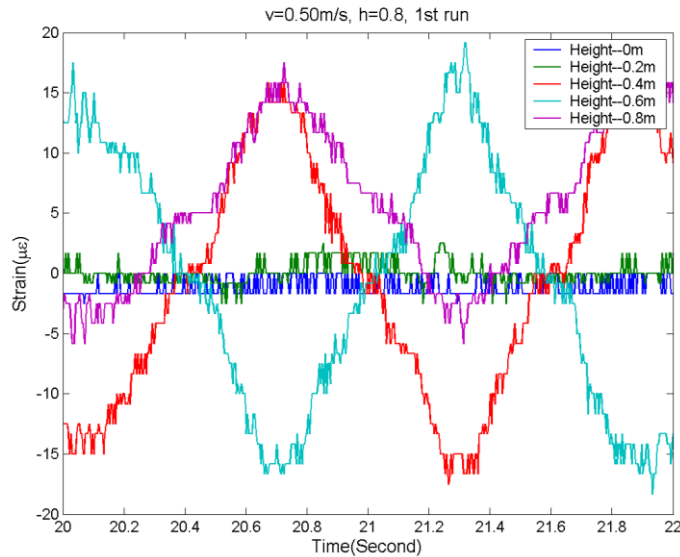


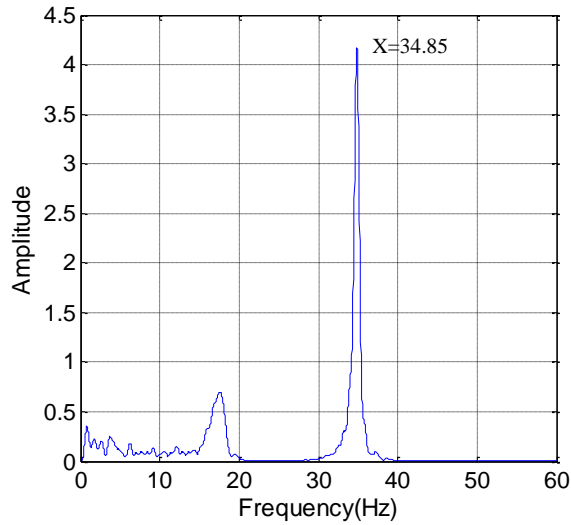
Figure 111
Zoomed strain response, water 2.62 ft, 1.64 ft/s

From the above test with different water heights, the higher the water, the less significant the sensors respond, especially for the bottom sensors. It indicates that the sensor in the deep water with slow water velocity will have little response to the water flow impact, which might lead to the wrong interface of water and sand. Therefore, basing results on the water impact only is not enough to obtain the correct answer.

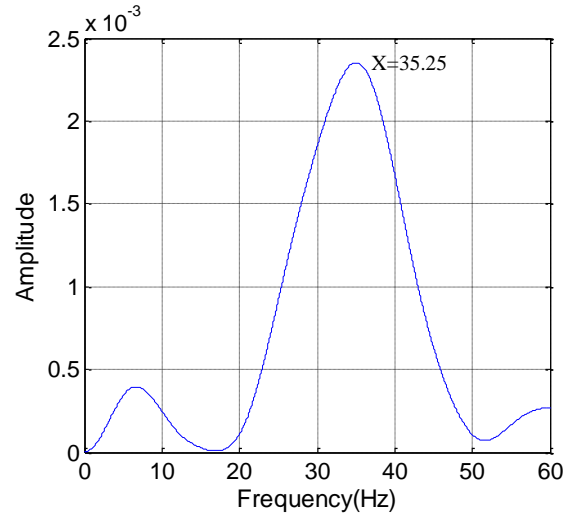
Test of FRP bar on GFRP pipe

(1) Detection of frequency change

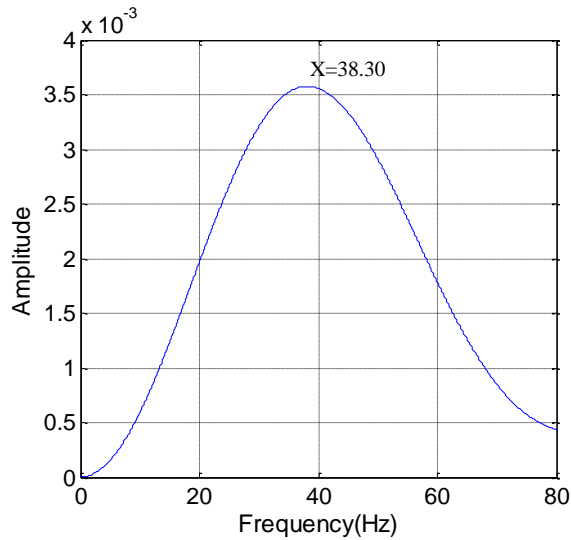
The GFRP pipe was first put on the ground without sand and clicked on the top, and was then buried in the sand at heights of 0.66 ft. (0.2 m), 1.31 ft. (0.4 m), and 1.97 ft. (0.6 m). The time histories of strain response are transferred into the frequency domain using Fast Fourier Transform (FFT), as shown in Figure 112. The first frequencies of the four cases are 34.85 Hz, 35.25 Hz, 38.30 Hz, and 42.00 Hz, respectively. Therefore, it confirms that the fundamental frequency of the structure decreases as the reduction of sand height, which indicates a scour activity.



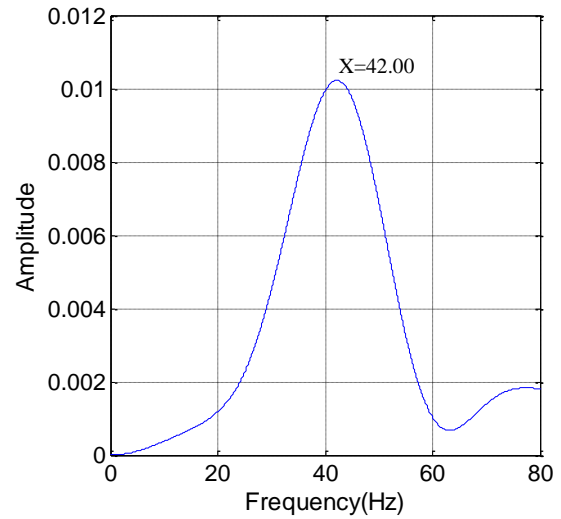
(a) without sand



(b) with 0.2m sand



(c) with 0.4 sand



(d) with 0.6m sand

Figure 112
FFT of strain response

(2) Detection of moment/strain profile change

As observed earlier in the numerical simulation, the location of the maximum moment in the pile changes with the scour depth. In this section, tests of the GFRP pipe under different supporting conditions were conducted: without sand and with different heights of sand. A lateral force was applied intermittently on the top of the GFRP pipe to generate the bending moment in the pipe, and the time history of the strain response at different locations was recorded by the five sensors.

Without sand: The GFRP pipe was on the ground without any sand around and six runs were conducted. The strain responses of the five sensors of the first run are shown in Figure 113. For each run, the strain value of the five sensors at a specific time was extracted to demonstrate the strain distribution along the pipe length. Figure 114 is the strain value along the pile length at the five peak times shown in Figure 113. Those values are then normalized based on the ratio to the strain of the bottom sensor, namely, the strain value of the sensor at the position of 0.0 ft. is set to be 1, as shown in Figure 115. The average of the normalized strain value at each run is then summarized in Figure 116. It can be found that the strain distribution is nearly linear.

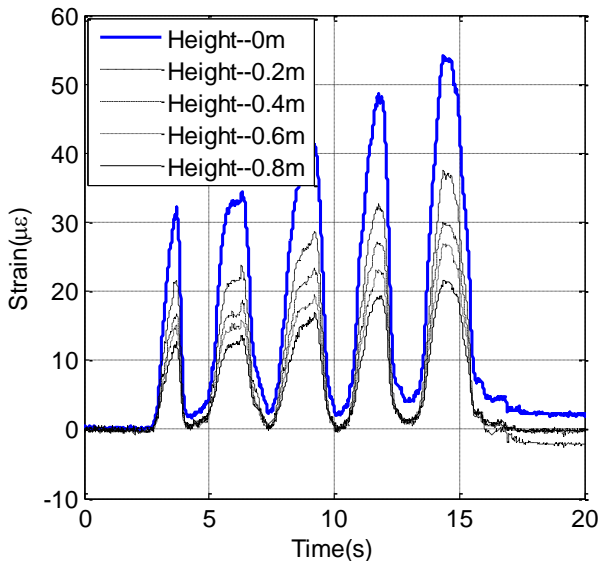


Figure 113
Strain response of the pipe without sand

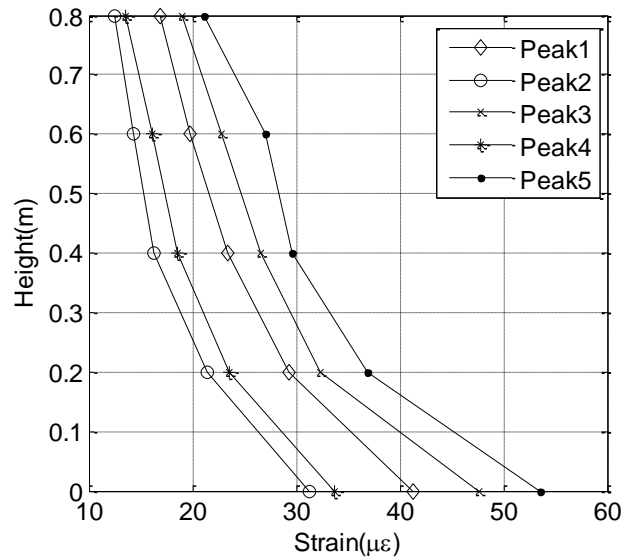


Figure 114
Strain distribution of first run

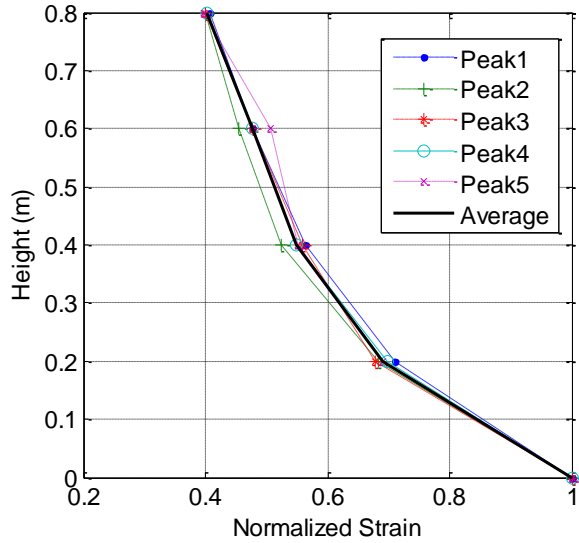


Figure 115
Normalized strain distribution of first run

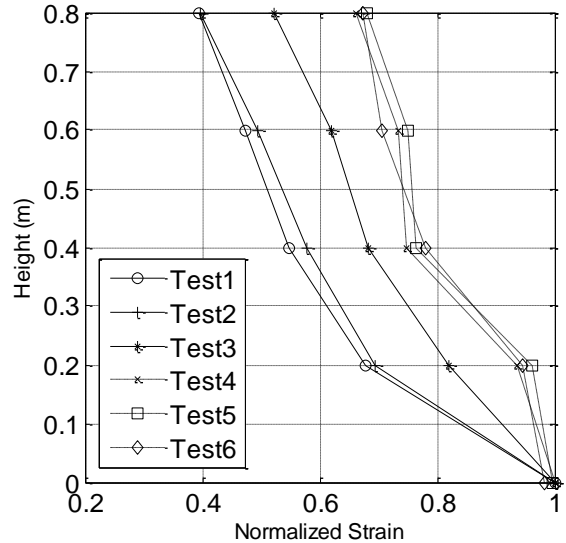


Figure 116
Normalized strain distribution of 6 runs

With sand 0.66 ft (0.2 m) high and 1.31 ft (0.4 m) high: The GFRP pipe was buried in the sand with a height of 0.66 ft. (0.2 m) and 1.31 ft. (0.4 m), respectively. With the same procedure, the normalized strain distributions of all three runs are summarized in Figure 117 and Figure 118. The maximum strain in Figure 117 is at the position of 0.66 ft. (0.2 m) and that in Figure 118 is at the position of 1.31 ft. (0.4 m), which is equal to the sand height of each case and indicates the scour depth.

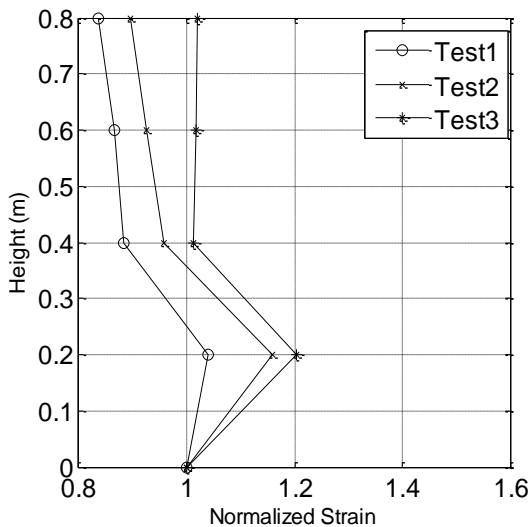


Figure 117
Normalized strain distribution of pipe with 0.66 ft. sand

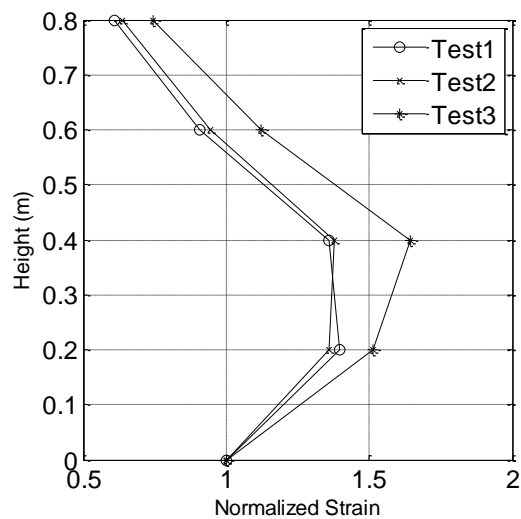


Figure 118
Normalized strain distribution of pipe with 1.31 ft. sand

(3) Water current test on the shaking table

In this test, the specimen was put into the water tank on the shaking table to simulate the water flow action, and hanging weights were used to simulate the debris in the river water. The GFRP pipe with the FRP bar was buried in different heights of sand. In the first case, the sand height was 1.31 ft. (0.4 m) and one hanging weight was at the position of 1.97 ft. (0.6 m). In the second case, the sand height was 0.66 ft. (0.2 m) and two hanging weights were arranged at the position of 0.66 ft. (0.2 m) and 1.97 ft. (0.6 m), respectively. The water height was 2.62 ft. (0.8 m) and the speed of the shaking table was set to be 0.33 ft/s (0.1 m/s), 0.82 ft/s (0.25 m/s), and 1.64 ft/s (0.5 m/s).

The time histories of strains at the speed of 1.64 ft/s (0.5 m/s) are shown in Figure 119 and Figure 120. Figure 119 is the strain response from sensors on the FRP bar and Figure 120 is that from sensors attached on the GFRP pipe. It is observed that the response of the FRP bar is much stronger than that of the GFRP pipe, especially at the position of 1.97 ft. (0.6 m), where the hanging weight is located. Besides, the curves of both cases look totally different. The one in Figure 119 for height 1.97 ft. (0.6 m), looks like an impulse signal and is very obviously distinguished from others, due to the discontinuous impact of the hanging weight.

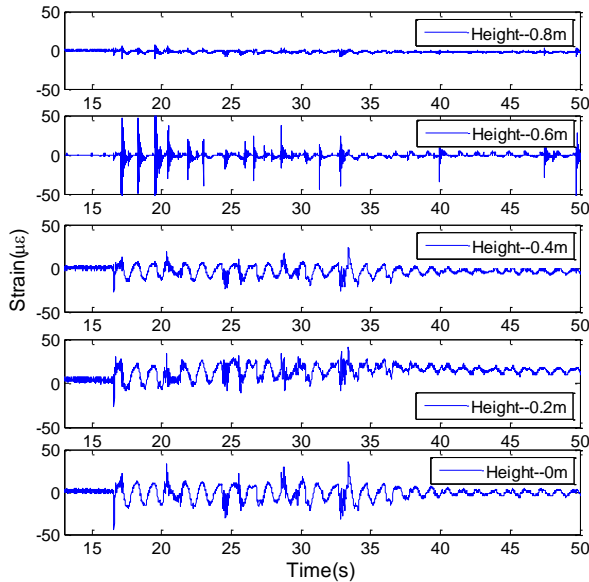


Figure 119
Strain of FRP bar with 1.31 ft. sand

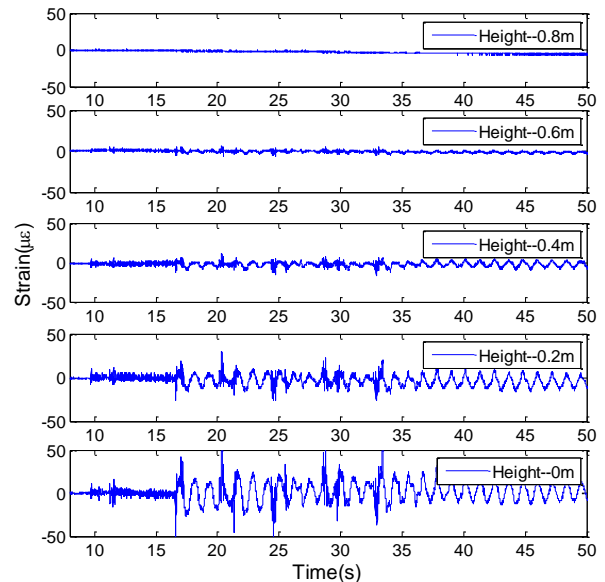


Figure 120
Strain of GFRP pipe with 1.31 ft. sand

The same observation can be seen from the results of the second case with 0.66 ft. (0.2 m), sand as shown in Figure 121 and Figure 122. Besides the position of 1.97 ft. (0.6 m), Figure 121 reveals that the impulse-like signal appears at the position of 0.66 ft. (0.2 m), as well. From case 1 to case 2, the sand height reduces from 1.31 ft. (0.4 m) to 0.66 ft. (0.2 m),,

which exposes the sensor and the hanging weight at the position of 0.66 ft. (0.2 m),. It indicates that as the soil is scoured, the sensor used to be buried in the soil is exposed to the water, and begins to respond recognizably differently due to the water current and debris impact. It is a good sign for scour detection.

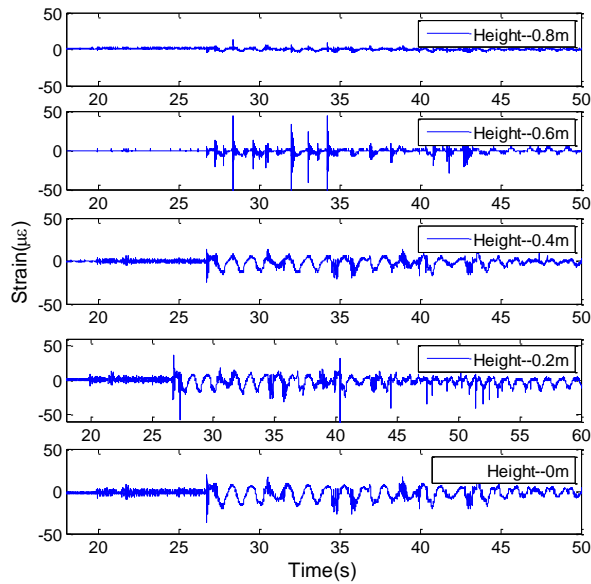


Figure 121
Strain of FRP bar with 0.66 ft sand

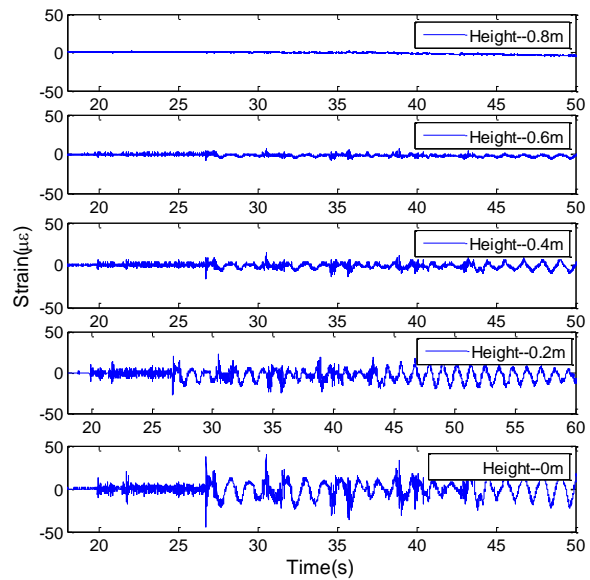


Figure 122
Strain of GFRP pipe with 0.66 ft sand

With the same procedure as described above, the strain distribution of the pipe at a given time was obtained by extracting from the time-history results of the five sensors, as shown in Figure 123, with a sand height of 1.31 ft. (0.4 m) and water speed of 0.82 ft/s. The maximum strain is at the position of 0.66 ft. (0.2 m), which is lower than the sand height. The possible reason could be that the elastic coefficient of sand is not constant but linearly distributed along the depth, which means that the stiffness at the top of the sand is very small. Moreover, the sand saturated in water weakens its supporting ability and the water flow drags the top sand and makes it loose. Therefore, the identified scour depth is not exactly the same as the actual scour depth.

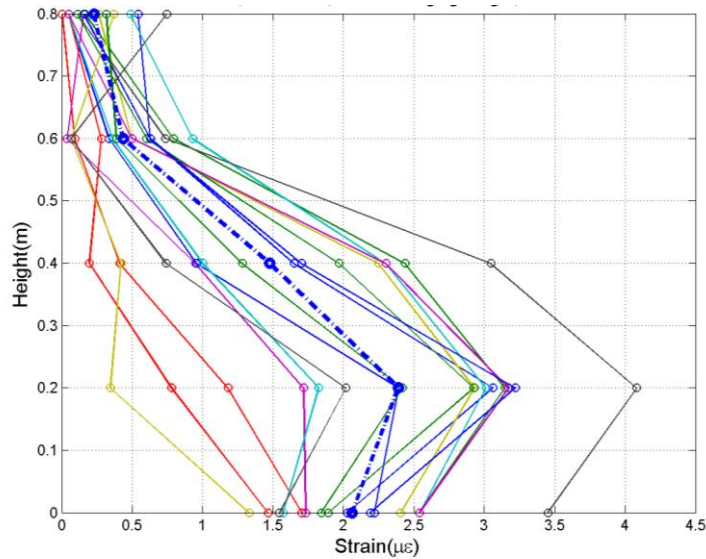


Figure 123
Strain distribution with 1.31 ft sand, $v=0.82$ ft/s

Results of Instrumental Design

As for the laboratory sample tested in the flume, there are three runs with different flowing water velocities and different discharge processes. In all cases, the temperature influence to FBG sensors is ignored.

Experimental Results for Case 1

In this case, the flowing water velocity is around 2.13 ft/s (0.65 m/s), the half limit discharge velocity of this flume. From the experimental results of case 1 (Figure 124), the local scour depth can be observed directly from the different responses of FBG sensors. Since sensor 1 has been exposed to water flow, it picks up information due to flow water pressure and impact and the measurement is relatively constant. While the running water erodes the sands and gravels, as presented in Figure 124, sensor 2 finally emerges from the riverbed at the time of 60s and the corresponding wavelength shift increases very quickly thereafter. Until sensor 2 emerges at the time of 65s, its wavelength shift becomes relatively stable again, but clearly greater than before. Among these FBG sensors, sensor 2 shows the largest wavelength shift, representing the largest bending moment in the steel bar, since only sensor 2 emerges from the riverbed surface. Accordingly, it can be seen that scour has already developed to the location of sensor 2. Since only the half limit discharge velocity of this flume is applied in this case, sensor 3 does not emerge from the riverbed surface and it only takes readings due to temperature variations and noises. During the experiment, sin-wave-like noises are also detected and possibly induced by the vibration of the cantilevered steel

bar. This vibration may be correlated with the motions of sands, gravels (transported particles), and flowing water (fluid turbulence), especially at the emerging stage of the sensor. It can be concluded that by identifying the emerging sensor locations, the specific scour depth can be successfully monitored.

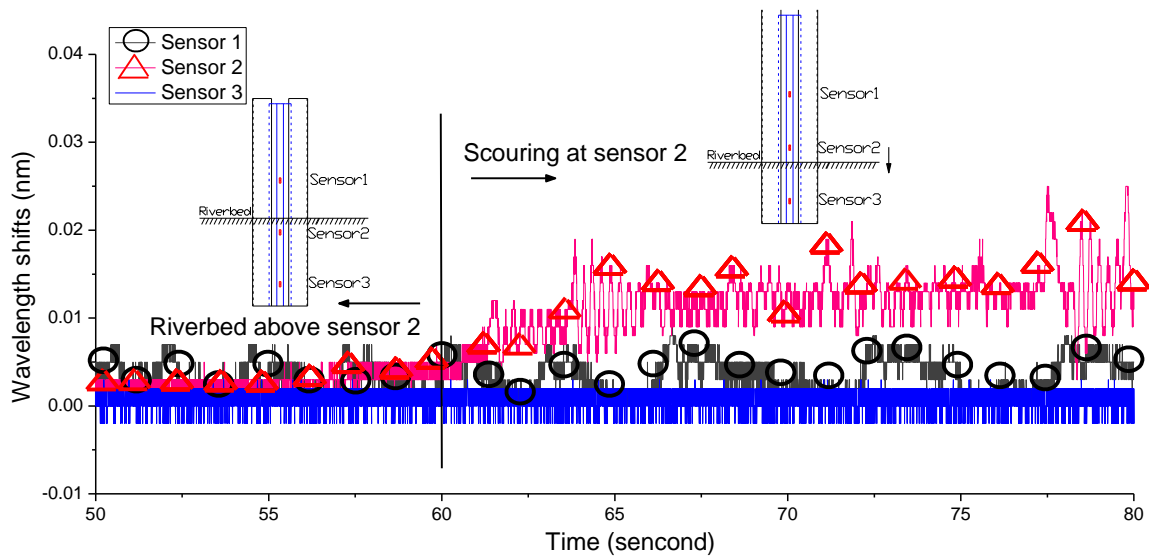


Figure 124
Experimental results of case 1

Experimental Results for Case 2

Considering different flowing water velocities, a full discharge velocity of the flume is applied, which is around 4.27 ft/s (1.3 m/s). From the experimental results of case 2 (Figure 125), the process of increase of local scour depth can be observed from an in-sequence response of more than one FBG sensors. As the case 2 experiment starts, the given constant discharge is released at the upstream end of the flume. When the running water arrives and makes contact with the cantilevered steel bar, sensor 1 responds first, as shown in Figure 125. When sensor 2 starts to emerge from the riverbed at the time of 20s, it is obvious that the reading of the wavelength shift changes significantly until it totally emerges. After a time of 30s, the reading of sensor 2 is approximately constant because the water level already remains constant. The variation of the reading may be attributed to the presence of particle motion the of sands and gravels and fluid turbulence induced by the flow velocity field. At this time, almost no reading is obtained from sensor 3 because it is still buried in the soil under the riverbed.

With sands and gravels washed away (in this case, the flowing water velocity is much higher than in case 1), as illustrated in Figure 125, sensor 3 begins to emerge by the running water in the scouring process at a time of 40s, 20s later than the sensor 2 emerging. Due to sensor 3's

location at the bottom of the tube, the corresponding bending of the steel bar caused by running water should be larger than the other positions. Accordingly, the response of sensor 3 is obviously much greater than the other sensors. Then, during a very short period (about 10s), the highest wavelength shift of sensor 3 is reached and later on keeps constant after a time of 50s. This shows the scour has already developed to the bottom position of the tube, which also successfully reveals the scour depth from the sensor 3 reading. Thereafter, the readings from all the sensors remain constant, with some sin-wave-like noises, until the end of experiment. It can be concluded that by the proposed instrumentation design the scour development can be successfully monitored in real time.

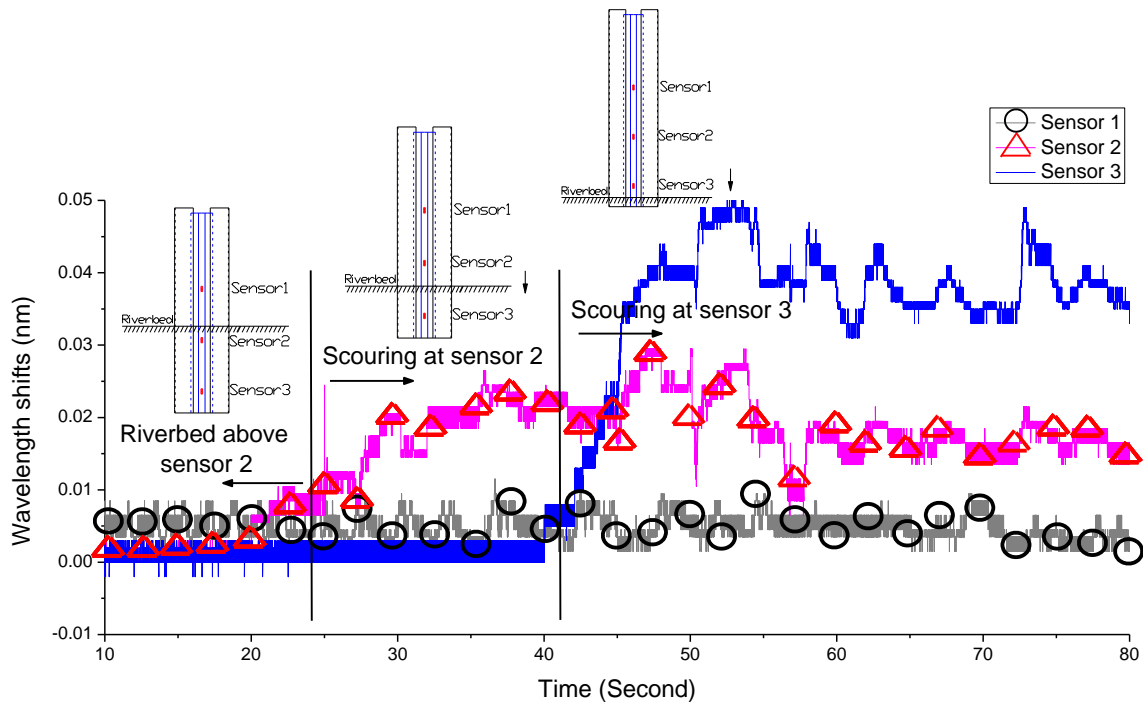


Figure 125
Experimental results of case 2

Experimental Results for Case 3

To investigate the processes of both scour and deposition on the riverbed, the experimental test of case 3 is conducted. In case 3, only the result from sensor 2 is shown in Figure 126 for a clear demonstration. With the same experimental setup as previous cases, sensor 2 is buried under the riverbed at the beginning of the experiment. The experiment starts by releasing the given discharge from the upstream end of the flume. As the running water level rises gradually, the washed-away sands and gravels indicate that the scour is developing. After a time of 25s in Figure 126, sensor 2 emerges and senses the bending strain which is generated by the flowing water acting on the cantilevered steel bar. This developing scour is directly reflected by the wavelength shifts of sensor 2 and lasts until a time of 50s. After the time of

50s, scour stops temporarily. Then, sensor 2 is buried again by the refilled sands and gravels and the reading of sensor 2 consequently decreases and remains in low values until the time of 70s. To stimulate this deposition (refilling) process, extra sands and gravels are poured directly near the steel tube (i.e., the scour monitoring instrument) after the time of 50s and meanwhile the discharge velocity decreases to keep the deposition status. After the time of 70s, the refilling process ends and scour develops again. During this period, the discharge velocity goes up and the running water begins to re-erode the riverbed. As a result, the sensor 2 emerges again from the riverbed and the reading of sensor 2 increases again which is similar to the initial increasing. It is clear to see that the refilling process can be entirely monitored using this proposed instrumentation design and the deposition height can be also determined by the emerging sensor positions.

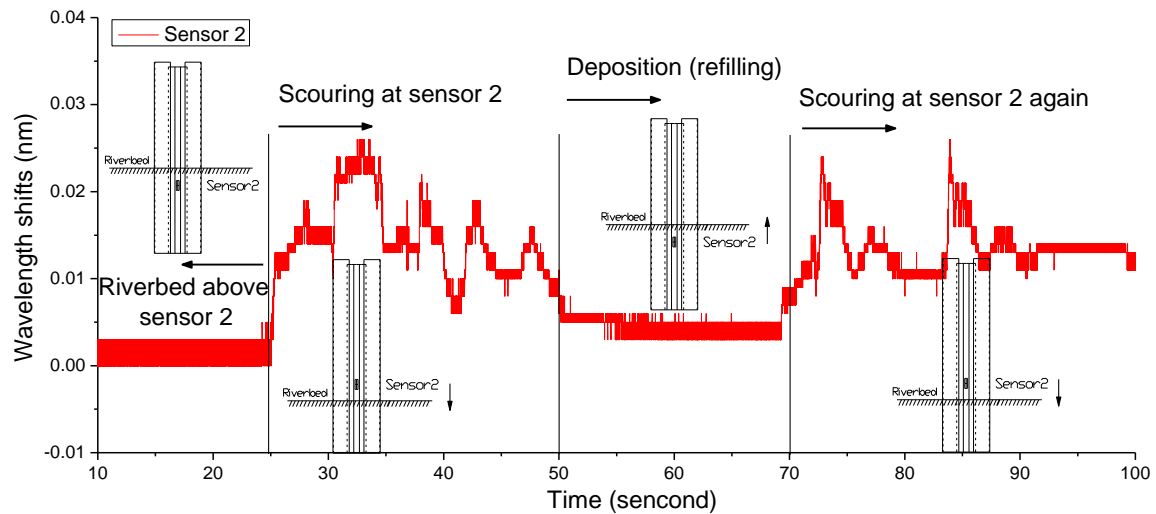


Figure 126
Experimental results of case 3

Based on the three cases of experiments, apparently, the proposed scour monitoring system using FBG sensors is capable of measuring the maximum scour depth and the whole process of scour development including soil deposition. Using the same monitoring principle, the deposition height can also be detected and monitored.

Field Monitoring Results

Data Collection

After the testing piles were installed in position and the cables were led to the bridge approach, as shown in Figure 127, it became easy to take measurements at any time. However, for most of the time, there is only a small amount of water in the river, as shown in Figure 128(b). The river could be filled with a large amount of water only when it has rained upstream, as shown in Figure 128 (a) (c) and (d).



Figure 127
Field data collection

Up until now, data collections have been conducted successfully four times, as listed below:

- 5/24/2013: The river was full of water, but the cable has not been lead to the bridge deck; therefore, no data was measured.
- 5/28/2013: After the flood passed, the cable was led to the deck and the data was collected. There was no water for test pile II (side), and the water was almost static for test pile I (middle).
- 7/16/2013: There was almost no water in the river, as shown in Figure 54, but data was collected for comparison with the future high water cases.
- 9/21/2013: The river was filled with water and data was collected for both piles. The water level was about 20 ft. (6.1 m) to the deck top.
- 2/22/2014: The river was filled with water and data was collected for both piles. The water level was about 17 ft. (5.2 m) to the deck top.



(a) Flood came on 2013-05-24



(b) Flood passed on 2013-05-28



(c) Data collection on 2013-09-21



(d) Data collection on 2014-02-22

Figure 128
Water conditions of different dates

Field Results of Pile I

As shown earlier in Figure 55, 10 sensors survived for the middle pile (Pile I) and 14 sensors for the side pile (Pile II). Figure 129 shows the original signal measured from FBG sensor I-1. From top to bottom, the signals were measured on dates, 2013-05-28, 2013-07-16, 2013-09-21, and 2014-02-22, respectively. The top two measurements are not obvious due to the shallow water in the river. The bottom two measurements are more significant because there was high water in the river.

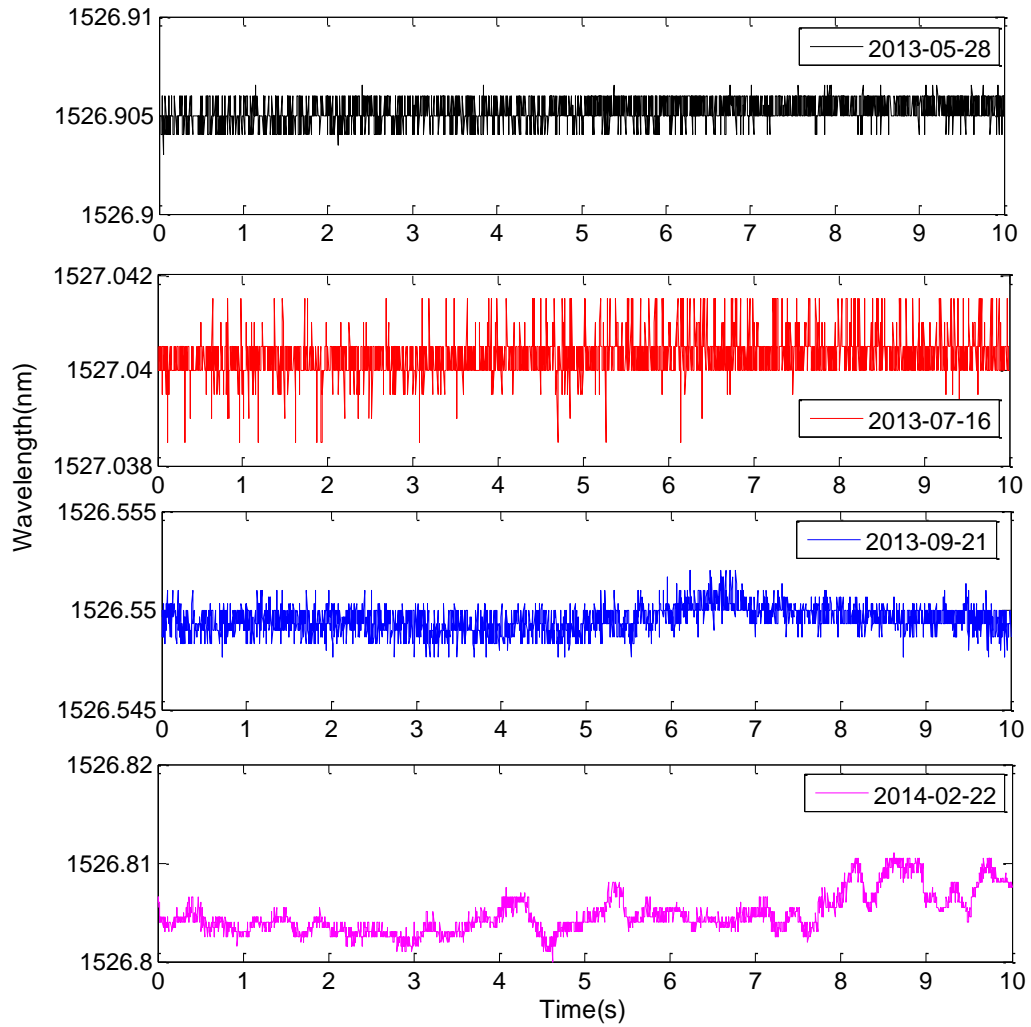


Figure 129
Original signal of Sensor I-1

The original signal is the wavelength of the optical fiber. For easy understanding, the wavelength is converted to micro strain using equation (17) mentioned earlier. The strain-change of sensors is shown in Figure 130. As can be seen, the strain change of data on 2014-02-22 is very significant, more than two times greater than others.

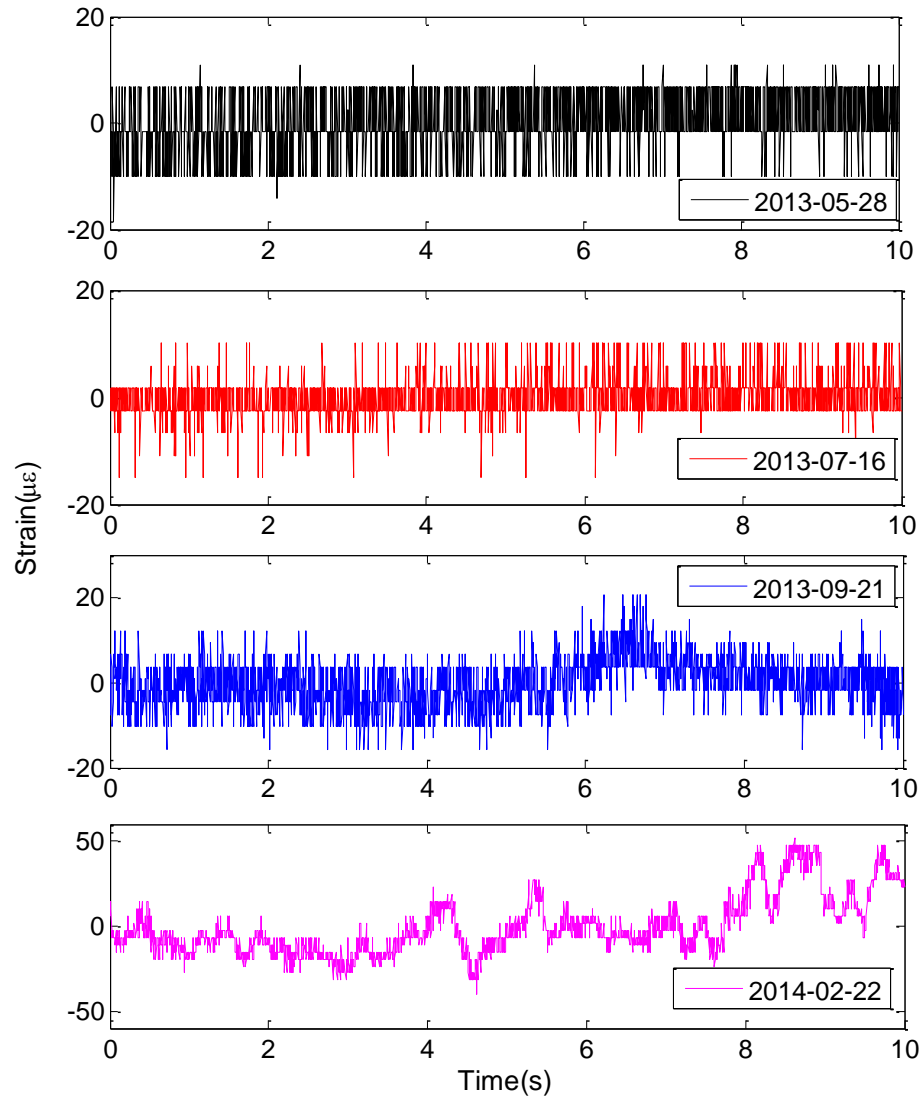


Figure 130
Strain response of Sensor I-1

Since the sensors in the same segment have similar responses, some of the sensors on Pile I are selected for discussion. The strain changes along Pile I measured on the three separate dates, 2013-05-28, 2013-09-21, and 2014-02-22, are shown in Figure 131 ~ Figure 133. As can be seen, on days 2013-05-28 and 2013-07-16 (not shown here), the sensors along the entire pile have small responses, which is consistent with the condition of low water in the river. However, significant responses can be observed on sensors I-1, I-3, I-6, and I-8 in Figure 132 and Figure 133, and slight response on sensor I-9. This difference indicates that sensors I-1 to I-8 are no longer covered with soil and sensors I-9 and I-10 are still covered with soil, which means the soil level was already scoured to the position of between sensor I-8 and I-9. The top three segments of test pile I are already exposed out of the riverbed.

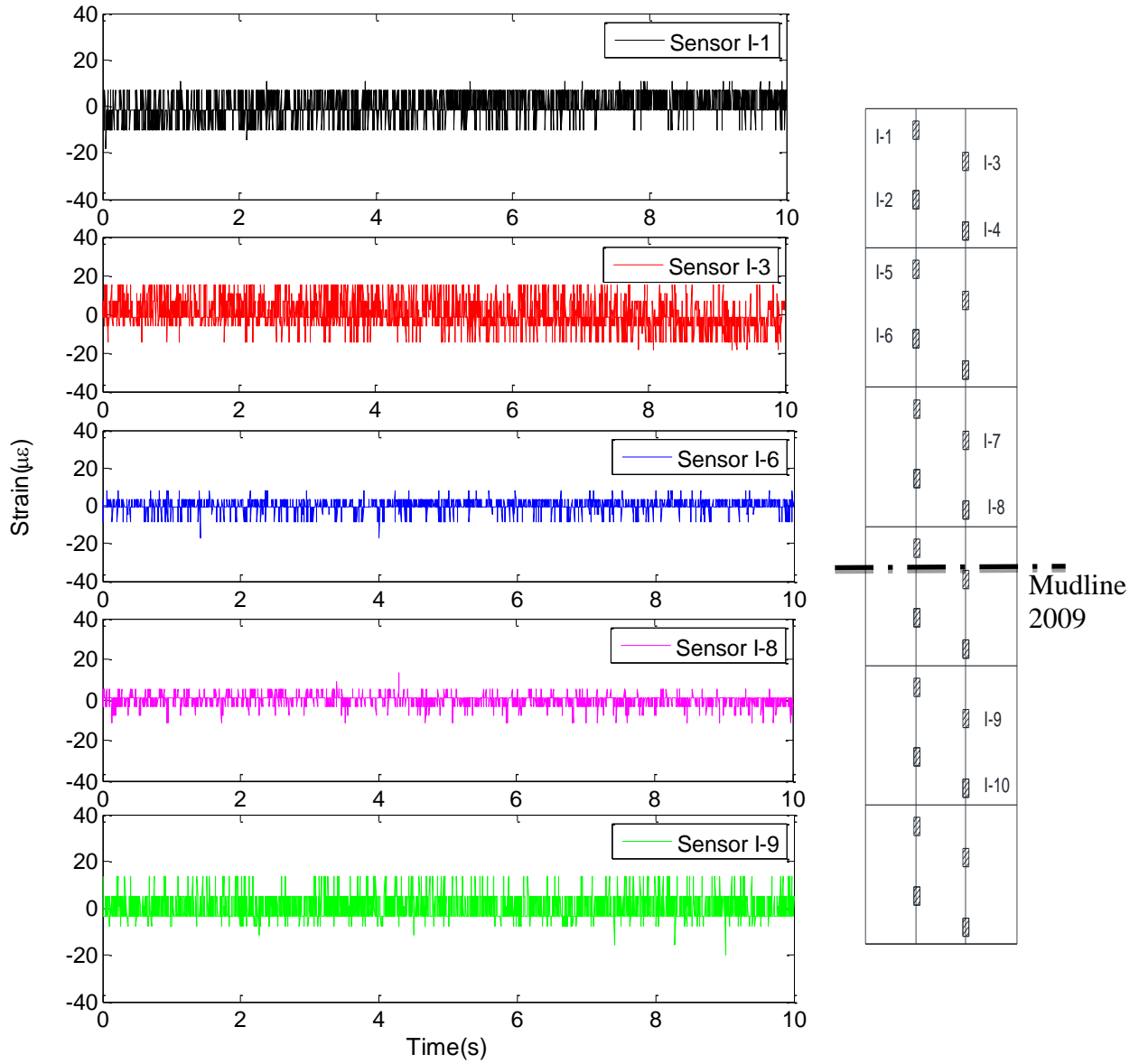


Figure 131
Pile-I data on 2013-05-28

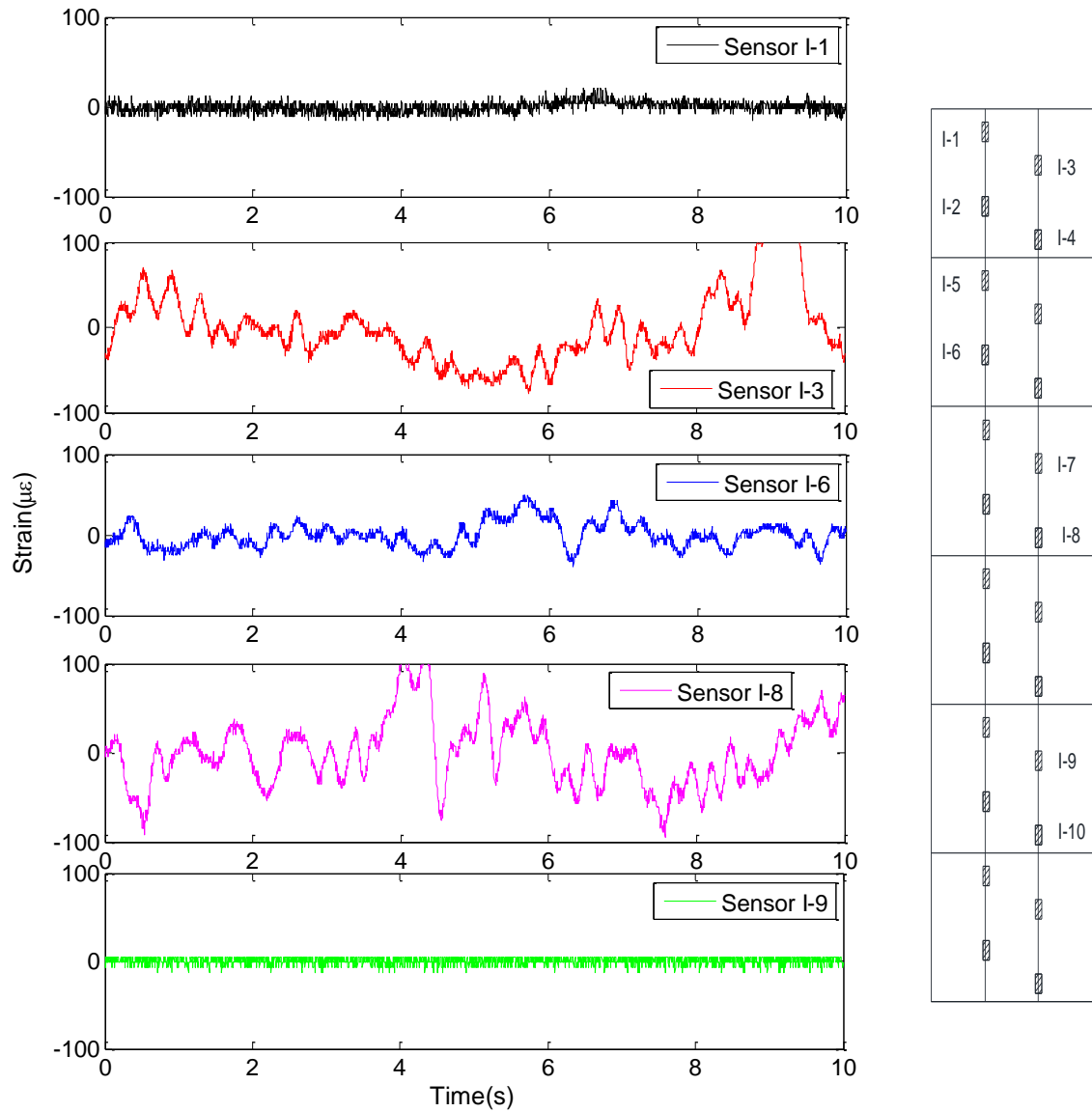


Figure 132
Pile-I data on 2013-09-21

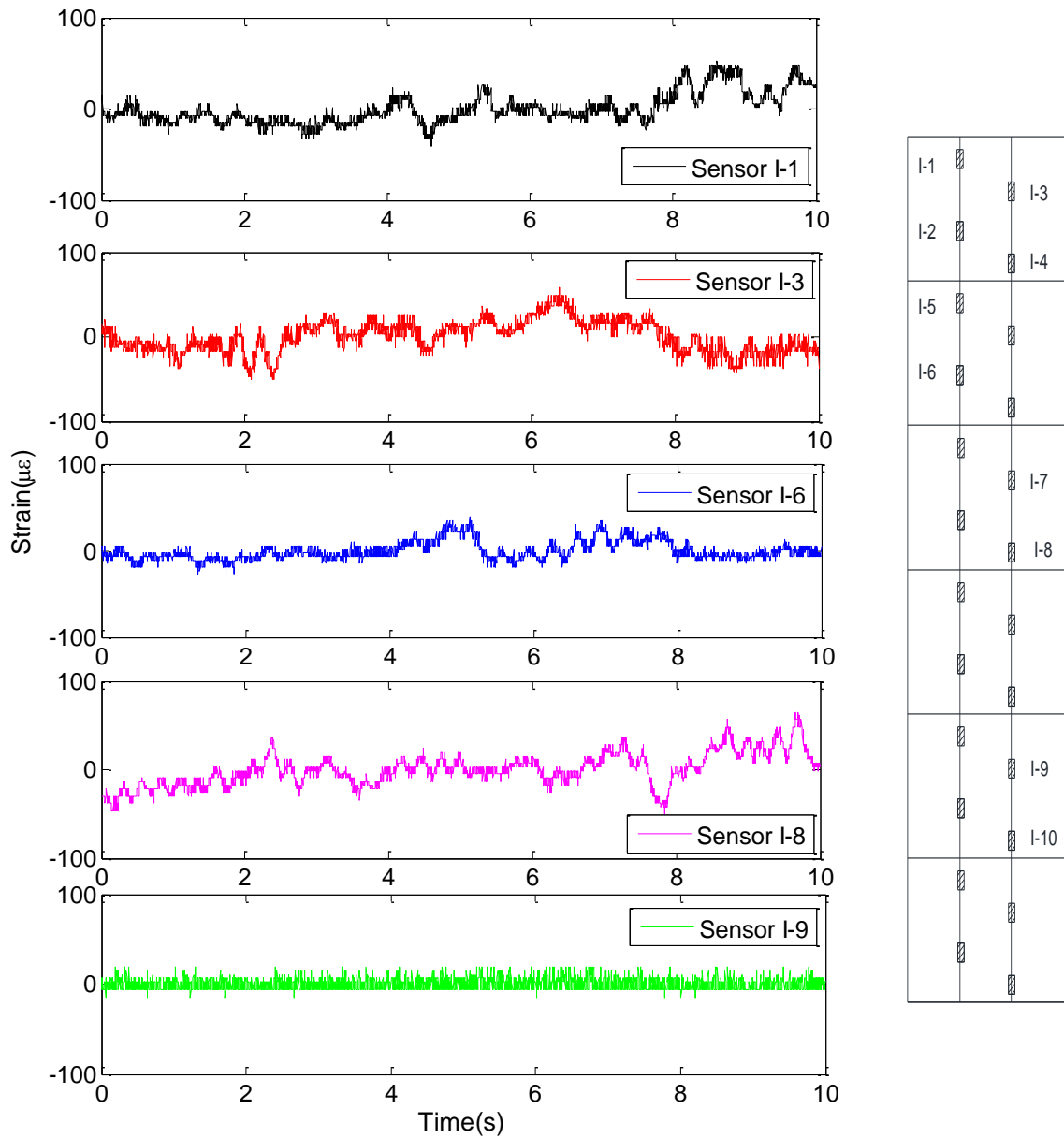


Figure 133
Pile-I data on 2014-02-22

Field Results of Pile II

Due to the small water velocity around the test pile II, the responses of all sensors are small. Herein, only responses of sensor II-1 are shown in Figure 134.

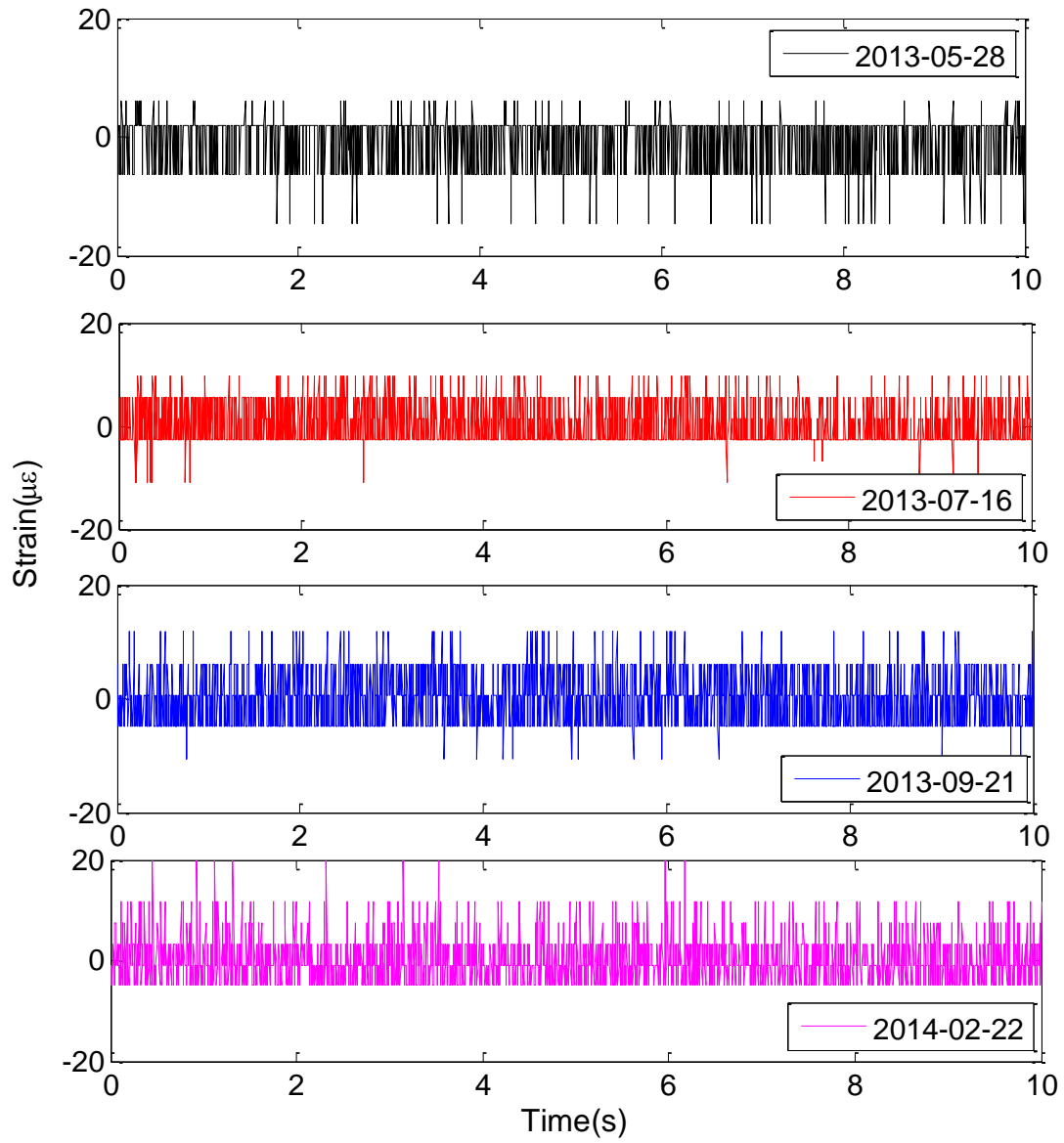


Figure 134
Data of Sensor II-1

CONCLUSIONS

The present study has developed bridge scour monitoring techniques using fiber optic sensors. Based on theoretical and numerical studies, laboratory verifications, and field tests, the following conclusions can be drawn:

- (1) The bending test of the GFRP pipe buried in sand at different heights has verified the numerical observations, that is, the position of the maximum moment (strain) in the pile is close to the interface of the sand and water. It has also confirmed the feasibility of the scour monitoring method based on the bending moment (strain) profile.
- (2) In order to measure and monitor the scour depth variations in real time, including the soil deposition (refilling) process, three designs for a scour monitoring system using FBG sensors were discussed in the present study and the third one is highly recommended for field applications. A verification test using a flume was carried out in the laboratory and it demonstrated the applicability of the recommended scour monitoring system. The advantages over other conventional scour monitoring systems have been proven.
- (3) The field monitoring has shown that significant responses can be observed on sensors I-1, I-3, I-6, and I-8 and slight response on I-9, which indicates that the soil level is already to the position of sensor 8. The top three segments of the test pile I are already exposed out of the riverbed.

RECOMMENDATIONS

Based on the initial results obtained from this research program, the following recommendations are made:

- Based on the tests in the laboratory and monitoring on the field bridge up until now, the proposed monitoring instrumentation performed very well and is recommended for additional applications on bridges in Louisiana.
- Periodical visual inspection of the water and riverbed level should be carried out.
- Long-term scour monitoring should be ensured by periodically taking measurements from the permanently installed monitoring plies with FBG sensors.
- Currently, measurements are carried out by field trips and it is very difficult to know in advance if a high water and scour event has occurred. For practical application, on-line monitoring technology using fiber optic sensors should be developed, which can continuously monitor the scour process.

REFERENCES

1. Lin, Y. B., Chang, K. C., Lai, J. S., and Wu, I. W. "Application of Optical Fiber Sensor on Local Scour Monitoring." Proceedings of the IEEE Sensors, 2004, 2, pp. 832-835, Vienna, Austria.
2. Shirole, A. M., and Holt, R. C. "Planning for a Comprehensive Bridge Safety Program." Transportation Research Record 1290, Transportation Research Board, National Research Council, Washington, D.C, 1991.
3. Kattell, J., and Eriksson, M. "Bridge Scour Evaluation: Screening, Analysis, and Countermeasures." Pub. No. 9877 1207P, Washington DC: USDA Forest Service, 1998.
4. Lagasse, P. F., Richardson, E. V., Schall, J. D., and Price, G. R. "Instrumentation for Measuring Scour at Bridge Piers and Abutments." National Cooperative Highway Research Program, NCHRP Report 396, 1997.
5. Parker, G.W., Bratton, L., and Armstrong, D.S. "Stream Stability and Scour Assessments at Bridges in Massachusetts." U.S. Geological Survey Open File Report 97-588, 53 p, 2 CD-ROMs, 1997.
6. Richardson, E. V., and Davis, S. R. "Evaluating Scour at Bridges (3rd ed.)." Federal Highway Administration Hydraulic Engineering Circular No. 18, FHWA-IP-90-017, 203 p, Washington, DC, 2001.
7. Laursen, E. M., and Toch, A. "Scour Around Bridge Piers and Abutments." Bull. No. 4, Iowa Highway Research Board, Ames, Iowa, 1956.
8. Liu, H. K., Chang, F. M., and Skinner, M. M. "Effect of Bridge Constriction on Scour and Backwater." Report CER60HKL22, Department of Civil Engineering, Colorado State University, Fort Collins, CO, 1961.
9. Shen, H. W., Schneider, V. R., and Karaki, S. "Local Scour around Bridge Piers." Proceeding of ASCE, 95(6), 1969, pp. 1919-1940.
10. Breusers, H. N. C., Nicollet, G., and Shen, H. W. "Local Scour around Cylindrical Piers." *Journal of Hydraulic Research*, 15(3), 1977, pp. 211-252.
11. Jain, S. C., and Fischer, E. E. "Scour around Bridge Piers at High Froude Numbers." Report FHWA-RD-79-104, Federal Highway Administration, Washington D.C., 1979.
12. Melville, B. W., and Sutherland, A. J. "Design Method for Local Scour at Bridge Piers." *Journal of Hydraulic Engineering*, 114(10), 1988, pp. 1210-1226.
13. Froehlich, D. C. "Local Scour at Bridge Abutments." Proceedings of the 1989 National Conference on Hydraulic Engineering, ASCE, 1989, pp. 13-18, New York, NY, USA.
14. Melville, B. W. "Local Scour at Bridge Abutments." *Journal of Hydraulic Engineering*, 118(4), 1992, pp. 615-631.

15. Abed, L., and Gasser, M. M. "Model Study of Local Scour Downstream Bridge Piers." Proceedings of the National Conference on Hydraulic Engineering, 1993, pp. 1738-1743, San Francisco, CA, USA.
16. Richardson, J. R., and Richardson, E. V. "Practical Method for Scour Prediction at Bridge Piers." Proceedings of the ASCE National Conference on Hydraulic Engineering, 1994, pp. 1-5, Buffalo, NY, USA.
17. Lim, S.-Y. "Equilibrium Clear-water Scour around an Abutment." *Journal of Hydraulic Engineering*, 123(3), 1997, pp. 237-243.
18. Heza, Y. B. M., Soliman, A. M., and Saleh, S. A. "Prediction of the Scour Hole Geometry around Exposed Bridge Circular-pile Foundation." *Journal of Engineering and Applied Science*, 54(4), 2007, pp. 375-392.
19. Federal Highway Administration. "Evaluating Scour at Bridges." Hydraulic Engineering Circular No. 18, Report No. FHWA-IP-90-017, Federal Highway Administration (FHWA), U.S. Department of Transportation, Washington, D.C., 1993.
20. Neil, C. R. "River Bed Scour, a Review for Bridge Engineers." Contract No. 281, Research Council of Alberta, Calgary, Alberta, Canada, 1964.
21. Jones, J. S. "Comparison of Prediction Equations for Bridge Pier and Abutment Scour." Transportation Research Record, Second Bridge Engineering Conference, v 2, 202-209, Transportation Research Board, Washington, D.C., 1984.
22. Johnson, P. A. "Comparison of Pier-scour Equations Using Field Data." *Journal of Hydraulic Engineering*, 121(8), 1995, pp. 626-629.
23. Landers, M. N., and Mueller, D. S. "Evaluation of Selected Pier-scour Equations Using Field Data." Transportation Research Record, 1523, 1996, pp. 186-195.
24. Mueller, D. S. "Local Scour at Bridge Piers in Non-uniform Sediment under Dynamic Conditions." Dissertation in partial fulfillment of the requirements for the Degree of Doctor of Philosophy, Colorado State University, Fort Collins, CO, 1996.
25. Landers, M. N., Mueller, D. S., and Richardson, E. V. "U.S. Geological Survey Field Measurements of Pier Scour." *ASCE Compendium, Stream Stability and Scour at Bridges*, Richardson and Lagasse (eds.), Reston, VA, 1999.
26. Johnson, P. A., and Ayyub, B. M. "Modelling Uncertainty in Prediction of Pier Scour." *Journal of Hydraulic Engineering*, 122(2), 1996, pp. 66-72.
27. Melville, B. W. "Pier and Abutment Scour-integrated Approach." *Journal of Hydraulic Engineering*, 123(2), 1997, pp. 125-136.
28. Ataie-Ashtiani, B., and Beheshti, A. A. "Experimental Investigation of Clear-water Local Scour at Pile Groups." *Journal of Hydraulic Engineering*, 132(10), 2006, pp. 1100-1104.

29. Benedict, S. T., Deshpande, N., and Aziz, N. M. "Evaluation of Abutment Scour Prediction Equations with Field Data." *Transportation Research Record*, 2025, 2007, pp. 118-126.
30. Lu, J. Y., Hong, J. H., Su, C. C., Wang, C. Y., and Lai, J. S. "Field Measurements and Simulation of Bridge Scour Depth Variation during Floods." *Journal of Hydraulic Engineering*, 134(6), 2008, pp. 810-821.
31. Ettema, R. "Scour at Bridge Piers." Report No. 216, University Of Auckland, School of Engineering, New Zealand, 1980.
32. Yanmaz, A. M., and Altinbilek, H. D. "Study of Time-dependent Local Scour around Bridge Piers." *Journal of Hydraulic Engineering*, 117(10), 1991, pp. 1247-1268.
33. Kothyari, U., Garde, R., and Ranga Raju, K. "Temporal Variation of Scour around Circular Bridge Piers." *Journal of Hydraulic Engineering*, 118(8), 1992, pp. 1091-1106.
34. Cardoso, A. H., and Bettess, R. "Effect of Time and Channel Geometry on Scour at Bridge Abutments." *Journal of Hydraulic Engineering*, 125(4), 1999, pp. 388-399.
35. Melville, B. W., and Chiew, Y. M. "Time Scale for Local Scour at Bridge Piers." *Journal of Hydraulic Engineering*, 125(1), 1999, pp. 59-65.
36. Oliveto, G., and Hager, W. H. "Temporal Evolution of Clear-water Pier and Abutment Scour." *Journal of Hydraulic Engineering*, 128(9), 2002, pp. 811-820.
37. Chang, W. Y., Lai, J. S., and Yen, C. L. "Evolution of Scour Depth at Circular Bridge Piers." *Journal of Hydraulic Engineering*, 130(9), 2004, pp. 905-913.
38. Choi, S. U., and Cheong, S. "Prediction of Local Scour around Bridge Piers Using Artificial Neural Networks." *Journal of the American Water Resources Association*, 42(2), 2006, pp. 487-494.
39. Bateni, S. M., Borghei, S. M., and Jeng, D. S. "Neural Network and Neuro-fuzzy Assessments for Scour Depth around Bridge Piers." *Engineering Applications of Artificial Intelligence*, 20(3), 2007, pp. 401-414.
40. Lee, T. L., Jeng, D. S., Zhang, G. H., and Hong, J. H. "Neural Network Modeling for Estimation of Scour Depth around Bridge Piers." *Journal of Hydrodynamics*, 19(3), 2007, pp. 378-386.
41. Mohammad, Z. K., Beheshti, A. A., and Behzad, A. A. "Estimation of Current-induced Scour Depth around Pile Groups Using Neural Network and Adaptive Neuro-fuzzy Inference System." *Applied Soft Computing*, 9, 2009, pp. 746-755.
42. Fukuoka, S., Tomita, K., Hotta, T., and Miyagawa, T. "Practical Numerical Simulation of Local Scour around a Bridge Pier." *Proceedings of the Japan Society of Civil Engineers*, p71-79, Tokyo, Japan, 1994.

43. Richardson, J. E., and Panchang, V. G. "Three-dimensional Simulation of Scour-inducing Flow at Bridge Piers." *Journal of Hydraulic Engineering*, 124(5), 1998, pp. 530-540.
44. Melville, B. W., and Raudkivi, A. "Flow Characteristics in Local Scour at Bridge Piers." *Journal of Hydraulic Research*, IAHR, 15(4), 1977, pp. 373-380.
45. Young, G. K., Dou, X., Saffarinia, K., and Jones, J. S. "Testing Abutment Scour Model." Proceedings of the 1998 International Water Resources Engineering Conference, v 1, 1998, pp. 180-185. Memphis, TN, USA.
46. Kassem, A., Salaheldin, T. M., Imran, J., and Chaudhry, M. H. "Numerical Modeling of Scour around Artificial Rock Island of Cooper River Bridge." *Transportation Research Records* 1851, 2003, pp. 45-50.
47. Umbrell, E. R., Young, G. K., Stein, S. M., and Jones, J. S. "Clear-water Contraction Scour under Bridges in Pressure Flow." *Journal of Hydraulic Engineering*, 124(2), 1998, pp. 236-240.
48. Sheppard, D. M., and William, M. Jr. "Live-bed Local Pier Scour Experiments." *Journal of Hydraulic Engineering*, 132(7), 2006, pp. 635-642.
49. Sheppard, D. M. "Large-scale and Live-bed Local Pier Scour Experiments." Coastal Engineering Technical Rep. No. 133, Civil and Coastal Engineering Dept., Univ. of Florida, Gainesville, Fla, 2003.
50. Gorin, S. R., and Haeni, F.P. "Use of Surface-geophysical Methods to Assess Riverbed Scour at Bridge Piers." U.S. Geological Survey Water-Resources Investigations Report 88-4212, 1989, pp. 33.
51. Horne, W. A. "Scour Inspection Using Ground Penetrating Radar." Proceedings of the National Conference on Hydraulic Engineering, 1993, pp. 1888-1893, San Francisco, CA, USA.
52. Millard, S. G., Bungey, J. H., Thomas, C., Soutsos, M. N., Shaw, M. R., and Patterson, A. "Assessing Bridge Pier Scour by Radar." *NDT & E International*, 31(4), 1998, pp. 251-258.
53. Park, I., Lee, J., and Cho, W. "Assessment of Bridge Scour and Riverbed Variation by a Ground Penetrating Radar." Proceedings of the Tenth International Conference Ground Penetrating Radar, GPR, 2004, pp. 411-414, Delft, Netherlands.
54. Mason, R. R., and Shepard, D. M. "Field Performance of an Acoustic Scour-depth Monitoring System." *Proceeding of Fundamentals and Advancements in Hydraulic Measurements and Experimentation*, 1994, pp. 366-375, New York, USA.
55. Hayes, D. C., and Drummond, F. E. "Use of Fathometers and Electrical-conductivity Probes to Monitor Riverbed Scour at Bridges and Piers." *Water Resource Investigations Rep. No. 94-4164*, U.S. Geological Survey, Hartford, Connecticut, 1995.

56. De Falco, F., and Mele, R. "The Monitoring of Bridges for Scour by Sonar and Sediment." *NDT & E International*, 35(2), 2002, pp. 117-123.
57. Hunt, B. E. "Scour Monitoring Programs for Bridge Health." *The 6th International Bridge Engineering Conference: Reliability, Security, and Sustainability in Bridge Engineering*, Transportation Research Board, 2005, pp. 531-536, Boston, MA, USA.
58. Yankielun, N. E., and Zabilansky, L. "Laboratory Investigation of Time-domain Reflectometry System for Monitoring Bridge Scour." *Journal of Hydraulic Engineering*, 125(12), 1999, pp. 1279-1284.
59. Yu, X., and Zabilansky, L. J. "Time Domain Reflectometry for Automatic Bridge Scour Monitoring." *Geotechnical Special Publication*, 149, 2006, pp. 152-159.
60. Yu, X., and Yu, X. "Algorithm for Time Domain Reflectometry Bridge Scour Measurement System." *The 7th International Symposium on Field Measurements in Geomechanics, FMGM*, 2007, pp. 1-10, Boston, MA, USA.
61. Lin, Y. B., Chen, J. C., Chang, K. C., Chern, J. C., and Lai, J. S. "Real-time Monitoring of Local Scour by Using Fiber Bragg Grating Sensors." *Smart Materials and Structures*, 14(4), 2005, pp. 664-670.
62. Deng, L., and Cai, C. S. "Applications of Fiber Optic Sensors in Civil Engineering." *Structural Engineering and Mechanics, an International Journal*, 25(5), 2007, pp. 577-596.
63. Lagasse, P. F., Clopper, P. E., Zevenbergen, L. W., and Girard, L. G. "Countermeasures to Protect Bridge Piers from Scour." *National Cooperative Highway Research Program, NCHRP Report 593*, Transportation Research Board, Washington, D.C., 2007.
64. Barkdoll, B. D., Ettema, R., and Melville, B. W. "Countermeasures to Protect Bridge Abutments From Scour." *National Cooperative Highway Research Program, HCHRP Report 587*, Transportation Research Board, Washington, D.C., 2007.
65. Lauchlan, C. S., and Melville, B. W. "Riprap Protection at Bridge Piers." *Journal of Hydraulic Engineering*, 127(5), 2001, pp. 412-418.
66. Odgaard, A. J., and Wang, Y. "Scour Prevention at Bridge Piers." *Proceeding of the 1987 National Conference on Hydraulic Engineering*, 1987, pp. 523-527, New York, NY, USA.
67. Chiew, Y. M., and Lim, S. Y. "Protection of Bridge Piers Using a Sacrificial Sill." *Proceedings of the Institution of Civil Engineers: Water and Maritime Engineering*, 156(1), 2003, pp. 53-62.
68. Kumar, V., Ranga Raju, K. G. and Vittal, N. "Reduction of Local Scour around Bridge Piers Using Slots and Collars." *Journal of Hydraulic Engineering*, 125(12), 1999, pp. 1302-1305.

69. Zarrati, A. R., Nazahira, M., and Mashahir, M. B. "Reduction of Local Scour in the Vicinity of Bridge Pier Groups Using Collars and Riprap." *Journal of Hydraulic Engineering*, 132(2), 2006, pp. 154-162
70. Li, H., Barkdoll, B. D., Kuhnle, R., and Alonso, C. "Parallel Walls as an Abutment Scour Countermeasure." *Journal of Hydraulic Engineering*, 132(5), 2006, pp. 510-520.
71. Grimaldi, C., Gaudio, R., Calomino, F., and Cardoso, A. H. "Control of Scour at Bridge Piers by a Downstream Bed Sill." *Journal of Hydraulic Engineering*, 135(1), 2009, pp. 13-21.
72. Johnson, P. A., and Niezgod, S. L. "Risk-based Method for Selecting Bridge Scour Countermeasures." *Journal of Hydraulic Engineering*, 130(2), 2004, pp. 121-128.
73. Lagasse, P. F., Zevenbergen, L. W., Schall, J. D. and Clopper, P. E. "Bridge Scour and Stream Instability Countermeasures: Experience, Selection, and Design Guidelines." FHWA NHI 01-003: Federal Highway Administration, Hydraulic Engineering Circular No. 23, 2nd ed., U.S. Department of Transportation, Washington, D.C., 2001.
74. Molinas, A., and Abdeldayem, A. "Effect of Clay Content on Bridge Scour." Proceedings of the 1998 International Water Resources Engineering Conference. Part 1 (of 2), 1998, pp. 280-285, Memphis, TN, USA.
75. Molinas, A., Jones, S., and Hosny, M. "Effects of Cohesive Material Properties on Local Scour around Piers." Transportation Research Record, 1690, 1999, pp. 164-174.
76. Bertoldi, D., and Kilgore, R. "Tetrapods as a Scour Countermeasure." Proceedings of the National Conference on Hydraulic Engineering, 1993, pp. 1385-1395, San Francisco, CA, USA.
77. Melville, B. W., and Raudkivi, A. J. "Effects of Foundation Geometry on Bridge Pier Scour." *Journal of Hydraulic Engineering*, 122(4), 1996, pp. 203-209.
78. El-Razek, M. A., El-Motaleb, M. A., and Bayoumy, M. "Scour Reduction around Bridge Piers Using Internal Openings Through the Pier." AEJ-Alexandria Engineering Journal, 42(2), 2003, pp. 241-248.
79. Parola, A. C., Mahavadi, S. K., and Brown, B. M. "Effects of Rectangular Foundation Geometry on Local Pier Scour." *Journal of Hydraulic Engineering*, 122(1), 1996, pp. 35-40.
80. Bozkus, Z., and Yildiz, O. "Effects of Inclination of Bridge Piers on Scouring Depth." *Journal of Hydraulic Engineering*, 130(8), 2004, pp. 827-832.
81. Lagasse, P.F. and Nordin, C. F. "Scour Measuring and Monitoring Equipment for Bridges." *Hydraulic Engineering*, 1991, pp. 311.
82. Schall, J.D., Fischer G.A., Price, G.R., "Scour Monitoring at Johns Pass and Nassau Sound, Florida." *Hydraulic Engineering*, 1995.

83. Ding, Z. "A General Solution to Vibrations of Beams on Variable Winkler Elastic Foundation." *Computer & Structures*, Vol.47, No.1, 1993, pp. 83-90.
84. Coskun, I. "The Response of a Finite Beam on a Tensionless Pasternak Foundation Subjected to a Harmonic Load." *European Journal of Mechanics/Solids*, 22, 2003, pp. 151-161.
85. Clough, R., and Penzien, J. *Dynamics of Structures*. Computer and Structures, Inc., 2003.
86. Deng, L., and Cai, C. S. "Bridge Scour: Prediction, Modeling, Monitoring, and Countermeasures—Review." *Practice Periodical on Structural Design and Construction, ASCE*, Vol. 15, No. 2, 2010, pp. 125–134.
87. Deng, L., and Cai, C. S. "Applications of Fiber optic Sensors in Civil Engineering." *Structural Engineering and Mechanics*, 25(5), 2007, pp. 577-596.
88. Lu, J. Y., Hong, J. H., Su, C. C., Wang, C. Y., and Lai, J. S. "Field Measurements and Simulation of Bridge Scour Depth Variation During Floods." *Journal of Hydraulic Engineering*, 134(6), 2008, pp. 810-821.
89. Rytter, A. "Vibration Based Inspection of Civil Engineering Structures." Ph. D. Dissertation, Department of Building Technology and Structural Engineering, Aalborg University, Denmark, 1993.
90. Schlichting, H. *Boundary-Layer Theory*, McGraw-Hill, New York, 1968.
91. Casas, J. R., and Cruz, P. J. S. "Fiber Optic Sensors for Bridge Monitoring." *Journal of Bridge Engineering*, 8(6), 2003, pp. 362-373.
92. Kersey, A. D., Davis, M. A., and Patrick, H. J. "Fiber Grating Sensor." *Journal of Lightwave Technology*, 15(8), 1997, pp. 1442-1463.
93. Xu, M. G., Dong, L., Reekie, L., Tucknott, J. A., and Cruz, J. L. "Temperature-independent Strain Sensor Using a Chirped Bragg Grating in a Tapered Optical Fiber." *Electronics Letters*, 31(10), 1995, pp. 823-825.
94. Idriss, R.L., Kodindouma, M.B., Kersey, A.D. and Davis, M.A. "Multiplexed Bragg Grating Optical Fiber Sensors for Damage Evaluation in Highway Bridges." *Smart Materials and Structures*, 7(2), 1998, pp. 209-216.
95. Miridonov, S. V., Shlyagin, M. G., and Tentori-Santa-Cruz, D. "Digital Demodulation of a Twin-grating Fiber Optic Sensor." *Fiber Optic and Laser Sensors and Applications Including Distributed and Multiplexed Fiber Optic Sensors VII*, Proceedings SPIE, 3541, 1999, pp. 33-40.
96. Tennyson, R.C., Coroy, T., Duck, G., Manuepillai, G., Mulvihill, P., Cooper, David J.F., Smith, P.W.E., Mufti, A.A. and Jalali, S.J. "Fiber Optic Sensors in Civil Engineering Structures." *Canadian Journal of Civil Engineering*, 27(5), 2000, pp. 880-889.

97. Li, H., Li, D., and Song, G. "Recent Applications of Fiber Optic Sensors to Health Monitoring in Civil Engineering." *Engineering Structures*, Vol. 26, 2004, pp. 1647-1657.
98. Leung, C. K. Y., Elvin, N., Olson, N., Morse, T. F., and He, Y. F. "A Novel Distributed Optical Crack Sensor for Concrete Structures." *Engineering Fracture Mechanics*, Vol. 65, No. 2-3, 2005, pp. 133-148.

ACRONYMS, ABBREVIATIONS, & SYMBOLS

μ	Poisson's ratio
$\mu\varepsilon$	micro strain
cm	centimeter(s)
DOF	degree of freedom
E_x	Elastic modulus along longitudinal axis
E_y	Elastic modulus along lateral axis
FBG	Fiber Bragg Grating
FEM	Finite Element Model
FFT	Fast Fourier Transform
FHWA	Federal Highway Administration
ft.	foot (feet)
FOS	Fiber Optic Sensor
FRP	Fiber Reinforced Polymer
GFRP	Glass Fiber Reinforced Polymer
G_T	Temperature gauge factor
G_{xy}	Modulus of rigidity
G_ε	Strain gauge factor
in.	inch (es)
kHz	kilo hertz
kip	kilo Pounds
DOTD	Louisiana Department of Transportation and Development
lb.	pound (s)
LTRC	Louisiana Transportation Research Center
m	meter (s)
mm	millimeter
mph	miles per hour
nm	nanometer
pm	picometer
OTDR	optical time domain reflectometer
$\Delta\varepsilon$	Change in strain
λ_b	Original wavelength

APPENDIX A

Installation Procedure for Fiber Optic FBG

Before discussing the installation procedure, some basics of fiber optic sensors and installations are first introduced below.

Fundamentals of FOS (Fiber Optic Sensing)

An optical fiber basically consists of a flexible dielectric waveguide that traps optical radiation at one end and guides it to the other. An optic fiber usually consists of at least two optically dissimilar materials. A typical fiber is packaged as shown in Figure 135. It is clear that besides the core and cladding mostly made of glass, a few additional layers made of different materials are added to enhance mechanical strength and flexibility properties of the fiber. The core is the main component that carries the light waves and defines two available modes of fiber configurations: single mode (core size $< 10 \mu\text{m}$) and multi-mode (core size $50 \sim 100 \mu\text{m}$) [87], [91].

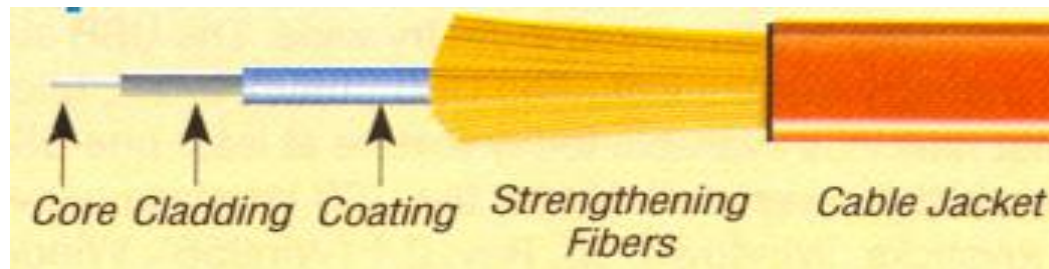


Figure 135
Basic structure of optical fiber

FOS is based on measuring changes in the physical properties such as phase, polarization state, intensity, and wavelength of the guided light. Based on the varied transduction methods of the guided light, FOS can be classified into: intensimetric, interferometric, and spectrometric. The sensing ability of the fiber can yet again categorize FOS into point/local, distributed, or multiplexed sensors. Optical fibers come in two configurations, multi-mode (core size $50 \sim 100 \mu\text{m}$) and single mode (core size $< 10 \mu\text{m}$) [87].

Unique characteristics of the Fiber Bragg Gratings (FBG) and optical time domain reflectometer (OTDR) type FOS sensors have led to favorable structural health monitoring applications.

FOS technology involves the installation of optical fiber sensors that measure strain and temperature in various civil engineering materials such as concrete, steel, composites, etc.

Light waves transmitted down a thin optical cable measure change in signal properties that are correlated to elongation and contraction, measured in microstrains. When fiber optic sensors are used, strain is detected by a special demodulation unit and processed to yield a digital signal. Converting these signals to strains/temperatures is then performed by a data acquisition system. A number of different fiber optic sensors have been developed in recent years, from simple sensors that only measure an on/off state to multiplexed sensors that measure a range of wavelengths.

Monitoring with FBG Optic Fibers

FBG () forms the integral sensing unit of this FOS. The FBG are intrinsic spectrometric sensors with local and multiplexing sensing abilities. An FBG is generated by engraving a periodic modulation of the refractive index of about 0.393 in. (1 cm) in the core of an optical fiber. The basic principle involved in the functioning of a FBG sensor is shown in Figure 136. Usually, the FBG sensor measures strain but can be modulated to measure displacement, acceleration, etc. The achievable resolution for these sensors is 1μ strain and they can have a working range of over 5000 μ strains [97].

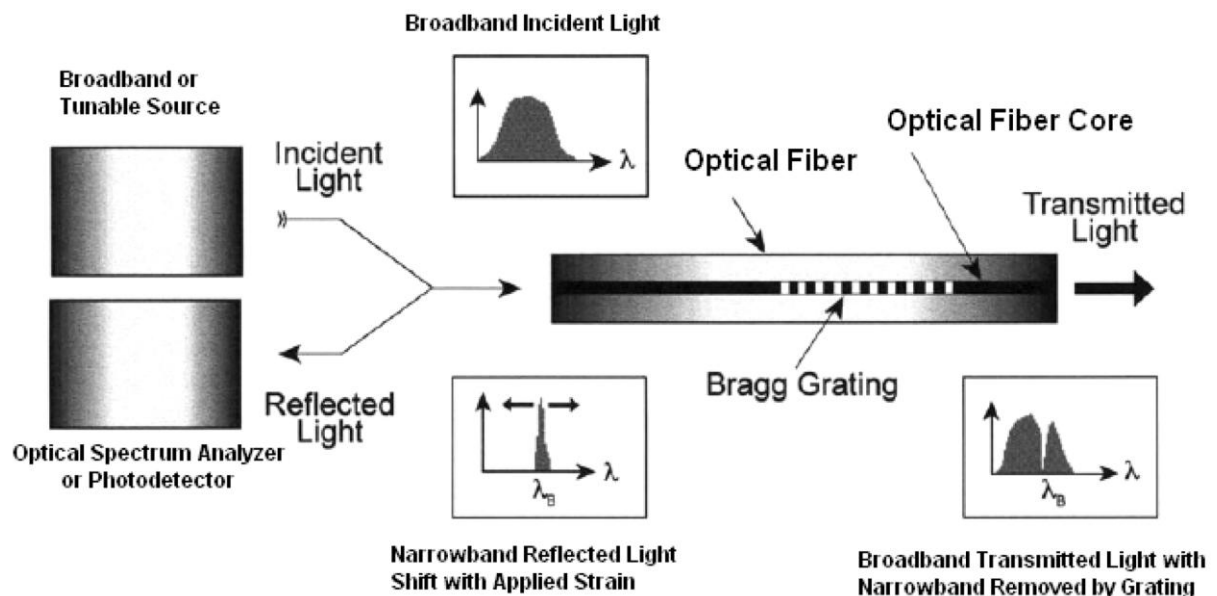


Figure 136
Principle of FBG

The spacing of the grating, called the “pitch,” reflects the incident light with a narrow band centered about the “Bragg” wavelength, defined by:

$$\lambda_0 = 2n\Lambda \quad (27)$$

where, λ_0 is the Bragg wavelength, n is the average effective index of refraction of the grating, and Λ is the pitch spacing.

The FBG also provides a linear response based on the measurement of wavelength shift ($\Delta\lambda$) due to the straining of the gauge. Once temperature effects are accounted for in the wavelength shift, $\Delta\lambda$ provides a means of determining the strain according to the equation:

$$\Delta \lambda / \lambda_0 = (GF) \varepsilon + \beta \Delta T \quad (28)$$

where, $\Delta\lambda = \lambda - \lambda_0$; GF is the FBG gauge factor, typically about 0.75 – 0.82, ε is the strain; β is the thermal coefficient; and ΔT is the temperature change relative to the temperature at installation.

FBG sensors have a unique property over other FOS in that they encode the wavelength that does not suffer from disturbances of the light paths. FBG sensors could be particularly useful when gratings with different periods are arranged along an optical fiber. Each of the reflected signals will have a unique wavelength and can be easily monitored, thus achieving multiplexing of the outputs of multiple sensors using a single fiber. FBG sensors are preferred in many civil engineering applications and have been successfully employed in several structures requiring multi-point sensing distributed over a long range [97].

A major advantage of FBG sensors is that they can be embedded in structures to measure strain. A lot of research has been conducted on the measurement of strain on reinforcement bars. A FBG strain sensor bonded to a piece of rebar (Figure 137) with the jacket of the fiber removed only in the sensing zone is bonded to the polished surface of the rebar by means of special glue. The sensing part is protected by several layers of rubber, and the input/output lead is protected by the fiber jackets [91].

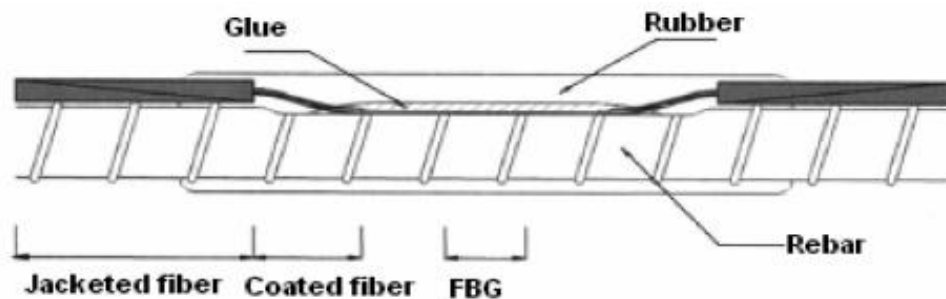


Figure 137
FBG sensors for strain measurement in rebar

Monitoring with OTDR Based Optic Fibers

In simple terms, an OTDR (optical time domain reflectometer) based optic fiber is an intensimetric sensor that carries and modulates the light within the fiber and has a sensing capability throughout the length of the fiber. These sensors can be used to measure either temperature or strain and give a resolution of 19.68 in. (0.5 m) or every 1°C for up to 6561 ft. (2 km) distance [97].

The principle by which these sensors function is illustrated in Figure 138. These sensors are efficient for use in large structures like bridges as all portions of the fiber acts as a sensor, thus enabling monitoring changes along its length. Cracks or local strain changes can lead to a light intensity variation within the fiber that reflects as a power loss [97].

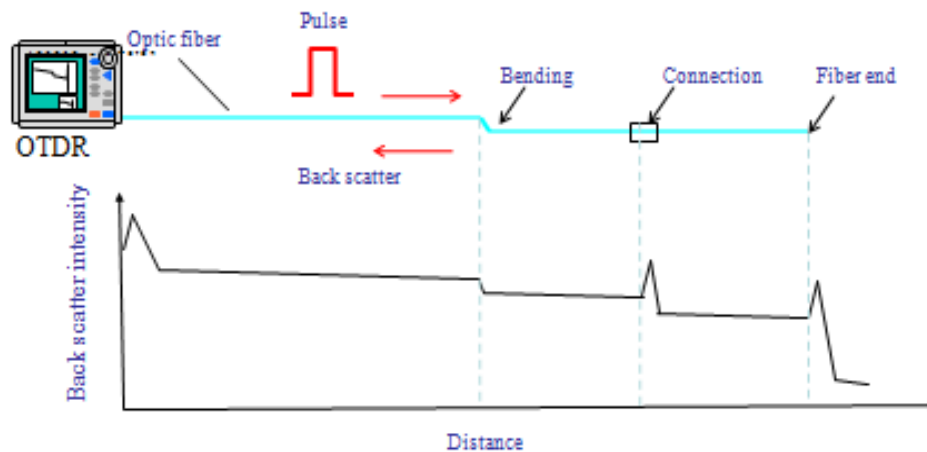


Figure 138

Principle of OTDR based optic fiber

The pulsed laser input signal sent from the OTDR equipment is reflected at each of the perturbations along the length of sensor as a power loss. This power loss is considered to be the outcome of mainly two effects in the optic fiber: bending/curvature or breaking. This intensity change can directly relate to the damage state when appropriately calibrated.

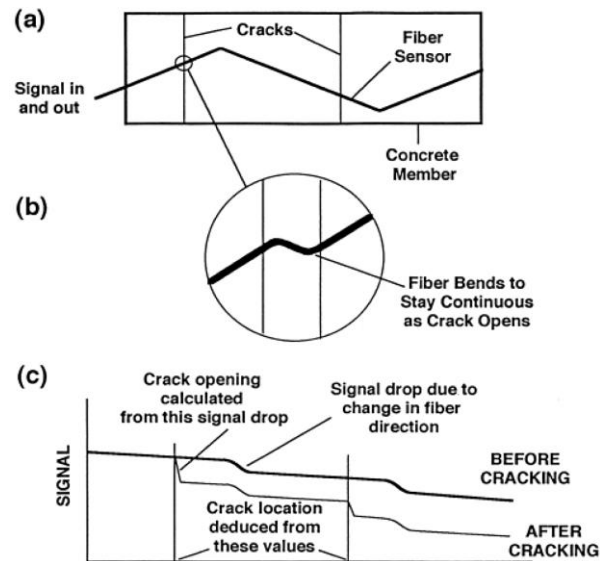


Figure 139
OTDR based optic fiber crack sensor

To overcome limitations of conventional FOS such as local sensing and a lack of differentiation in the extent of damage, the zigzag sensor was introduced [16]. The working principle of this sensor is shown in Figure 139. The sensor was affixed to the bottom of a bridge deck to illustrate its applicability. A backscattered signal versus time data is collected before crack formation to establish a datum for comparison once the cracks are formed along the sensor length. There exist signal losses in the datum line as well, probably due to the absorption of light by the cladding of the fiber. When a crack opens in a structure, a fiber intersecting the crack at an angle other than 90° has to bend to stay continuous [Figure 139 (b)]. This sudden bending of the fiber at the crack results in a sharp drop in the optical signal [Figure 139 (c)]. From the time history data collected by the OTDR system, cracks can be located from the sharp signal drops. This data can be made quantitative by carefully calibrating the data to correspond to the crack opening length [98].

Prior to using the FOS cables, they need to be prepared for use with the optical systems. Although, when coated with polymer cladding, the sensors are pretty tough once they are stripped of this layer before installation; care must be given to protect them from any damage. At times, the fiber might break or a specific end point for the fiber may be desired. To facilitate this, two devices are used, namely:

1. Fiber Cleaver - Fujikura CT-30 and
2. Fusion Splicer - Fujikura FSM-50S splicer

(1) Fujikura CT-30

The CT-30 (Figure 140) provides a clean, straight fiber cut on both ends, making it suitable for splicing later. The 16-position blade yields 48,000 single-fiber cleaves and the built-in scrap collector stores fiber shards until they can be safely discarded.



Figure 140
The fiber cleaver unit - Fujikura CT-30

Procedure for cleaving is as follows:

- Remove at least 2 in. (0.0508 m) of the coating on the fiber from the section to be cleaved using a stripping tool.
- Clean the stripped end with lint free tissue soaked in iso-propyl alcohol.
- Open the cleaver cover and blade assembly.
- Place the fiber across the cleaving area, ensuring sufficient material crosses the cleaving section.
- Adjust the position of the non-stripped portion of fiber at the appropriate marking provided at the blade assembly. Lock the fiber in this position.
- Press down on the cleaver cover until a click is heard.
- Remove fiber from the cleaver apparatus and directly place into fusion splicer.

(2) Fujikura FSM-50S Splicer

The FSM-50S Fusion Splicer uses a high temperature welding process to provide a better optical connection. The unit, shown in Figure 141, has both a splicing section and shrinking tube/protective sleeve heating section, which provides further protection to the newly spliced components. The unit also includes user friendly features such as calibration-free arc adjustments (with auto splice mode), automatic fiber type identification, and reduced operational steps. The device is operated by an easy-to-use touch screen menu.



Figure 141
Fiber splicing unit - Fujikura FSM-50S

Procedure for splicing is as follows:

- Power up the system (press on green icon) until it shows it's ready for fusion splicing.
- Open the middle compartment wherein the cleaved fiber ends have to be properly placed.
- If a protection sleeve is desired to protect the connection, make sure this has already been inserted through one of the cable ends before splicing.
- Place fiber ends into the fiber holder and ensure fibers are properly aligned before clamping them in position by looking at the touch screen.
- Press the "SET" button, located close to the heating device to begin splicing.
- Once the machine begins to splice the two ends, messages as to the progress of the splicing are displayed on the touch screen. Once splicing is completed the Optical power loss will be reported on the monitor and the fiber is ready for use. Typically an optical loss of up to 0.01dB is acceptable. It is possible that at times error messages will be obtained, stating misalignment and presence of dust. In such situations, remove the fiber ends, and prepare them again as explained in the procedure above.
- After splicing, remove the spliced fiber from the clamps. Slide the protection sleeve over the connection and place it directly into the heating section at the rear end of the apparatus.

- Once the fiber has been placed appropriately, close the top cover of the heating tube and press the “SET” button.
- Once heating and cooling operations are carried out, the system will beep to inform that the process has been completed.

APPENDIX B

Field Long-Term Monitoring Guidelines

A routine periodic inspection involves careful planning before and during testing. The following is a comprehensive list of all items required on-site for any such routine inspection:

- (a) For data acquisition
 - i) si425 Interrogator
 - ii) Channel Coupler extension
 - iii) Laptop with Micron Optics software installed
 - iv) Connector cables
 - v) Connectors
 - vi) Connector head cleaner
 - vii) Cable ties

- (b) For power supply
 - i) Portable Generator
 - ii) Extension cord
 - ii) Fuel for generator
 - iii) Lubricant Oil

- (c) For setup and safety
 - i) Hard hats
 - ii) Vests
 - iii) Ladders
 - iv) Table

System Concepts

FBG (Fiber Bragg Gratings) form the integral sensing unit of this FOS system. They are intrinsic spectrometric sensors with local and multiplexing sensing abilities. FBG are generated by engraving a periodic modulation of the refractive index of about 0.393 in. (1 cm) in the core of an optical fiber.

Strain indicated by expansion or contraction of the optical fiber can be caused by loading or temperature changes. The spacing of the grating in a sensor, called the “pitch,” reflects the incident light with a narrow band centered about the “Bragg” wavelength, defined by

$$\lambda_0 = 2n\Lambda \quad (29)$$

where, λ_0 is the Bragg wavelength, n is the average effective index of refraction of the grating, and Λ is the pitch spacing.

FBG also provides a linear response based on the measurement of wavelength shift ($\Delta\lambda$) due to the straining of the gauge. Once temperature effects are accounted for in the wavelength shift, $\Delta\lambda$ provides a means of determining the strain according to the equation:

$$\Delta \lambda / \lambda_0 = (GF)\varepsilon + \beta\Delta T \quad (30)$$

where, $\Delta\lambda = \lambda - \lambda_0$; GF is the FBG gauge factor, typically about 0.75 – 0.82;

ε is the strain; β is the thermal coefficient; and ΔT is the temperature change relative to the temperature at installation.

The change in the length of an optical fiber with Bragg gratings indicate strain induced by either loading, temperature, or both. The fiber optic Bragg grating sensor response is a function of axial strain and temperature change on the grating as clear from equation (30). The GF and β are manufacture provided values.

Appropriate calibration tests have revealed that 1.2 pm/ $\mu\varepsilon$ is the average strain gauge factor. Wavelength shift due to a combination of strain and temperature can be isolated with certain sensors being strategically installed as dummy sensors.

Monitoring Procedure

Before beginning data acquisition, all instruments should be conveniently setup at the proximity of the bridge. The generator should be primed and started supplying power to all instrumentation used. Once both the interrogator and laptop is ready for operation, all sensor cable leads from the stored location have to be brought out to the data acquisition system. Connect the appropriate cables to the interrogator outlet and check their functionality by shifting through the various views available in the si425 front panel graphical interface. A brief introduction to the si425 system along with step-by-step operation instructions is detailed in the following section.

SI425 Optical Sensing Interrogator. The si425 Optical Sensing Interrogator from Micron Optics, Inc., provides rapid, accurate measurements of hundreds of optical sensors in real time. It is a multi-FBG sensor system that can support up to 512 sensors on four fibers, powered by a high output power swept laser source. The current si425- 500 system has four functional channels on the main unit, which has a working wavelength range of 1510-1590 nm. The scan rate is 250 Hz for less than 100 sensors used simultaneously. An additional

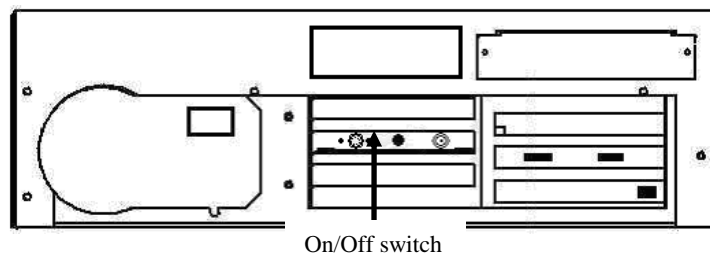
coupler extension module can increase the number of available channels further. This system can be controlled and monitored remotely through a complete set of Ethernet controls.

The si425 optical sensing interrogator system allows for a quick collection of wavelength shift information from fiber optic sensors. Their applications include strain measurements for civil structures such as bridges and roads, force monitoring in prestressed tendons, performance monitoring of web-flange interface in composite decks, and long-term performance monitoring of rehabilitated structures.

System Description. The front control panel of the si425 mainly consists of an LCD display screen that allows real time data viewing, menu keys for navigation through options menus, arrow keys for incrementing integer data inputs, number keys for numeric data entry, and FC/APC connectors for connecting the optical sensors as seen in Figure 142(a). The alternating action power switch of the system is located at the rear of the unit, as shown in Figure 142(b).



(a) Front panel view



(b) Rear panel view

Figure 142
Front and rear panel view of si425

SM040-016 (16-ch. Coupler Extension). This 1U chassis contains four 1 x 4 couplers to accommodate connections of up to four fibers to each si425-500 optical channel. All fibers are scanned simultaneously. It is solely intended to provide more fiber connection

options. When structural strain monitoring requires several fiber optic sensors and more than just four optical fibers, the expansion module sm040-016 facilitates this (Figure 143).



Figure 143
SM040-016 (16-ch. coupler extension)

SI425 Acquisition System Interface. The front panel graphical interface provides four standard screen views either through the built-in LCD or via Ethernet on a remote PC; they are:

Sensor Wavelength View: shows wavelength vs. time for selected sensors. In this view, the user can select both the data acquisition rate of the si425 as well as the time base over which data are displayed to the screen as seen in Figure 144.

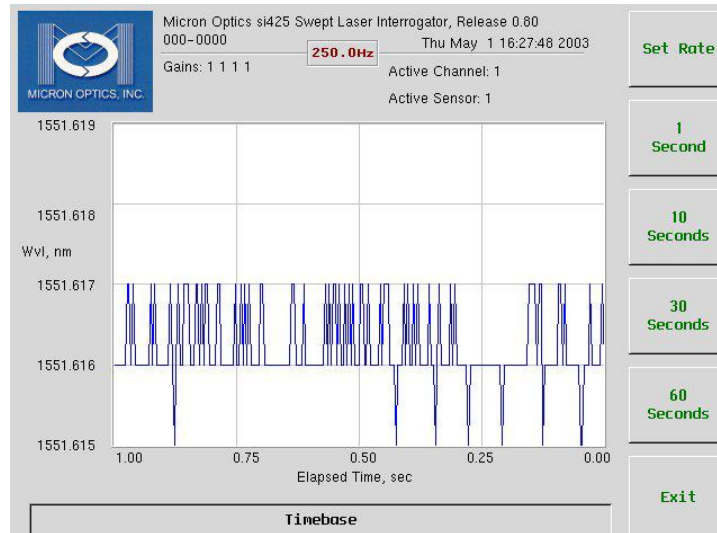


Figure 144
Sensor wavelength view screenshot

Table View: simultaneously displays wavelengths for all sensors on all channels as shown in Figure 145.

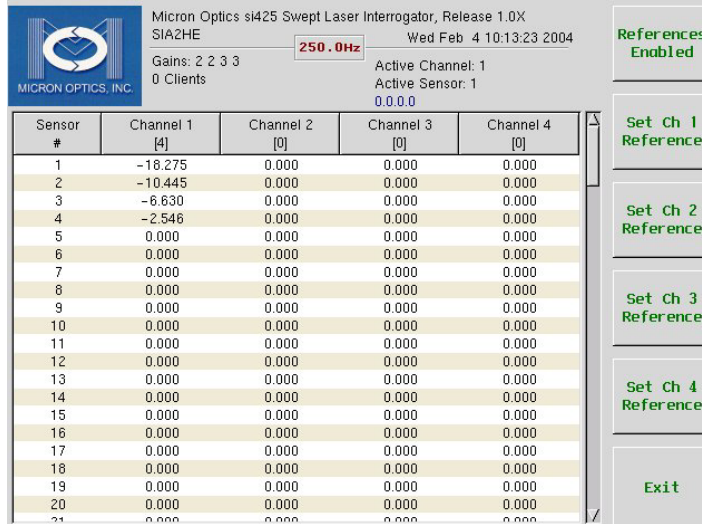


Figure 145
Table view screenshot

Channel Power View: gain level for each channel can be set here ensuring that the sensors are in the proper power band for optimal measurements, as shown in Figure 146.



Figure 146
Channel power view screenshot

FFT View: this view shown in Figure 147, accurately identifies the fundamental frequency of oscillations.

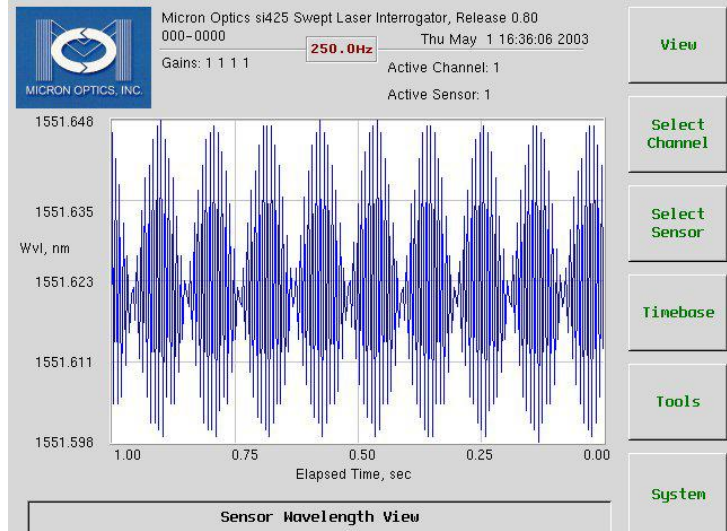


Figure 147
FFT view screenshot

Operation Procedure for the si425 Labview Utility.

Step 1: Press the power switch at the rear of the system that leads to an initialization mode of the si425. Connect the crossover Ethernet cable to the host PC with si425 software installed and power up the remote host PC.

Step 2: Once the system has finished initializing, the user is mostly able to see the sensor wavelength view first. The other alternate views such as the sensor FFT view can be accessed from the menu at the right end of the display monitor by clicking on “View.” The menus on the right hand side of the display screen are the options available at the beginning shown in Figure 148.

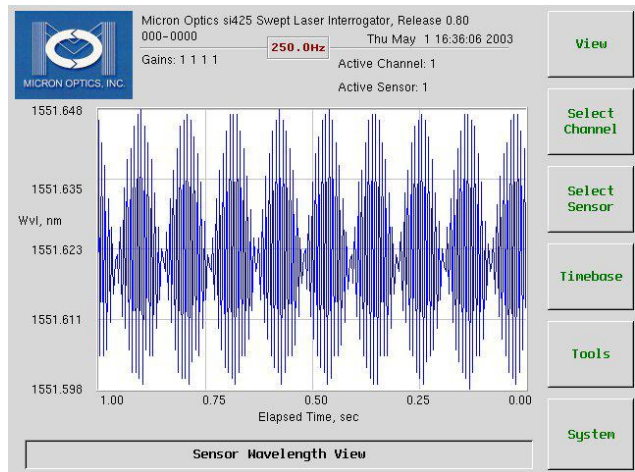


Figure 148
Sensor FFT view with basic menu options

Step 3: The next step to be taken is to establish communication between the si425 and the host PC. To be able to collect and store data while using the interrogator, the si425 system must be connected to a host PC via a provided crossover Ethernet cable. Data transfer to and from the si425 is through a 100Mbit/S Ethernet port on the back of the unit. To setup remote control interface, one should first detect the IP address and network mask of the si425 system. For this, a button labeled “System” placed at the bottom right corner of any view has to be clicked (Figure 148). Clicking on the system button reveals the system menu as seen in Figure 149.

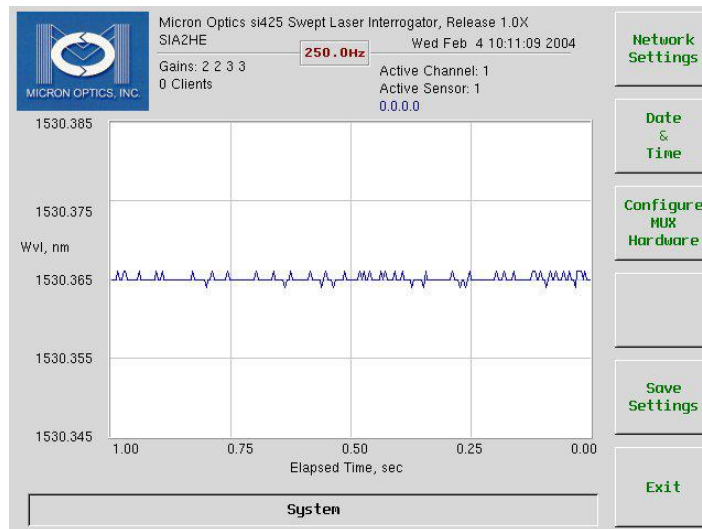


Figure 149
Sensor wavelength view with system menu options

When not connected to a remote client (host PC), the display beside the Micron Optics, Inc., symbol will read “0 Clients.” To ensure data transfer, this message has to change to reflect the recognition of a remote client. First, collect the default IP address and Network Mask ID from the si425 system. This information can be accessed by clicking on the “Network Settings” button, giving rise to the button labeled “IP Addr & Netmask” (Figure 150). The default values of IP address and network mask for the si425 are 10.0.0.129 and 255.255.255.0, respectively. For proper communication, the host PC and the si425 must be set for the same network mask and different, but compatible, IP addresses. A typical correct setting is shown in Table 9.

Table 9
Typical correct network settings

	Host PC	si425
IP Address	10.0.0.121	10.0.0.129
Netmask	255.255.255.0	255.255.255.0

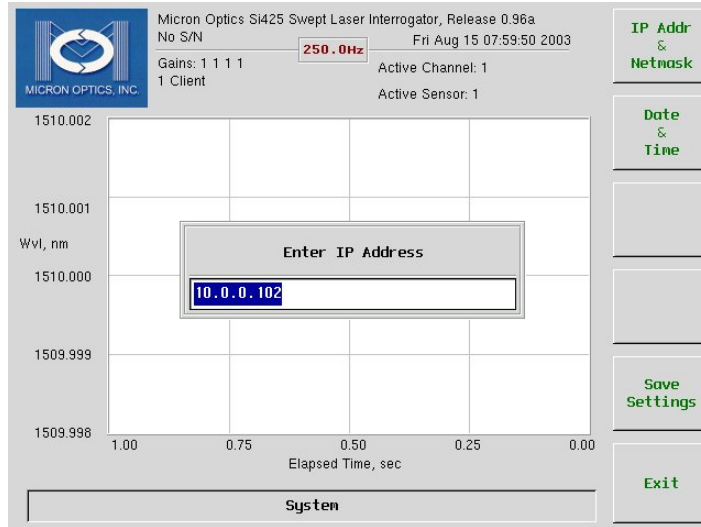


Figure 150
System IP address query screen shot

To begin setting the network mask and IP address on host PC either of the two methods explained below can be adopted.

Method 1

For a personal Windows XP system, i.e., when you are the administrator of the machine being used, go to “Control Panel.” Click on the icon “Network Connections,” highlight the “Local Area Network” selection, right click, and choose “Properties.” The window shown in Figure 151 will appear. Highlight the “TCP/IP” entry and click “Properties.” You will then have access to change the IP address and subnet mask. Click “OK” to save settings.

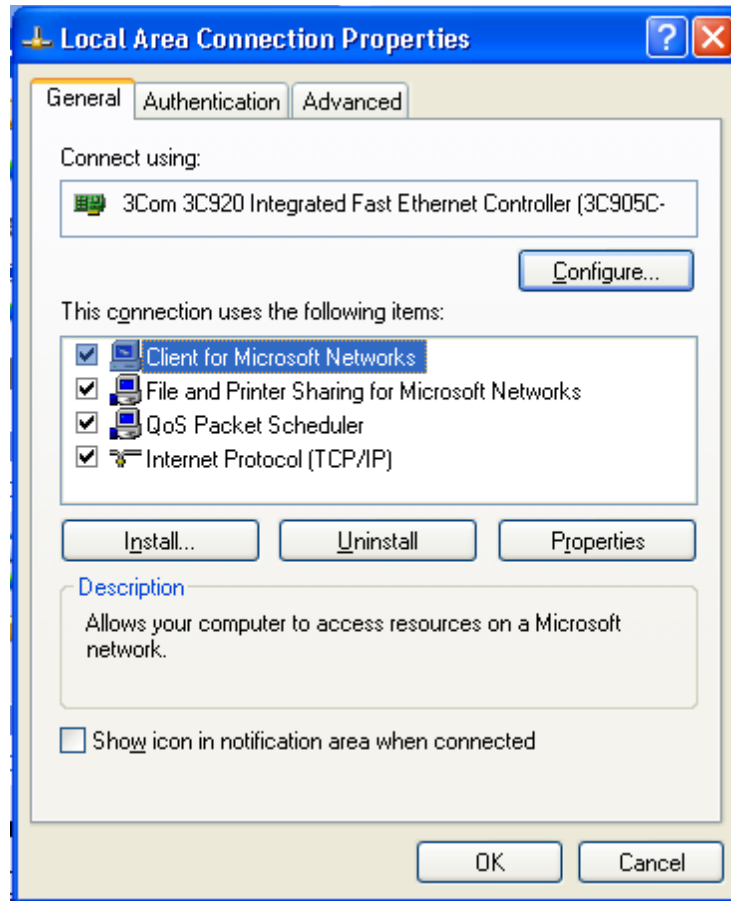


Figure 151
Local area connection property window

Method 2

Get to the command prompt in your system and type in IPCONFIGURE; one can update the IP address as required from there. Once the link is established, the system will recognize the remote client and notice the change in message from “0 Client “to “1 Client” in Figure 152.

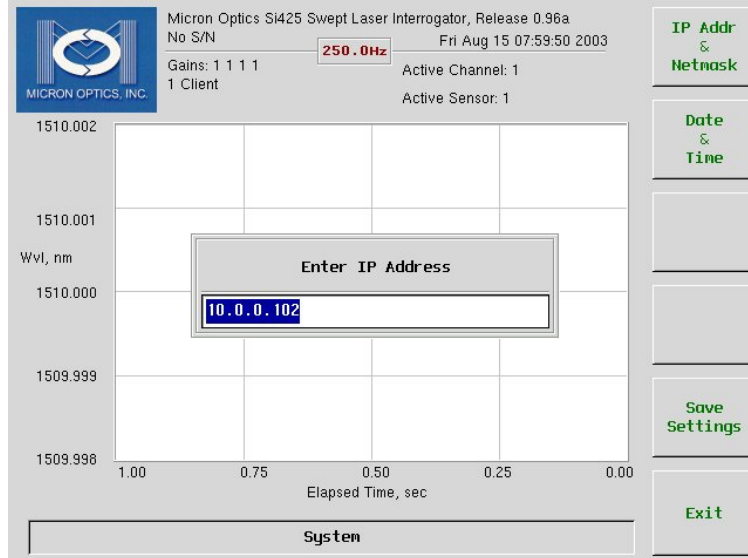


Figure 152
Screen shot when remote client identified

Step 4: The last and final step is to save and retrieve data that are collected from the sensors during testing. Open the si425 utility software in the host PC and the user is typically prompted to enter the IP address and network mask of the interrogator as shown in Figure 153.

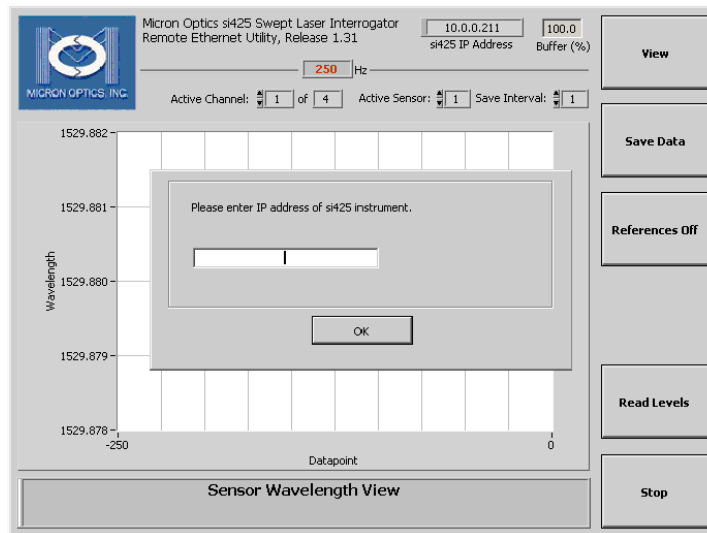


Figure 153
Typical host PC software interface

Enter the appropriate IDs as mentioned in Table 9 and the host PC is ready to collect information from the si425 system. The menu items on the right hand corner of the graphical user interface (GUI) though similar to the system display menu, have other options such as “Read Levels” and “Save Data.”

Clicking on the “Read Levels” button takes the user to a Channel Power Level View shown in Figure 154, which collects both wavelength and level information. The remote Channel Power Level View is intended for setup and diagnostic use, not for full-speed data transfer.

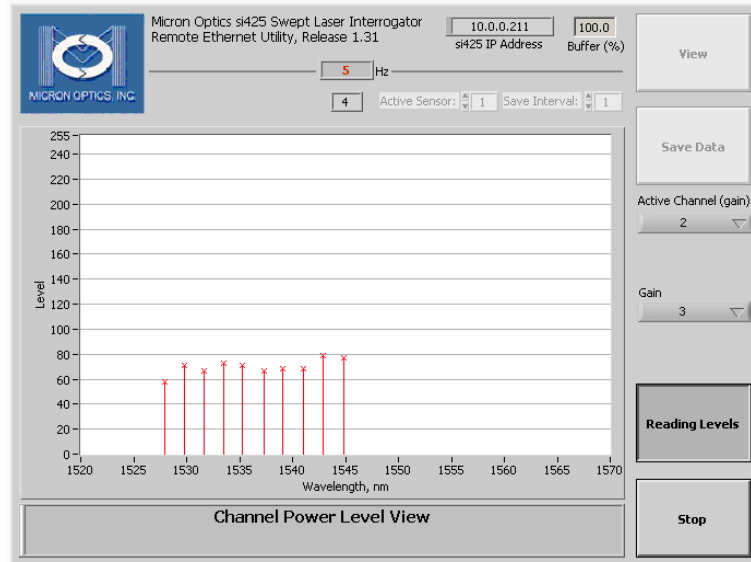


Figure 154
Screen shot of channel power level view in LABVIEW utility

To initialize data saving, click on the button “Save Data.” The program then prompts the user for a file path for the saved data (Figure 155). A customized file name of “####@.txt” can be assigned and accepted by clicking “OK.” Once a file path is selected, data saving begins until the “Saving...” button is clicked again, which turns off the data save function. The stored data typically appear as shown in Table 10.

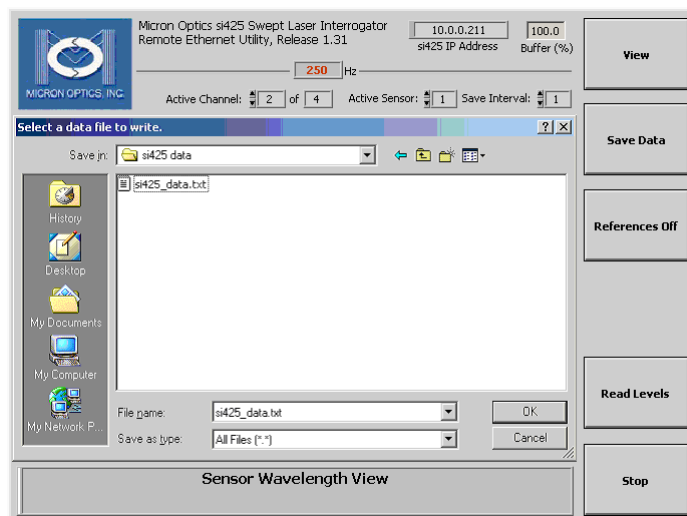


Figure 155
Save data mode screen shot

Table 10
Sample data format

TIMEBASE	CH1_SN	CH2_SN	CH3_SN	CH4_SN	DATA
1052737738.68036	0	0	3	0	1530.973 1538.781 1546.617
1052737738.68446	0	0	3	0	1530.972 1538.781 1546.612
1052737738.68856	0	0	3	0	1530.972 1538.781 1546.615
1052737738.69265	0	0	3	0	1530.972 1538.782 1546.613
1052737738.69675	0	0	3	0	1530.972 1538.781 1546.615
1052737738.70085	0	0	3	0	1530.972 1538.781 1546.614
1052737738.70494	0	0	3	0	1530.973 1538.782 1546.613
1052737738.70905	0	0	3	0	1530.972 1538.781 1546.615
1052737738.71314	0	0	3	0	1530.973 1538.783 1546.613
1052737738.71723	0	0	3	0	1530.971 1538.782 1546.619
1052737738.72133	0	0	3	0	1530.972 1538.783 1546.619

Step 5: As seen in Table 10, only wavelength values are recorded by the si425. Post-processing of this data is done using MATLAB to reveal strain and temperature values. The system concept involved is that strain indicated by expansion or contraction of the optical fiber can be caused by loading or temperature changes. The spacing of the grating in a sensor, called the “pitch” reflects the incident light with a narrow band centered about the “Bragg” wavelength, defined by:

$$\lambda_0 = 2n\Lambda \quad (31)$$

where, λ_0 is the Bragg wavelength, n is the average effective index of refraction of the grating, and Λ is the pitch spacing.

FBG also provides a linear response based on the measurement of wavelength shift ($\Delta\lambda$) due to the straining of the gauge. Once temperature effects are accounted for in the wavelength shift, $\Delta\lambda$ provides a means of determining the strain according to the equation:

$$\Delta\lambda/\lambda_0 = (GF)\varepsilon + \beta\Delta T \quad (32)$$

where, $\Delta\lambda = \lambda - \lambda_0$; GF is the FBG gauge factor, typically about 0.75 – 0.82; ε is the strain; β is the thermal coefficient; and ΔT is the temperature change relative to the temperature at installation.

This public document is published at a total cost of \$250. 42 copies of this public document were published in this first printing at a cost of \$250. The total cost of all printings of this document including reprints is \$250. This document was published by Louisiana Transportation Research Center to report and publish research findings as required in R.S. 48:105. This material was duplicated in accordance with standards for printing by state agencies established pursuant to R.S. 43:31. Printing of this material was purchased in accordance with the provisions of Title 43 of the Louisiana Revised Statutes.